Master's thesis

2019

Runar Braut Kyllingstad

NTNU
Norwegian University of
Science and Technology
Faculty of Natural Sciences
Department of Materials Science and Engineering

Master's thesis

Runar Braut Kyllingstad

Strength and Ductility in two Ultra High Strength Al-Alloys AA2196 and AA7090

June 2019

NTNU
Norwegian University of
Science and Technology

NTNU
Norwegian University of
Science and Technology

NTNU

Norwegian University of
Science and Technology

Strength and Ductility in two Ultra High Strength Al-Alloys AA2196 and AA7090

Runar Braut Kyllingstad

Materials Science and Engineering
Submission date: June 2019
Supervisor: Ola Jensrud
Co-supervisor: Rune Østhus
Hans Jørgen Roven

Norwegian University of Science and Technology
Department of Materials Science and Engineering

Abstract

An initial evaluation of the mechanical properties, anisotropy and grain structure of AA2196 has been conducted for a proposed heat treatment process in order to determine the applicability of the process and to determine whether the third-generation Al-Li alloy AA2196 is a suitable material for aerospace applications, particularly for propulsion systems.

Tensile testing and Charpy testing have been conducted for cold rolled samples to determine the mechanical properties following cold work ranging from 0-56.3%. Additionally, these results have been compared with another aerospace alloy, AA7090, to establish a baseline for comparison. Initial tensile testing of AA2196-T8511 as delivered showed an average of yield strength of 656MPa, an average tensile strength of 663 MPa and an average elongation of approximately 5.68%. After heat treatment, the highest strength obtained for AA2196 was at approximately 10%CW, with an average yield strength of 435 MPa, an average tensile strength of 525 MPa and an average elongation of 7.84%. AA7090 exhibited higher strength and a lower elongation than AA2196. The highest strength for AA7090 was found after 9.2% cold work with averaged values for yield strength, tensile strength and %elongation at 691 MPa, 707 MPa and 3.37%, respectively.

Charpy testing revealed that the fracture energies for AA2196 were in the range of 7.5-23.59J, while the fracture energy for AA7090 ranged from 1.34-2.86J. Generally, the fracture energies decreased as a result of cold work. A minor hardness increase and a finer grain structure were found when comparing the core of a Charpy sample with hardness values and grain structure close to the surface of the sample, thus implying inhomogeneous samples. Generally, the fractures of AA2196 were fibrous, while the fracture surfaces of AA7090 were more granular. It is likely that a reason for the higher fracture energy of AA2196 is due to some energy being absorbed in order to propagate the fracture, thus giving higher fracture energy.

The anisotropy both prior to and following heat treatment has been investigated. In both cases, there were observed an extrusion texture. Cold pressing generally resulted in a decrease in texture, but an extensive cold pressing of 55.5% in the extrusion direction resulted in a compression texture. Both 40.1% and 58.7% cold pressing in the transverse direction resulted in a recrystallisation texture that is thought to be due to the presence of sub-grains.

The grain size was found using EBSD, Electron Backscatter Diffraction. Increased amounts of cold work resulted in a decrease in grain size. The initial grain size was found to be 10.8 μm in the extrusion direction and 3.1 μm in the transverse direction. The finest grains obtained after cold working were found at 55.5%CW in the extrusion direction and 58.7%CW in the transverse direction and were 7.8 μm and 7.6 μm respectively. Investigation of OM, optical microscope, images indicated no recrystallisation, and hence the reduction in grain size was most likely due to the nucleation of sub-grains.

The heating and holding time for various stages were investigated using a data logger. Heat treatment steps included were annealing, solid solution heat treatment and aging. It was found that the alloy was not solid solution heat treated for 60 minutes at 530°C, but rather experienced a holding time of only 5 minutes above 500°C, in which there is thought to

exist a single-phase area. Consequently, there were less Cu and Li in solid solution than previously anticipated, which may have been detrimental to the precipitation hardening. Additionally, the temperature discrepancy between the furnace display temperature of N11/R and the air temperature were logged and found to be almost 30°C during aging at 160°C. Aging curves were created for AA2196 at 150°C, 160°C and 180°C and for AA7090 at 120°C, but due to the temperature deviation between the display and actual temperature experienced, the curves should be used as an indication only.

Lastly, several improvements for the heat treatment process has been proposed, including the usage of a lower volume of air to area furnace, causing a more uniform temperature gradient within the furnace, pre-heating prior to annealing and an increased solutionising holding time. Furthermore, it has been suggested to introduce a deformation step to increase the strength and toughness of AA2196 due to the formation of T_1 particles.

Sammendrag

I denne masteroppgaven blir de mekaniske egenskapene, kornstrukturen og anisotropien i tredjegenerasjons Al-Li legeringen AA2196 undersøkt etter en foreslått varmebehandlingsprosess. Hensikten med rapporten er å undersøke om legeringen er egnet som materiale i fremdriftssystemer for romfartsapplikasjoner.

Oppgaven innbefatter både strekkprøving og Charpy testing for prøver kaldbearbeidet 0-56.3%. Prøvene har blitt sammenlignet med AA7090, en annen romfartslegering, for å ha sammenligningsgrunnlag. Strekkprøving av AA2196-T8511, tilstanden som levert, ga gjennomsnittlig flytespenning på 656 MPa, strekkfasthet på 663 MPa og forlengelse på 5,68%. Størst styrke etter varmebehandling av AA2196 ble funnet etter cirka 10% kaldvalsing. De gjennomsnittlige verdiene var 435 MPa i flytespenning, 525 MPa i strekkfasthet og 7,84% forlengelse. AA7090 utviste høyere styrke, men lavere forlengelse enn AA2196. Høyest styrke ble funnet for AA7090 ved 9.2 %CW, og de respektive gjennomsnittsverdiene var på 691 MPa i flytespenning, 707 MPa i strekkfasthet and en forlengelse på 3,37%.

Under Charpy testing viste AA2196 seg å ha en bruddseighet på 7,50 til 23,59 J, mens AA7090 hadde verdier i området 1,34 til 2,86 J. Økt kaldbearbeiding av AA2196 resulterte i en lavere absorbert bruddenergi. Overflaten av en Charpy test ble hardhetstestet, fikk mikrostrukturen undersøkt og ble sammenlignet med kjernen av prøven. Kjernen viste seg å ha en marginalt høyere hardhet og en finere kornstruktur enn overflaten, noe som tyder på inhomogene prøver. Bruddflatene til AA2196 var mer fiberaktive, mens bruddflatene til AA7090 var mer granulære. Grunnet høyere duktilitet i AA2196, vil noe av energien i Charpy testingen gå med til å forplante bruddet, og dermed føre til en høyere målt bruddenergi.

AA2196, både før og etter varmebehandling, ble undersøkt i EBSD for å se etter tekstur. I begge tilfeller ble det observert en ekstruderingstekstur. Økt kaldbearbeiding resulterte i en mindre definert tekstur, og dermed også mindre anisotropi. Ved 55,5% kaldpressing i ekstruderingsretning ble det observert enakset kompresjonstekstur. Kaldpressing av materialet 40,1% og 58,7% i den tverrgående retningen resulterte i tendenser til rekrystalliseringstekstur, noe som er antatt å skyldes subkorn dannelse.

Kornstørrelsen ble funnet ved hjelp av EBSD og viste seg å synke med økende grad av kaldbearbeiding. Den initielle kornstørrelsen ble funnet til å være 10,8 µm i ekstruderingsretningen og 3,1 µm i tverrgående retning. Etter 55,5 % kaldpressing i ekstruderingsretningen og 58,7% i tverrgående retningen ble kornstørrelsen respektivt 7,8 µm og 7,6 µm. Lysoptiske bilder ble studert og indikerte ingen rekrystallisasjon, noe som tyder på at reduksjonen i målt kornstørrelse skyldes kimdanning av subkorn.

Oppvarmingstiden og holdetiden ved mykgløding, innherding og utherding ble undersøkt ved hjelp av en data logger. Det ble oppdaget at holdetiden for innherding ikke var 60 minutter på 530°C, men at materialet bare opplevde 5 minutter over 500°C, hvor det er antatt det eksisterer en grense for et enfaseområde. Dermed var det betydelig mindre Cu og Li i fast løsning, noe som kan ha ført til at mindre presipitater ble utfellet under utherdingen. Det ble også oppdaget et avvik opp mot 30°C mellom temperaturen på

displayet i en varmluftsovn og på den faktiske temperaturen inne i ovnen. Utherdingskurver er blitt laget for AA2196 ved 150°C, 160°C og 180°C og for AA7090 ved 120°C. Grunnet temperaturavviket mellom display og faktisk ovnstemperatur, anbefales det at utherdingskurvene bare brukes som en indikasjon på trender.

Til slutt ble ulike forbedringsforslag for varmebehandlingsprosessen lagt frem. Disse var blant annet å forvarme materialet før mykgløding, å ha lengre holdetid ved innherding for å få mer legeringselementer i fast løsning og å bruke en ovn med lavere volum luft relativt til areal, og på den måten få en ovn med lavere temperaturgradient i luften. Et deformasjonssteg ble også foreslått for å få dannet flere T_1-presipitater og på den måten øke styrken og seigheten til materialet.

Preface

This master's thesis, and the corresponding work, is the basis for the subject "TMT4905 Materials Technology, Master's Thesis" at NTNU Gløshaugen. I hereby declare that I have worked individually and that the following results are based on actual experiments conducted by me, Runar Braut Kyllingstad, during the spring of 2019, unless otherwise noted.

This master's thesis is based on previous work done in the specialization project TMT4500 "Materialteknologi, fordypningsprosjekt" at NTNU. Some parts of said thesis have been reused, specifically, parts regarding the theoretical background and experimental method used. Additionally, several confidential documents from NAMMO Raufoss have been used for heat treating AA7090.

I have chosen APA as the reference system, as I think it gives more credit to the author of each article or book, and because I think it is a beneficial system to recognise which authors are recurring throughout this paper.

I would like to thank my supervisor Ola Jensrud for his guidance during this master's thesis and Rune Østhus for his help with data logging the faulty furnace. Additionally, I would like to thank Yingda Yu for his help in operating and interpreting the results obtained from the EBSD analysis. My thanks to Pål Christian Skaret who helped me with both Charpy testing and tensile testing. Furthermore, I would like to thank the workshop at Sintef Manufacturing for cutting the extruded billet.

Runar Braut Kyllingstad

Trondheim, 19.06.19

Table of contents

Abbreviations

EBSD: Electron Backscatter Diffraction

ESA: European Space Agency

GP zones: Guinier-Preston zones

LOM: Light Optical Microscope

NAMMO: Nordic Ammunition Company, or "Norsk Ammunisjon AS" in Norwegian.

NTNU: Norwegian University of Science and Technology

OM: Optical Microscope

SEM: Scanning Electron Microscope

TEM: Transmission Electron Microscope

wt%: weight percent

%CW: Percent cold worked

%EL: Percent elongation

1. Introduction

The aerospace industry is a highly technological industry that requires materials with excellent attributes in highly stressful environments. Aluminium-lithium alloys have shown excellent mechanical properties in such areas, and have therefore obtained considerable interest (Kim et al., 2016) (James, 1990) (Callister Jr & Rethwisch, 2015f). Aluminium generally has a high specific strength that, if added lithium, results in an even stronger and lighter alloy, and is therefore highly suitable for aerospace applications where weight plays a significant role (James, 1990) (Nayan et al., 2014). One example of the benefit of replacing conventional materials with Al-Li alloys is that is it estimated to provide weight savings of approximately 25% by replacing 2024-T351 with 2199-T8E79 (Giummarra, Thomas, & Rioja, 2007)

Compared to other excellent aluminium alloys such as AA7075, Al-Li alloys have seen a large increase in specific modulus over time, thereby increasing weight savings (Rioja & Liu, 2012). Al-Li alloys have been researched for over 50 years by the aerospace industry, which has resulted in the so called "third-generation Al-Li alloys" (Rioja, 1998) (Rioja & Liu, 2012). Third-generation Al-Li alloys are aluminium alloys with a large addition of Cu while containing a lower content of Li, compared to earlier generations (Abd El-Aty et al., 2018) (Warner, 2006). One such alloy is AA2195, which is an excellent candidate for fuel tanks in rockets, having already been used in the Space Shuttle Program by NASA (Chen & Bhat, 2002).

Constellium, a manufacturer of third-generation AL-Li alloys, produces such alloys under the marketing name "Airware". Airware comprises a range of different Al-Cu-Li alloys, including AA2196. Due to the high strength of AA2196, the alloy has been utilized as the material for the fuselage frame and stringers, the upper wing stringers and floor beams and seat rails in Airbus A380, thereby replacing previously used alloys such as AA7075 and AA7150 (Wanhill & Bray, 2014). AA2196 also exhibits excellent corrosion resistance and has a high damage tolerance (Uféras, 2017b), making it a prime candidate material for aerospace applications when reliability is an important factor. As a consequence due to Li-additions, AA2196 has a low density and high modulus of elasticity, even when compared with other third-generation Al-Li alloys (Uféras, 2017a, 2017b).

For previous generations of AL-Li alloys, a major drawback when using Al-Li alloys were the high anisotropy, thus limiting their usability (Abd El-Aty et al., 2018). For extruded products, such as AA2196, the extrusion direction is generally the strongest direction, while off-axis directions suffer poorer properties due to an extrusion texture (Rioja, 1998). According to Rioja & Liu (2012), third-generation Al-Li alloys have a less distinct texture than previous generations, thus opening up the possibility for a wider range of applications.

Prior to the emergence of third-generation Al-Li alloys, 7xxx were some of the most prominent alloys systems used for aerospace applications (Niedzinski, 2019) and are a benchmark candidate when comparing properties (Daniélou, Ronxin, Nardin, & Ehrström, 2016) (Niedzinski, 2019). When designing a fuel tank for aerospace applications, cryogenic temperatures are to be expected (Nayan et al., 2014). Several 7xxx alloys suffer

embrittlement when exposed to cryogenic temperatures, while several third-generation Al-Li alloys exhibit a higher fracture toughness at cryogenic temperatures, making third-generation Al-Li alloys more suitable as the structural material in fuel tanks in which such temperatures are likely (Niedzinski, 2019).

The Al-Cu-Li system experiences precipitation hardening, resulting in high strength aluminium alloys, such as AA2195 and AA2196 (Warner, 2006) (Uféras, 2017a, 2017b). Contrary to second generation Al-Li alloys, the third-generation seems to be mainly strengthened by T_1 and θ' particles, instead of δ' (Warner, 2006) (Chen & Bhat, 2002) (Elgallad, Lai, & Chen, 2014) (Hekmat-Ardakan, Elgallad, Ajersch, & Chen, 2012). Additionally, as in other AL-Cu alloys (Solberg, 2014), some third-generation AL-Li alloys experiences natural aging, resulting in a significant hardness increase (Kyllingstad, 2018), which may complicate the ease of storage.

An added benefit for several Al-Li alloys is that they may be recycled indefinitely, and several alloys may be welded, using techniques such as Friction Stir Welding for AA2195 and AA2196 and Laser Beam Welding for AA2196 (Uféras, 2017a, 2017b), increasing the ease of manufacturing, thus allowing for a wide array of potential applications. A consequence of the low density is that Al-Li has a higher specific strength than conventional 7xxx and 2xxx alloys (Giummarra et al., 2007).

1.1 Scope of Work

This master thesis aims to give a preliminary insight into the mechanical properties of AA2196 following cold work and heat treatment to investigate the validity of the heat treatment and to give an initial assessment whether AA2196 might be a suitable alloy for aerospace applications, particularly propulsion systems. The principal focus of this master's thesis has been directed towards determining the strength and ductility for cold worked samples and to give an initial overview regarding one of the main challenges when using Al-Li alloys, the anisotropy. Furthermore, the response for the material regarding the heat treatment have been investigated by finding an initial estimate of the grain size after various stages of cold work for both the extrusion direction and the transverse direction. Additionally, data logging of the heating time to a designated temperature and the holding time for various stages during heat treatment has been conducted.

A heat treatment consisting of an annealing step, solid solution heat treatment and precipitation hardening have been used for AA2196 and are based on previous work conducted. Previous work proved that following solid solution treatment and precipitation hardening, there was registered a hardness increase compared to the annealed state (Kyllingstad, 2018). The Al-Li hardening mechanisms will be discussed based on an initial literature review. Subsequently, the experimental procedure will be discussed briefly, followed by the results obtained and relationships discovered. The strength and ductility have been investigated using tensile testing and Charpy testing. Aging curves have been constructed to determine the hardening response following heat treatment. Lastly, the findings are discussed and improvements are suggested.

1.2 Limitations

The literature study suggests that an argon atmosphere might be necessary to prevent a reaction between lithium in the alloy and oxygen to create lithium oxide or lithium hydroxide (James, 1990). Practical limitations meant that this could not be achieved. Rather, the aluminium alloy was covered in aluminium foil to retard the process.

All hardness values for solid solution hardening were measured approximately 24 hours after quenching unless otherwise stated. This was due to natural aging, which seemed to slow down after 24 hours. It is assumed that no natural aging occurred after artificially aging the material, hence the measurement of hardness after precipitation hardening was taken at various times after quenching.

Due to a lack of suitable machining tools and a safe method to perform cold working in the transverse direction, no Charpy samples nor tensile testing rods were constructed of samples pressed in the transverse direction. Hence, all impact test and tensile test samples were cold rolled in the extrusion direction.

It has been assumed that the volume is constant until necking during tensile testing. Hence, true stress and strain have been found as a function of the engineering stress and strain.

For this master's thesis, it has been assumed that the extruded bolt of AA2196 and the bolt and extruded profile of AA7090 were homogeneous and that no concentration gradient existed within the material.

2. Background

2.1 Aluminium, Al-Cu-Li alloys and AA2196

Aluminium exhibits a high strength to weight ratio, referred to as specific strength, that may in certain aluminium alloys be greater than those achieved in steel (Callister Jr & Rethwisch, 2015f). The superior specific strength of aluminium over iron is due to the low density of aluminium, 2.70 g/cm^3, compared to the higher density of iron, 7.87 g/cm^3, making aluminium a suitable choice for lightweight applications such as aeroplanes and cars (Solberg, 2014).

Aluminium alloys range a vast scope of abilities, with various alloying elements improving the capabilities of the desired property (Callister Jr & Rethwisch, 2015f). Generally, aluminium is divided into subcategories differentiating between wrought and cast alloys (Solberg, 2014). Wrought alloys are aluminium alloys that have high ductility and are thus shaped into the desired geometry (Solberg, 2014). The hardening mechanisms in most aluminium alloys are usually some, or all, of the following; cold working, solid solution hardening and precipitation hardening (Solberg, 2014). A numbering system based on the primary alloying element is used for wrought alloys, ranging from pure aluminium 1xxx alloys to 8xxx alloys, which is used for "other" primary alloying elements not used in previous groups (James, 1990).

AA2196 is classified within the 2xxx – series, a group of aluminium alloys with the primary alloying element being copper (Callister Jr & Rethwisch, 2015f). Copper addition increases the strength of the material while decreasing the elongation and enables the possibility of solid solution strengthening and precipitation hardening (Solberg, 2014). The strength of a material may be expressed in engineering stress, seen from Equation 1, with F being the force acting on the material and A the area affected by the force (Callister Jr & Rethwisch, 2015c).

$$\sigma_e = \frac{F}{A} \tag{1}$$

Equation 1 - Engineering stress.

The strain is described using engineering strain, expressed by Equation 2, with l_i the final length and l_0 the initial length (Callister Jr & Rethwisch, 2015c).

$$\varepsilon_e = \frac{l_i - l_0}{l_0} \tag{2}$$

Equation 2 - Engineering strain.

The relationship between the yield stress and elastic strain may be expressed using Hooke's law, Equation 3, where E is the modulus of elasticity (Callister Jr & Rethwisch, 2015c).

$$\sigma = \varepsilon * E \tag{3}$$

Equation 3 - Hooke's law.

The percentage of elongation, %elongation or %EL, may be expressed using the engineering strain, as seen from Equation 4, and are used to describe the plastic strain achieved (Callister Jr & Rethwisch, 2015c).

$$\%EL = \varepsilon_e * 100 \tag{4}$$

Equation 4 - Percent elongation.

In addition to % elongation, the % reduction in area is a way to express the ductility in a material (Callister Jr & Rethwisch, 2015c). Percent reduction in area, %RA may be seen from Equation 5, where A_0 is the initial area and A_f the resulting area (Callister Jr & Rethwisch, 2015c).

$$\%RA = \frac{A_0 - A_f}{A_0} \tag{5}$$

Equation 5 - Percent reduction in area.

Additions of Li increases the elastic modulus of an aluminium alloy while simultaneously decreasing the density, thus enabling the possibility of precipitation of hardening particles (James, 1990) (Hugaas, 1985) (Rioja & Liu, 2012). In the case of AA2196, the resulting modulus of elasticity is 76.5 GPa while the density is 2.63 g/cm^3 (Uféras, 2017b). Pure aluminium on the other hand has a modulus of elasticity of 69GPa and a density of 2.9 g/cm^3 (Callister Jr & Rethwisch, 2015c) (Callister Jr & Rethwisch, 2015f), while AA7090, a competitor to AA2196, has a specific modulus of 72 GPa and a density of 2.83 g/cm^3 according to Materials Datasheet for 7090 by NAMMO Raufoss. Al-Li alloys have been used as structural materials in planes since the 70s (James, 1990), while the combination of Al-Cu-Li, third-generation Al-Li alloys, have been studied for a significantly shorter timeframe (Warner, 2006) (Starke et al., 1995).

For several aerospace applications, such as the fuel tank, a high strength material is needed (Niedzinski, 2019). While AA2196-T8511 has a yield strength of 490 MPa and a tensile strength of 524 MPa for extrusions of thickness between 3.2 and 6.3 mm (Uféras, 2017b), AA7090-T6 has a yield strength of 700 MPa and a tensile strength of 710 MPa for extrusions of thickness between 3 and 10 mm according to NAMMO Raufoss' Materials Datasheet for 7090. The strength values given above are minimum values guaranteed by Constellium for AA2196, and the actual strength may be significantly higher, as seen in the material characteristics given in Appendix A.

The specific strength is an important parameter for aerospace applications, as it determines the amount of load per weight that a material is able to withstand (Rioja & Liu, 2012). The specific strength is defined as the tensile strength, σ_y, divided by the density, ρ, seen in Equation 6 (Callister Jr & Rethwisch, 2015f). For AA2196 the specific strength is 199.2, while for AA7090 it is 247.3 when using the aforementioned values for strength and density.

$$Specific\ Strength = \frac{\sigma_T}{\rho} \tag{6}$$

Equation 6 - The specific strength of a material.

Compared to earlier generations, third-generation Al-Li alloys generally have a lower amount of Li and a higher amount of Cu (Rioja & Liu, 2012). AA2196 is regarded as a third-generation Al-Li alloys (Rioja & Liu, 2012) (Warner, 2006). According to Rioja (2012), earlier Al-Li alloy generations suffered from a large anisotropy, creating problems such as microcracks. Third-generation Al-Li alloys also suffer from similar texture problems due to fabrication processes utilized, though, according to Hekmat-Ardakan (2012), the texture problems are lessened.

Al-Cu-Li alloys, such as AA2196, generally exhibit high strength and damage tolerance (Warner, 2006) (Uféras, 2017b). Consequently, there is considerable interest in Al-Cu-Li alloys for aerospace applications, with varying alloys tailored for specific components. An example is fuel tanks of AA2195 in the space shuttles made by NASA (Rioja & Liu, 2012) (James, 1990) (Starke et al., 1995) (Kim et al., 2016). According to Nayan et al. (2014), AA2195 displays excellent properties at cryogenic temperatures, which is necessary if a fuel tank is to contain liquid hydrogen. The significant improvement in alloy properties with respect to time may be observed in Figure 1 (Rioja & Liu, 2012). Due to the high strength of AA2196, the alloy has been used as upper wing stringers in aircraft (Abd El-Aty et al., 2018).

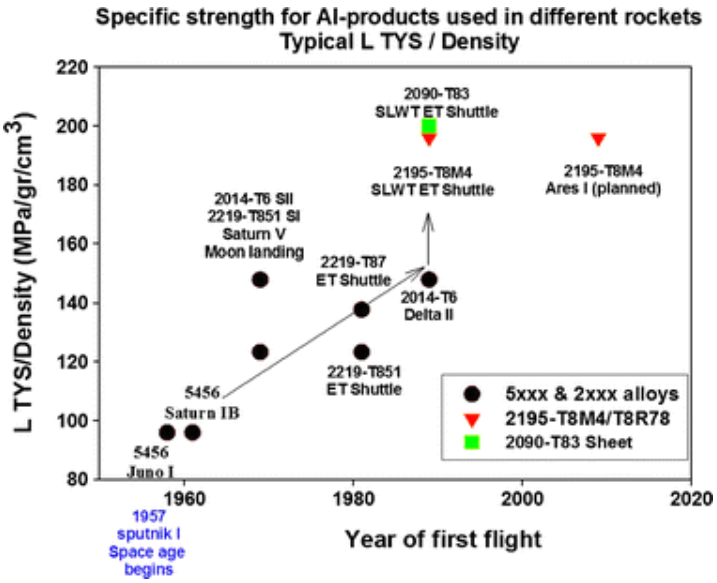

Figure 1 - Plot of the development of aluminium alloys used in rocket fuel tanks (Rioja & Liu, 2012).

Magnesium, silver and zirconium have been added to AA2196 to give higher strength, influence the rate of precipitation and provides thermal stability by forming Al_3Zr-particles, which causes Zener pinning, respectively (Warner, 2006) (Elgallad et al., 2014) (Tsivoulas, Robson, Sigli, & Prangnell, 2012) (Solberg, 2014) (Rioja & Liu, 2012) (Hekmat-Ardakan et al., 2012) (Tsivoulas & Prangnell, 2014). Some Ti and Mn are added to increase the recrystallization temperature and thereby the thermal stability(Solberg, 2014). It is thought that Mn form $Al_{20}Cu_2Mn_3$ dispersoids that cause Zener pinning (Rioja & Liu, 2012) (Tsivoulas & Prangnell, 2014). Fe impurities are minimised as these form Al_7Cu_2Fe particles that reduce the fracture toughness and fatigue life (Rioja & Liu, 2012) (Jiang, Gao, & Zheng, 2010). Si

is also thought to have a harm fatigue life, corrosion and fracture toughness, and thusly Si additions are minimised (Abd El-Aty et al., 2018).

2.2 Heat Treatment

As the alloy was heat treated prior to delivery, annealing was required in order to prepare the material for any further heat treatment. Annealing is conducted by raising the material to elevated temperatures for a certain amount of time, until the material is finally slowly cooled back to room temperature (Callister Jr & Rethwisch, 2015g) (Solberg, 2014). This kind of heat process is generally used to relieve stresses, change the microstructure, for example by dissolving precipitates, or to make the material softer and thus more malleable (Callister Jr & Rethwisch, 2015g) (Solberg, 2014). By increasing the temperature of the reaction, the speed of the annealing process may be increased, as the process is diffusion controlled (Callister Jr & Rethwisch, 2015g). During annealing, recovery, recrystallisation and grain growth may occur (Callister Jr & Rethwisch, 2015g), but due to the additions of Zr, Ti and Mn, the degree of recrystallisation is lowered in AA2196(Rioja & Liu, 2012) (Solberg, 2014).

To achieve a solid solution of alloying elements, the aluminium alloy is heated to higher temperatures, typically above 500°C for Al-Cu-Li, as there is a solubility limit in that area (Warner, 2006). At such temperatures, the solubility of copper and lithium in aluminium is increased compared to aluminium at room temperature, that, if quenched, results in an oversaturated aluminium matrix (Solberg, 2014) (Warner, 2006). From Table 1 in chapter 3 it can be seen that the alloying concentrations for a particular AA2196 alloy were 3.07 wt% Cu and 1.7 wt% Li, which, if every other alloying element is disregarded and the resulting weight percent is assumed to be aluminium, gives an atomic percent of 1.26% and 6.41 %, respectively. Consequently, at 500°C, AA2196 will be within the Al-phase region in Figure 2, thus dissolving any other phase present.

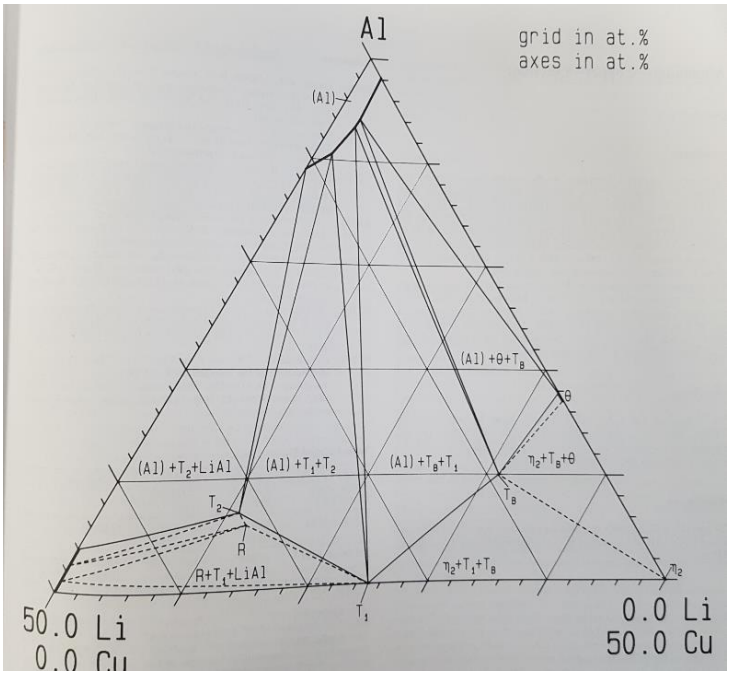

Figure 2 - Ternary phase diagram of Al-Cu-Li at T = 500°C (Petzow & Effenberg, 1991).

Due to rapid cooling the alloying elements are not able to diffuse at a sufficient speed, resulting in supersaturation at room temperature (Solberg, 2014) (Callister Jr & Rethwisch, 2015h). For solid solution heat treatment, there are two types, substitutional solid solution and interstitial solid solution (Dieter, 1988a). Substitutional solid solution strengthening is due to a small size difference between the matrix and the solute atom resulting in the solute atom participating in the matrix structure of the solvent atom (Dieter, 1988a). The lattice parameter may be used in order to determine whether the size difference is small enough for substitutional solid solution, and is required to be less than 15 percent (Dieter, 1988a). If the lattice parameter is larger than 15 percent, the solubility of the solute atom is mostly less than 1 percent (Dieter, 1988a). According to Callister and Rethwisch (2015b), the size difference may also be determined using the atomic radii, with the threshold value being less than 15 percent.

In addition to the size difference, the crystal structure, the electronegativity difference and the valence of the solute and the solvent play a role in determining whether the solute will be in interstitial or substitutional solid solution (Callister Jr & Rethwisch, 2015b). A similar crystal structure is required for the solute to be solved substitutionally (Callister Jr & Rethwisch, 2015b). Similarly, a large difference in electronegativity will result in the formation of an intermetallic compound instead of being solved in a solid solution (Callister Jr & Rethwisch, 2015b). There is also a susceptibility for metals to dissolve other metals with a higher valence rather than to dissolve a metal with a lower valence (Callister Jr & Rethwisch, 2015b)

In an interstitial solid solution, the solute atoms arrange in interstitial position, position between the matrix atoms (Callister Jr & Rethwisch, 2015b). These positions may be either octahedral or tetrahedral, depending on the number of neighbouring atoms, 6 or 4

respectively (Callister Jr & Rethwisch, 2015b). The impurity atoms are larger than the interstitial sites, and consequently produce lattice strain (Callister Jr & Rethwisch, 2015b).

One of the strengthening mechanisms is the elastic stress field generated from misfit atoms in the crystal lattice, impeding dislocation motion (Dieter, 1988a). The degree of strengthening is proportional to the size of the misfit atom (Dieter, 1988a). Substitutionally solved atoms only impede edge dislocations, while interstitially solved atoms also impede screw dislocations (Dieter, 1988a). Other factors that may influence dislocation motion, and thus strengthen the material, are modulus interactions in which the shear modulus of the matrix is altered, interactions with stacking-faults and that the solute atoms may become charged and interact with the electrical diploes of dislocations (Dieter, 1988a). Lastly, the solute atoms may cluster together or have more than the equilibrium number of neighbouring matrix atoms, both of which results in more energy required from a dislocation to move through that region (Dieter, 1988a)

Aluminium, copper and lithium all have a FCC structure, thusly they have the potential to solve substitutionally the other aforementioned elements if the size difference is sufficiently small(Frank et al., 2009) (Lossin, 2001) (Wietelmann & Steinbild, 2014). For aluminium and copper, the lattice parameters are 0.40496 nm at 25°C and 0.36152 nm at 20°C, respectively (Frank et al., 2009) (Lossin, 2001). The size difference is, therefore, less than 15 percent and thus, copper could potentially be solved substitutionally in aluminium, which is proven to be the case (Draissia & Debili, 2005). Due to the electronegativity difference between aluminium and copper in addition to copper having a lower valence than aluminium, +3 to +1, aluminium has a relatively low solubility of copper, < 1.8 at% (Draissia & Debili, 2005). According to Figure 2, the solubility of copper in an Al-Cu-Li alloy is less than 2 at%, which corresponds well with the aforementioned solubility limit mentioned by Draissia and Debili.

The atomic radius for lithium metal is 0.152 nm (Blackman, Gahan, Aylward, & Findlay, 2014), while the atomic radius is 0.143 nm for aluminium (Frank et al., 2009). This, in addition to the aforementioned match of crystal structure, allows for the possibility of lithium to be in a substitutional solid solution for an aluminium alloy (Alekseev & Lukina, 2016). Generally, Li is considered to have a high solubility in Al (Dursun & Soutis, 2014), however the solubility limit is discussed (Noble & Bray, 1998).

According to Alekseev and Lukina (2016), lithium may be present in an aluminium matrix in three possible ways, in a neutral substitutional solid solution, as a lithium ion in a substitutional solid solution and as a lithium ion in an interstitial solid solution. In a solid solution of Li in Al, 80% of the lithium atoms are solved substitutionally as a neutral lithium atom, while 16% are ions solved substitutionally and 4% are ions solved interstitially (Alekseev & Lukina, 2016). Figure 2 indicates that the solubility limit for Li in an Al-Cu-Li alloy is close to 11 at%. The high modulus of elasticity in AL-Li alloys may be explained due to a covalent component in the bonding of neutral Li atoms with neighbouring aluminium atoms (Alekseev & Lukina, 2016).

The storage time at room temperature is often controlled, as the material properties may vary due to changes in the microstructure (Marioara, Andersen, Jansen, & Zandbergen,

2003). An example of a cause of change in a material's properties is due to natural aging, and will be discussed below (Bray, Glazov, Rioja, Li, & Gangloff, 2001).

After solid solution strengthening, an alloy may be aged (Solberg, 2014). Aging may be subdivided into two categories, natural aging and artificial aging (Callister Jr & Rethwisch, 2015h). Both natural and artificial aging results in precipitation hardening, with natural aging occurring at room temperature, while artificial aging transpires at elevated temperatures (Callister Jr & Rethwisch, 2015h). In some alloys, natural aging is rapid (Bray et al., 2001), while in other alloys there is no measurable change (Hugaas, 1985).

According to Bray et al. (2001), there has been substantial research investigating the natural aging of 7xxx alloys, while for 2xxx alloys only a few such investigations have been undertaken. According to Deschamps et. al. (2013), AA2196 experiences natural aging due to the formation of δ′ particles which, among other things, causes a decrease in fracture toughness due to precipitation on grain boundaries. Previous work conducted seems to agree with Deschamps et al. that the alloy experiences natural aging, as the alloy was found to have a substantial hardness increase with time at room temperature after solutionising treatment at 530°C (Kyllingstad, 2018). For AA2196, the natural aging seemed to slow down after approximately 24 hours, seen in Figure 3(Kyllingstad, 2018).

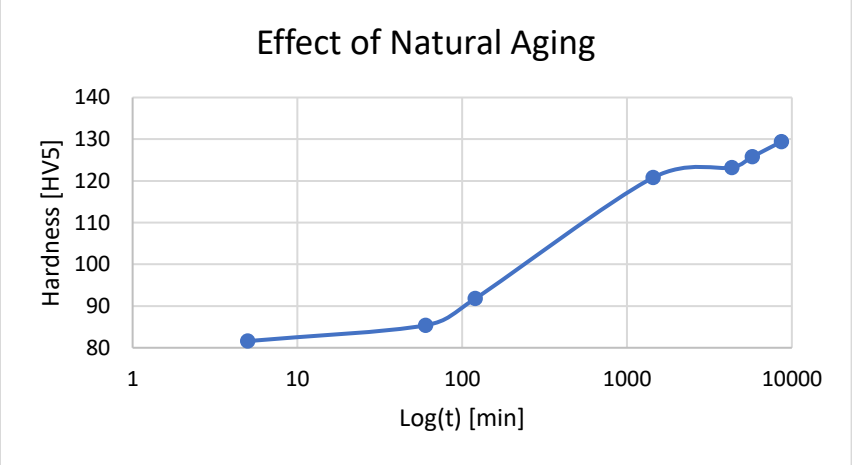

Figure 3 - The natural aging of AA2196. (Kyllingstad, 2018)

An aluminium alloy is generally precipitation hardened, and thus artificially aged, by heating the alloy to intermediate temperatures, e.g. just below 200°C for Al-Cu (Solberg, 2014). Due to the supersaturation of alloying elements at room temperature following solid solution heat treatment, small particles, precipitates, are formed when the alloy is heated to moderate temperatures. Precipitation hardening only occurs in alloys that have may have another alloying element in solid solution at elevated temperatures and where the solubility of that element decreases with a decrease in temperature (Dieter, 1988b). If the precipitate and the matrix match on an atomic level, they are said to be coherent, while if there is no atomic matching, then the precipitate is said to be incoherent (Dieter, 1988b). For a coherent precipitate, there will be some mismatch between the atomic lattice and the particle, resulting in distortion of the atomic lattice, and thus the emergence of stress fields which causes a strengthening of the material (Dieter, 1988b). Generally, the elasticity of a material is reduced during precipitation hardening (Callister Jr & Rethwisch, 2015h).

Precipitates generally increase the strength of the material in two distinct ways, either by forcing the dislocations to either cut through the particle at a higher strain than the strain required to move through the matrix itself, or to loop around the particle if the energy to cut through the particle is too high (Dieter, 1988b). Consequently, dislocation movement is lowered for both cases (Dieter, 1988b). Factors that affect the difficulty in which a particle may be shared are, among others, coherency strains, stacking-fault energies and the modulus of the precipitate (Dieter, 1988b). Generally, the strengthening effect increases with precipitate size (Dieter, 1988b).

In Al-Cu alloys, Guinier-Preston zones are formed firstly, followed by θ″, θ′ and θ respectively (Solberg, 2014). As GP zones and θ″ are formed, the hardness increases and the alloy is described as underaged (Solberg, 2014). Al-Cu alloys reach peak hardness when both θ″ and θ′ are present (Solberg, 2014). The rate of precipitate formation generally increases with temperature (Callister Jr & Rethwisch, 2015h). As θ′ are dissolved and stable θ are created, the hardness of the material decreases and the alloy is described as overaged (Solberg, 2014). Examples of underaging, peak hardness and overaging can be seen from Figure 4 and are respectively the left, top and right side of the graphs (Ringer & Hono, 2000).

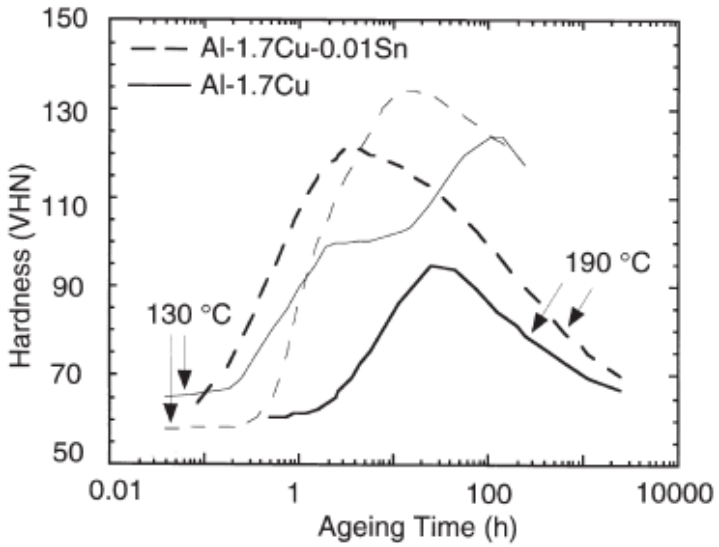

Figure 4 - Example of the link between hardness and aging time. The region left of the peaks are underaged, while the regions right of the peaks are overaged. (Ringer & Hono, 2000)

For third-generation Al-Li alloys, precipitation hardening temperatures ranging from 125°C to 160°C have been utilised in several cases (Elgallad et al., 2014) (Kim et al., 2016) (Deschamps et al., 2013) (Hekmat-Ardakan et al., 2012). AA2196 exhibits an aging behaviour resembling that of other Al-Cu alloys, seen in Figure 5. As seen, AA2196 experienced peak aging after approximately 100 hours, which was after peak hardness in the AA2198 was achieved (Deschamps, de Geuser, Decreus, & Malard, 2012). The initial higher hardness of AA2196 was most likely due to a larger fraction of δ′ precipitates (Deschamps et al., 2012). Due to the hardness of both AA2196 and AA2198 at peak hardness being relatively similar, δ′ most likely do not contribute to a large degree, and the main strengthening particle is assumed to be T_1 (Deschamps et al., 2012).

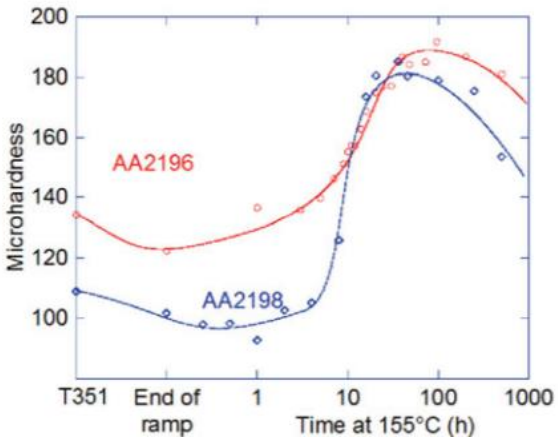

Figure 5 - Plot showing the precipitation curves for AA2196 and AA2198 aged at 155°C with respect to hardness. A "ramp" cosisting of heating at 20°C/h was used until 155°C was reached. (Deschamps et al., 2012)

Due to numerous alloying elements in AA2196, several precipitates may form, ranging from a considerable to negligible strengthening contribution (Elgallad et al., 2014) (Chen & Bhat, 2002) (Alekseev, Zhuravleva, Onuchina, & Klochkova, 2015). It is generally thought that $T_1(Al_2CuLi)$ and $\theta'(Al_2Cu)$ are the precipitates that gives the main strengthening contribution (Elgallad et al., 2014) (Chen & Bhat, 2002) (Metz, Weishaupt, Barkey, & Fairbee, 2012) (Kim et al., 2016) (Warner, 2006) (Deschamps et al., 2012) (Rioja & Liu, 2012) (Jiang et al., 2010) (Hekmat-Ardakan et al., 2012). T_1 additionally increases the toughness of the material and is thought to have favourable nucleation on dislocations (Rioja & Liu, 2012). A model for indicating what phases form during artificial aging may be seen from Figure 6 (Chen & Bhat, 2002). According to Figure 6, which gives the largest volume fraction of particles at 160°C (320°F) aged for 12 hours, the age hardening temperature and time used in this master thesis, should be T_1 and θ'. Worth noting is the fact that the TTP diagram only gives insight into the initiation of nucleation, therefore every region to the right of a curve is where the precipitate was present after heat treatment (Chen & Bhat, 2002).

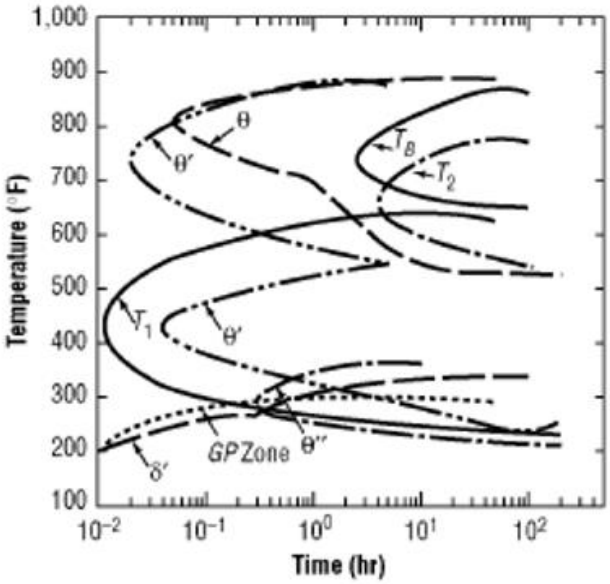

Figure 6 - TTP diagram showing the temperatures, in Fahrenheit, at which various phases were present after heat treatment (Chen & Bhat, 2002).

Alekseev et al. (2015) argues that the hardening effect of T_1 is overrated and that the main hardening mechanism is due to the δ′-phase (Al_3Li), often found in previous Al-Li alloys. Furthermore, there is some discussion regarding the existence and influence of an Ω and or Ω′ particle formed due to Ag additions in the alloy (Alekseev et al., 2015) (Rioja & Liu, 2012).

According to Elgallad et al. (2014) and Jiang et al. (2010), T_1 precipitates heterogeneously on dislocations formed during cold working and form a hexagonal platelet structure in the {111}-plane. This claim is supported by Wang & Shenoy (1998), who also argues that cold work can be used to promote a uniform distribution of T_1, as the dislocations function as nucleation sites. θ′ has a tetragonal structure and is partially coherent due to a size difference in the c-axis, thus causing little growth in the c-direction but growth in every other direction (Solberg, 2014) (Elgallad et al., 2014) (Jiang et al., 2010). Consequently, a resulting plate structure orienting itself in the {001}-plane is formed (Elgallad et al., 2014). Figure 7 indicates the structure of T_1, θ′ and δ′ as seen from a TEM, Transmission Electron Microscope (Rioja & Liu, 2012).

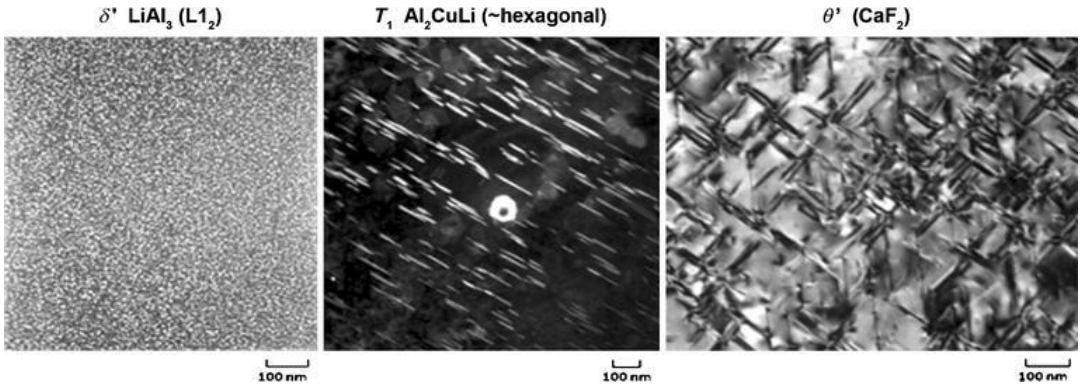

Figure 7 - TEM pictures indicating the structure of the proposed main strengthening particles, as well as δ´ (Rioja & Liu, 2012).

2.3 Temper Designation

AA2196, as delivered from Constellium, was subjected to a T8511 treatment (Uféras, 2017b). T8 treatment signifies that a material has been solid solution heat treated, followed by cold working and finally artificially aging (Solberg, 2014). Consequently, there will be a contribution to hardness due to both plastic deformation and precipitates in the matrix (Solberg, 2014). The final three digits, 511, signifies the relief of stress by stretching of the material after solutionising treatment, followed by minor straightening (The Aluminium Association Incorporated, 1979). Extrusions are stretched 1-3% (James, 1990).

The used heat treatment process in this master's thesis by first annealing, followed by cold rolling, solutionising heat treatment and finally precipitation hardening, is intended to correspond to plastic deformation that may occur during the reshaping of the material, followed by T6 treatment. In order to make the material more malleable, an annealing step was added. T6 treatment signifies solid solution heat treatment of the material, followed by artificial aging to max hardness (James, 1990). Compared to T8 treatment, where strain hardening contributes to the overall strength, there is only one major contributor in T6 treatment to strength (James, 1990). However, there may be a contribution to strength due to the grain size.

An aluminium alloy in the fabricated state is labelled F. This signifies that no special care or treatment has been utilized (James, 1990).

2.4 Grain Size and Nucleation of new Grains

The grain size is, as described in Callister (2015i), *"The average grain diameter as determined from a random cross-section".* A low grain size is generally considered to be beneficial, as a large grain size results in lower strength and lower hardness (Callister Jr & Rethwisch, 2015d). However, larger grains give a higher ductility(Witkin, Lee, Rodriguez,

Nutt, & Lavernia, 2003). In a fine-grained material, there is a larger total area for grain boundaries, which hinder dislocation motion, thereby increasing strength (Callister Jr & Rethwisch, 2015d).

After deformation, a material has an increased number of dislocations, resulting in a high energy state (Humphreys & Hatherly, 2004). Both creation of new dislocations and trapping of existing dislocations contribute to the increased dislocation density (Humphreys & Hatherly, 2004). A deformed material experiences an increase in grain surface area, and consequently also an increase in grain boundary area (Humphreys & Hatherly, 2004). Increased grain boundary area results in a higher energy state and is therefore a significant contributor to the higher energy state of a deformed material, compared to an annealed material. (Humphreys & Hatherly, 2004)

During annealing, the material is raised to sufficiently high temperatures that diffusion occurs, causing defects to either be annihilated or to be transformed into a lower energy state (Humphreys & Hatherly, 2004). During annealing, recovery, recrystallisation and grain growth may occur (Jazaeri & Humphreys, 2004). The annealing temperature may play a significant role in the resulting grain structure following annealing due to a larger driving force and the rate of diffusion increases (Klein, Schneider, Muske, Gall, & Fuhs, 2004).

Heat treatment at temperatures $\sim T_m/3$ following deformation results in recovery of the microstructure, the annihilation and rearrangement of dislocations (Humphreys & Hatherly, 2004). Both annihilation of dislocations and the rearrangement of dislocations from cell structures into low angle grain boundaries lowers the internal energy of the deformed material (Humphreys & Hatherly, 2004). The rearrangement of cell structures into low angle grain boundaries essentially transforms the cell into a sub-grain (Humphreys & Hatherly, 2004). Additionally, sub-grain coarsening may occur and their misorientation increase until the boundaries become high angle grain boundaries (Ahlborn, Hornbogen, & Köster, 1969). Due to the competition with recrystallisation, there rarely is a very large extent of subgrain coarsening (Humphreys & Hatherly, 2004).

If any further heat treatment is conducted, the material suffers recrystallisation and finally, grain growth (Humphreys & Hatherly, 2004). During recrystallisation, new grains are nucleated (Jazaeri & Humphreys, 2004). These particles are dislocation free and may grow by consuming neighbouring grains, thus lowering the dislocation density (Humphreys & Hatherly, 2004). Recrystallisation may thus provide a relatively dislocation free microstructure, but will still contain high energy grain boundaries (Humphreys & Hatherly, 2004). Recrystallisation occurs on inhomogeneities within a material, such as grain boundaries, second-phase particles or inhomogeneities due to deformation (Humphreys & Hatherly, 2004).

Further heat treatment will result in grain growth, where smaller grains are consumed by larger grains which grow and grain boundaries rearrange into a lower energy state (Humphreys & Hatherly, 2004). The driving force of recovery and recrystallisation is the aforementioned stored energy due to deformation (Humphreys & Hatherly, 2004). Figure 8 shows the change in certain properties during recovery, recrystallisation or grain growth. Due to the reduction in dislocation density, recovery and recrystallisation generally

decreases the strength and increases the ductility of the material (Humphreys & Hatherly, 2004).

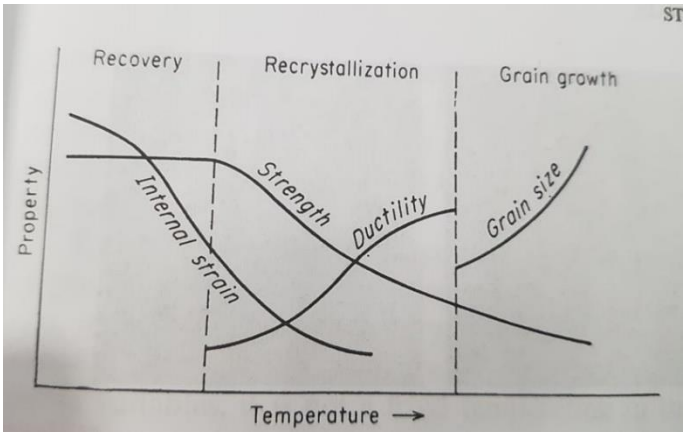

Figure 8 - Figure showing the change in properties during recovery, recrystallisation and grain growth (Dieter, 1988c).

Recrystallisation following deformation may reduce or increase the texture exhibited by a material (Humphreys & Hatherly, 2004). Particles larger than 1 μm may act as preferred nucleation sites, causing grains to nucleate in random directions, thus lowering the texture (Humphreys & Hatherly, 2004). It was found that in AA2195, coarse particles consisting of Al, Cu, Li and or Mg could function as favoured recrystallisation areas, while smaller particles impeded recrystallisation due to grain boundary impediment (Du, Zhang, Ye, & Liu, 2006). Additionally, recovered regions were experienced in the aforementioned AA2195 alloy (Du et al., 2006).

In several third-generation Al-Li alloys, Mg and Zr have been added in order to reduce recrystallisation observed during solutionising treatment, causing a reduction in the fracture toughness (Tsivoulas & Prangnell, 2014). For AA2198, a third-generation Al-Li alloy, Mg additions lead to increased recrystallisation and reduced texture due to the nucleation of grains with random orientation, compared to a another AA2198 alloy with Zr additions, resulting in an unrecrystallised structure and a clear cold rolling texture as seen before annealing (Tsivoulas & Prangnell, 2014). For Al-alloys that experience precipitation hardening, such as AA2196, sub-grains may be pinned by the precipitates, causing the retardation or suppression of recrystallisation (Engler, 1999).

Grain boundaries may generally be divided into two categories, high angle grain boundaries and low angle grain boundaries (Humphreys & Hatherly, 2004). High angle grain boundaries have a misorientation between two neighbouring grains of more than 10-15°, while low angle grain boundaries have a misorientation angle lower than this value (Humphreys & Hatherly, 2004). A low angle grain boundary is considered to be consist of a stack of dislocations and has a structure and properties that is a function of the misorientation (Humphreys & Hatherly, 2004). In contrast to a low angle grain boundary, a high angle grain boundary generally has properties and a structure that does not depend on the misorientation (Humphreys & Hatherly, 2004).

Subgrains are grains that have low angle grain boundaries and may be formed during the recovery process in a deformed material (Humphreys & Hatherly, 2004). Dislocations are either annihilated or form low angle grain boundaries, resulting in a lowering of the yield stress (Humphreys & Hatherly, 2004). By comparison with a recrystallised structure, a recovered structure has a higher energy, which may result in coarsening of the subgrain structure if further heat treatment is conducted (Humphreys & Hatherly, 2004). Recrystallisation and recovery may be seen as competing phenomenons, as the driving force in each process is the energy of the deformed structure (Humphreys & Hatherly, 2004).

2.5 Anisotropy

Some materials have similar properties in every direction and are therefore known as isotropic materials (Callister Jr & Rethwisch, 2015a). Other materials have varying properties depending on the direction examined, such materials are known as anisotropic (Callister Jr & Rethwisch, 2015a). Anisotropy is caused due to the symmetry in the crystal lattice, as varying unit cells have various planes of symmetry (Callister Jr & Rethwisch, 2015a). A material with a random orientation of grains is isotropic, while if there is a texture, an overall direction in the orientation of grains, then the material is anisotropic (Callister Jr & Rethwisch, 2015a). A material may, due to anisotropy, have material properties 20-50% lower in certain directions compared with other orientations (Engler & Randle, 2010). SEM and EBSD may be used to determine the texture of a material (Humphreys & Hatherly, 2004), by finding the individual orientations of grains (Engler & Randle, 2010).

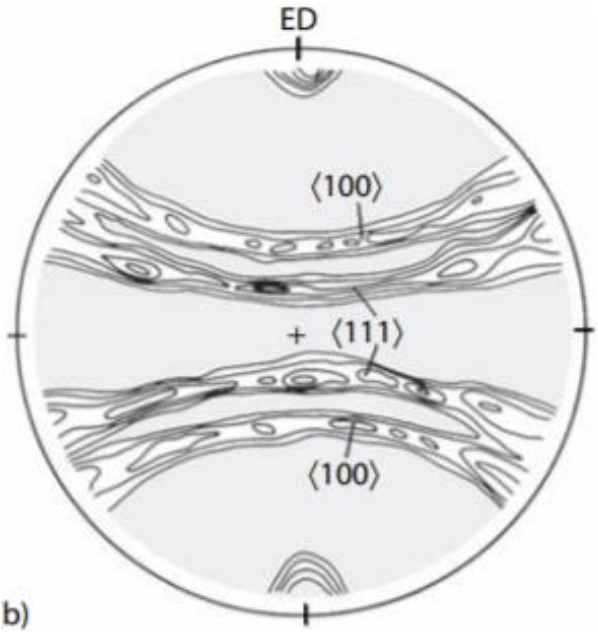

Pole figures may be utilized when describing the orientation of the crystal, with several pole figures required to properly describe the orientation (Engler & Randle, 2010). Various fabrication methods give rise to distinct pole figures, such as extrusion (Engler & Randle, 2010). In FCC metals, such as aluminium, extrusion results in a double fibre structure, in the ⟨100⟩ and ⟨111⟩ directions (Humphreys & Hatherly, 2004). Figure 9 indicates the pole figure of an Al-Li alloy, with the ⟨100⟩ and ⟨111⟩ fibres used to describe the corresponding texture (Engler & Randle, 2010).

Figure 9 - Pole figure for an extruded Al-Li alloy (Engler & Randle, 2010).

For a heavily deformed Al-Li alloy that has subsequently been annealed, there are two main types of recrystallisation texture that might occur, the cube orientation and the R orientation (Engler, 1999). Whereas the cube orientation is a new texture nucleated, the R orientation has similarities from the rolled S orientation and may nucleate on the deformation structure (Engler, 1999). Increased annealing time leads to reduced R oriented grains (Engler, 1999). Both recrystallisation and recovery may lead to the formation of a recrystallisation texture (Engler, 1999). From Figure 10, the pole figures for heavily deformed Al-alloys that were annealed can be seen. Each figure exhibits either both the cube and R orientation or one of them.

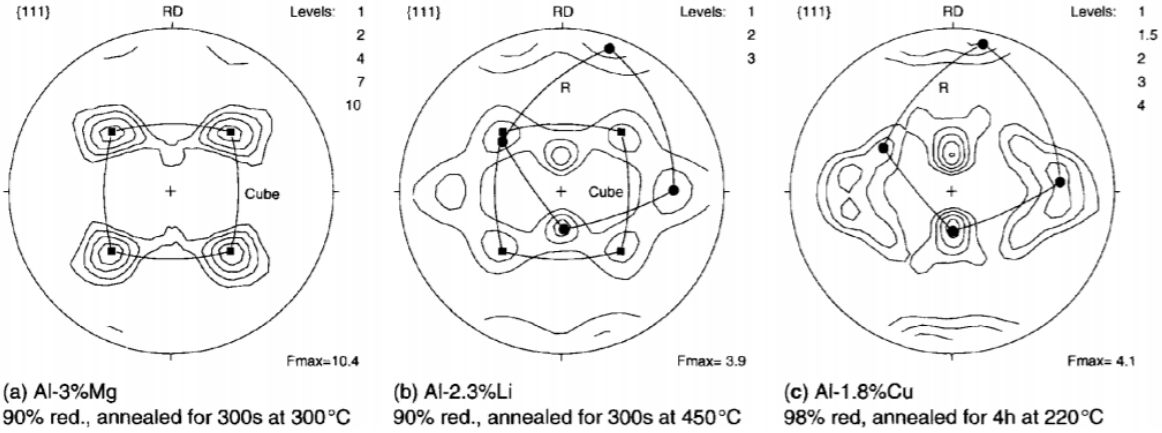

Figure 10 - (111) Pole figure for three heavily cold rolled Al-alloys which were subsequently annealed at various temperatures. a) Al-3%Mg alloy exhibiting cube orientation. b) Al-2.3%Li alloy exhibiting both cube and R orientation. c) Al-1.8%Cu alloy exhibiting heavy R orientation. (Engler, 1999)

An alternative to pole figures is to use inverse pole figures. Inverse pole figures can be used to describe fibres that may occur in a material (Engler & Randle, 2010). One such figure may be seen in Figure 11, which gives the inverse pole figure of uniaxially compressed pure Cu. Although Cu have a lower stacking fault energy than Al, which may affect the texture formed, FCC metals, such as Cu and Al, generally form ⟨110⟩ fibers during compression (Engler & Randle, 2010)

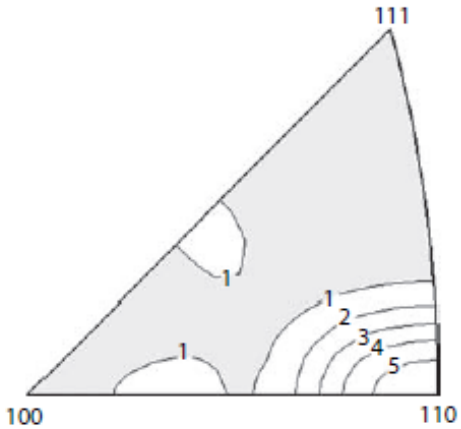

Figure 11 - Inverse pole figure of pure uniaxially compressed copper. There is a significant amount of ⟨110⟩ fiber, with some ⟨210⟩ fibers as well. (Engler & Randle, 2010)

2.6 Cold Working

Cold working, strain hardening at room temperature, increases the strength and the hardness of the material, at the cost of ductility (Callister Jr & Rethwisch, 2015e). Strain hardening increases the density of dislocations in the material, that have repulsive interactions with each other, resulting in a hindrance of dislocation motion, thereby making the material stronger (Callister Jr & Rethwisch, 2015e). For a precipitation hardened material with a low degree of strain hardening, dislocations cut through precipitates once the stress in the material is high enough, resulting in a low slope on a stress-strain curve (Dieter, 1988b). On the other hand, if a precipitation hardened material is exhibiting a high degree of strain hardening, dislocations no longer cut through the precipitates, but move around the particles, causing a high slope on the stress-strain curve (Dieter, 1988b).

Cold working results in high-density dislocation areas known as tangles, which, if further deformation is conducted, results in a cellular network where the dislocations constitute the cell wall (Dieter, 1988c). The cell size will decrease with increased deformation to a certain size, often experienced at approximately 10 %CW (Dieter, 1988c). The temperature at deformation, strain rate and type of material all influence the cell structure (Dieter, 1988c).

During cold working, the dimensions of one or two of the material are compressed, while the working direction is elongated, resulting in elongated grains (Dieter, 1988c). The orientation of individual grains changes with respect to that of the applied stress during the cold working, hence resulting in increased anisotropy (Humphreys & Hatherly, 2004). For cold rolling, the height of the sample is pressed by the roller, causing a length increase in the material and thus the grains. AA2196 was delivered as a round extrusion from Constellium, thus the material was deformed in two dimensions, both of the transverse directions, while experiencing elongation in the extrusion direction.

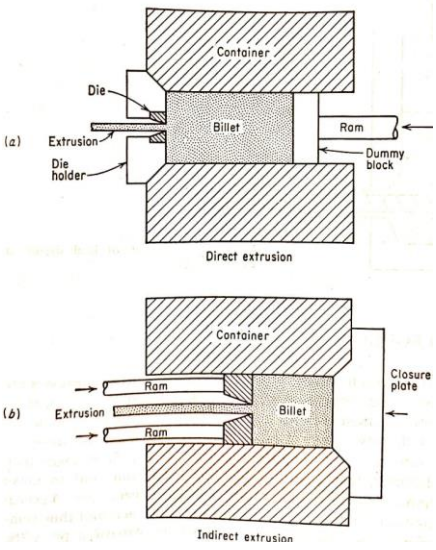

Extrusion is conducted by applying a compressive force from a ram onto a material, thus forcing the material through a narrow slit of the desired geometry (Dieter, 1988d). Figure 12 shows direct extrusion, in which the ram is moved on a stationary billet forcing the billet through a narrow die, and for indirect extrusion, where the ram is applying pressure in the opposite direction of the die and towards a closure plate, forcing the material through the die (Dieter, 1988d). Extrusion processes are generally conducted at an elevated temperature in order to increase the malleability of the material (Dieter, 1988d).

Figure 12 - Figure showing a) direction extrusion and b) indirect extrusion (Dieter, 1988d).

For third-generation Al-Li alloys, cold work prior to precipitation hardening may increase the strength and fracture toughness of the material (Rioja & Liu, 2012). This is due to the fact that precipitates are less likely to precipitate on grain boundaries and more likely to

precipitate on the heterogeneities introduced by the dislocations (Rioja & Liu, 2012) (Wang & Shenoy, 1998) (Jiang et al., 2010) (Hekmat-Ardakan et al., 2012). Cold work is measured in percent cold work, %CW, as seen from Equation 7 (Callister Jr & Rethwisch, 2015e). A_0 is the initial area and A_d the conclusive area.

$$\%CW = \left(\frac{A_0 - A_d}{A_0}\right) * 100 \tag{7}$$

Equation 7 - Percentage of cold work (Callister Jr & Rethwisch, 2015e).

2.7 Mechanical Testing

2.7.1 Tensile Testing

Tensile testing constitutes applying a tensile load on a prepared sample while carefully monitoring the elongation and force required to deform the material (Dieter, 1988e). As the material is deformed, yield strength, tensile strength and strain may be calculated using these parameters (Dieter, 1988e). Yield strength is commonly given as the offset yield strength at 0.2 percent plastic strain (Dieter, 1988e). This method of measuring the yield strength is used to avoid the elastic area (Dieter, 1988e).

A material experiences strain hardening during tensile testing, resulting in an increase in strength of the material and thereby demanding a higher load to continue deformation (Dieter, 1988e). Strain hardening is opposed by the decrease in cross-section area, resulting in a constant load giving a higher localised stress (Dieter, 1988e). Prior to necking, strain hardening has a larger contribution compared to the reduction of cross-section area, resulting in a demand for increased load if deformation is to continue (Dieter, 1988e). At maximum load, necking occurs (Dieter, 1988e). During necking, the contribution due to a reduction in cross-section area is larger than that of the strain hardening, resulting in a decreased engineering strength and thus a lower required load to continue deformation. (Dieter, 1988e).

Though the engineering stress may decrease during necking, the true stress experienced at the point of necking increases continuously until fracture (Dieter, 1988e). The difference is due to the assumption for engineering stress that the cross-sectional area is constant, while true strain considers the actual cross-section area for the point of necking (Dieter, 1988e). Consequently, true stress and true strain give a more accurate description of the stress-strain relationship, as seen from Figure 13 (Dieter, 1988e).

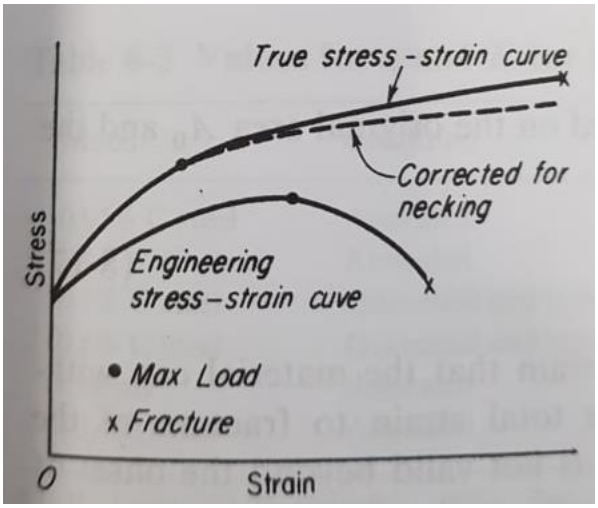

Figure 13 - Figure showing a comparison between a true stress-strain curve and an engineering stress-strain curve. (Dieter, 1988e)

True stress and strain are related to engineering stress and strain through Equation 8 and Equation 9 and are valid until necking (Dieter, 1988e). For Equation 8 and Equation 9 to be valid, a constant volume has been assumed.

$$\sigma_{true} = \frac{F}{A}(\varepsilon_e + 1) = \sigma_e(\varepsilon_e + 1) \tag{8}$$

Equation 8 - Equation for true stress (Dieter, 1988e).

$$\varepsilon_{true} = \ln(\varepsilon_e + 1) \tag{9}$$

Equation 9 - Equation for true strain (Dieter, 1988e).

For a tensile test sample the necked region is constructed for the region to emulate the behaviour of a mild notch (Dieter, 1988e). During testing the necked region experiences a triaxial stress state, with forces acting in the transverse and radial directions (Dieter, 1988e). The necked region and the forces acting in the necked region can be seen in Figure 14 (Dieter, 1988e). Both R, the curvature of the necking region, and a, the radii in the necking region, have to be carefully controlled (Dieter, 1988e).

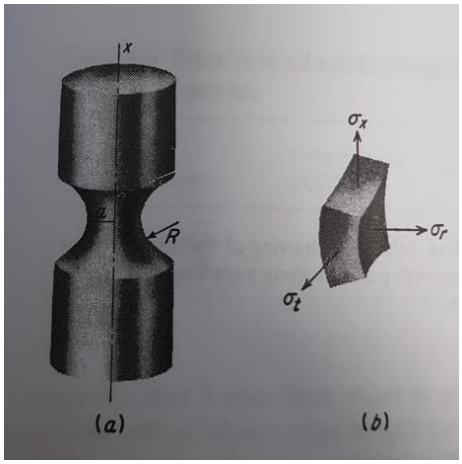

Figure 14 - a) Figure showing a tensile test sample and the necking region. b) Stresses acting on a certain point in the necking region. (Dieter, 1988e)

2.7.2 Charpy Testing

A type of impact testing is Charpy testing. Charpy testing utilizes a pendulum which is raised a certain height, giving it a certain energy (Dieter, 1988e). A standard Charpy sample has a 10 x 10 mm sample area and is notched with a 45° notch approximately 2 mm wide with a 0.25 mm root radius as seen from the NS-EN ISO 148-1:2016 standard seen in Appendix D. However, Charpy samples may also be constructed using a reduced thickness of 5mm instead of the standard 10mm. The raised pendulum has a giving known potential energy corresponding to the height raised, and a Charpy sample is placed at the lowest point in the strike area of the pendulum (Dieter, 1988e). The notched side of the sample is facing away from the area the pendulum strikes, as indicated by Figure 15 (Dieter, 1988e).

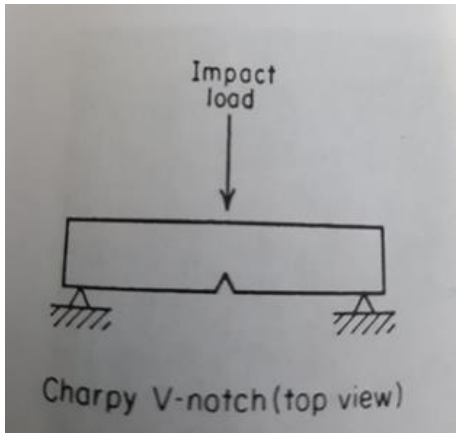

Figure 15 - Figure showing the loading method and impact area in a Charpy test (Dieter, 1988e).

When the pendulum strikes the sample, some of the mechanical energy of the pendulum is absorbed and fracture occurs (Dieter, 1988e). By measuring the initial and resulting height of the pendulum, the exact energy absorbed can be measured and thusly, the energy

required until fracture (Dieter, 1988e). Additionally, the fracture surface can be used to determine in the fracture was fibrous or granular, and thereby help describe how ductile a material is (Dieter, 1988e).

Compared to a standard Charpy test, an instrumented Charpy test provides the load-time relationship in addition to the fracture energy (Dieter, 1988e). Consequently, the maximum force, the energy until initiation of fracture, the initiation energy, and the propagation energy can be measured (Dieter, 1988e). Additionally, the load required to initiate yield, the fracture load and the maximum load subjected to a sample can be determined (Dieter, 1988e).

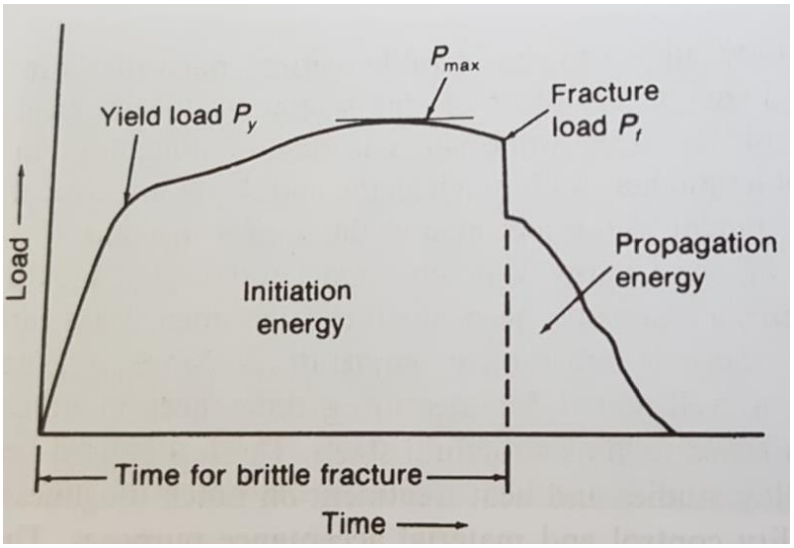

Figure 16 - The load-time relationship for an instrumented Charpy test. The fracture energy, the initiation energy and the propagation energy may be obtained.

2.8 Microscopy

Two alternatives when examining the microstructure of a sample are the OM, Optical Microscope, and the SEM, Scanning Electron Microscope. In an optical microscope, light is emitted from a light emitting source and reflected by a mirror onto the sample (Solberg, 2016). At the sample surface, the light is reflected through an eyepiece lens and an objective lens, resulting in magnification (Solberg, 2016). Polarized light is reflected differently in an anisotropic material, resulting in different colour patterns (Solberg, 2016). An aluminium alloy may be etched, resulting in an anisotropic coating on the sample surface with an orientation corresponding to the orientation of the surface (Solberg, 2016). Thus, the microstructure in a sample may be examined, with various grains showing different colours (Solberg, 2016).

A SEM functions by sending primary electrons with certain energies towards the sample surface (Hjelen, 1989). If these primary electrons collide inelastically with loosely bound electrons in the sample, some electrons are ejected out of the sample as secondary

electrons, which is utilized in a SEM (Hjelen, 1989). Some primary electrons are reflected from the surface and are thusly named backscattered electrons (Hjelen, 1989). Grains with different orientations will result in different diffraction angles, θ, following Braggs law, as seen from Equation 10 (Prior et al., 1999). λ is the wavelength, n a positive number and d is the interplanar spacing (Prior et al., 1999).

$$n\lambda = 2dsin(\theta) \tag{10}$$

Equation 10 - Braggs law (Prior et al., 1999).

Backscattered electrons create diffraction patterns that may be detected on a phosphorus screen and utilized using EBSD, Electron Backscatter Diffraction (Prior et al., 1999). Consequently, the microstructure and texture may be described(Prior et al., 1999). EBSD detectors are paired with a SEM and require that the sample is tilted a large angle relative to the incident primary electrons, in this case, 70°, to be able to collect the backscattered electrons (Prior et al., 1999) (Hjelen, 1989).

3. Experimental Procedure

As seen from Table 1, the AA2196 extrusion delivered contained 3.07 wt% Cu and 1.7 wt% Li, in addition to small additions of Mg, Mn, Ag and Zr. According to Figure 74 in Appendix A, initial yield strength and tensile strength in the longitudinal direction were both found to be approximately 653 and 647 MPa, while in the transverse direction it was 530 MPa and 505 MPa, respectively. Additionally, Figure 74 in Appendix A gives a full overview of the material characteristics and the alloying elements.

Alloy	***wt% Cu***	***wt% Li***	***wt% Mg***	***wt% Mn***	***wt% Ag***	***wt% Zr***	***wt% Zn***
AA2196	3.07	1.7	0.33	0.32	0.27	0.11	0.06
AA7090	0.3-0.8	NA	2.6-3.2	0-0.05	NA	0.1-0.2	8.0-9.0

Table 1 – Main alloying elements in the delivered AA2196 extrusion and for AA7090. NA, i.e. not applicable, has been used when no information has been given.

A 0.5-meter long extrusion of AA2196 with a diameter of 70 mm was delivered from Constellium in a T8 state. The billet was extruded indirectly. For the purposes of this master thesis, it has been assumed that the delivered material was homogenous throughout the 0.5m long extrusion.

AA7090 was supplied by NAMMO Raufoss as either an extruded bolt with 65 mm diameter or a 0.5m long, 10mm high and 50mm wide extruded profile. Both the bolt and the profile were directly extruded at 490°C with a speed of 1m/min, with billet diameters of 203mm and 98mm respectively. Alloying elements for AA7090 is also seen in Table 1.

At delivery AA7090 was in a fabricated state, labeled F. Samples were cut using similar equipment to that of AA2196. Charpy samples was created from solely the extruded profile. The 0%CW AA7090 tensile testing samples were made from the extruded bolt and the rest were made from extruded profiles. Samples used to create the aging curve were from the extruded bolt.

3.1 Cutting of Samples

The extrusion was initially cut into 15 cm long rods with a cross-section area of approximately 15 by 15 mm or into slices with a 70 mm diameter and a length of 15 mm. The cross-section of the extrusion and how the extrusion was cut into rods may be seen from Figure 17. The rods were cut such that the length of the rod corresponded to the extrusion direction of the extrusion. To minimize the material used to create the aging curves, the pieces were cut into roughly 15 mm cubes using a Stuers Labotom with a 10S25 blade.

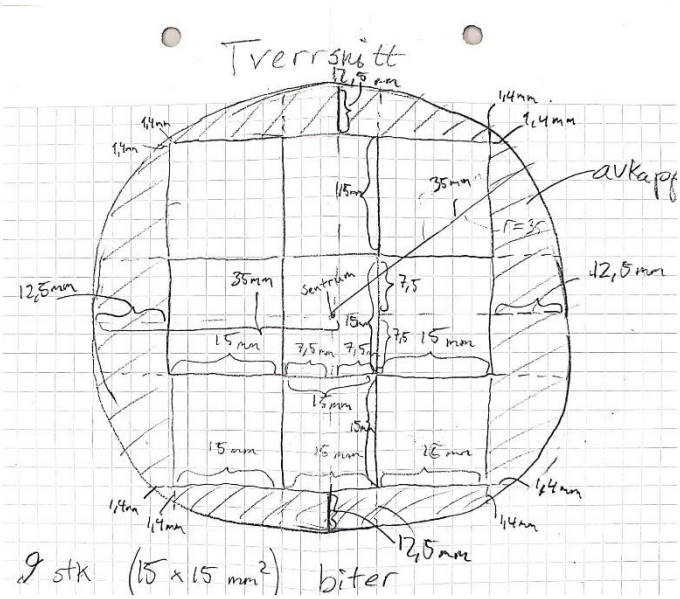

*Figure 17 - The drawing of the cross-section area used by the workshop at Sintef Manufacturing to cut the AA2196 extrusion into 15*15*150mm rods.*

3.2 Heat Treatment Conducted

The temperature and time chosen for both solid solution treatment and artificial aging have been chosen based on a combination of a literature review and due to practical considerations. While a lower temperature might result in a higher peak strength, the time to reach said peak strength may be long. Consequently, 160°C has been chosen as the precipitation hardening temperature. Similarly, due to a relatively short holding time and muffle furnaces unsuited to rapid heating, 530°C has been chosen.

Every heat treatment step for AA2196 and AA7090, except for the solid solution treatment of AA7090, was conducted using three muffle furnaces created by Nabertherm, provided by NTNU and named; N17/HR, N15/65HA and N11/R. For solid solution of AA7090, a salt bath was used. The AA2196 extrusion was initially in a T8 state, thus annealing was required in order to remove any previous heat treatment and get the material ready for further heat treatment. Consequently, AA2196 was annealed at 400°C for 2 hours, before it was cooled down to 250°C at a speed of 0.5°C/min, giving a total of 7 hours. Subsequently, the door to the muffle furnace was opened to give a faster cooling. During both annealing and solutionising treatment, every aluminium sample was covered in aluminium foil to protect the samples from reacting with oxygen in the air.

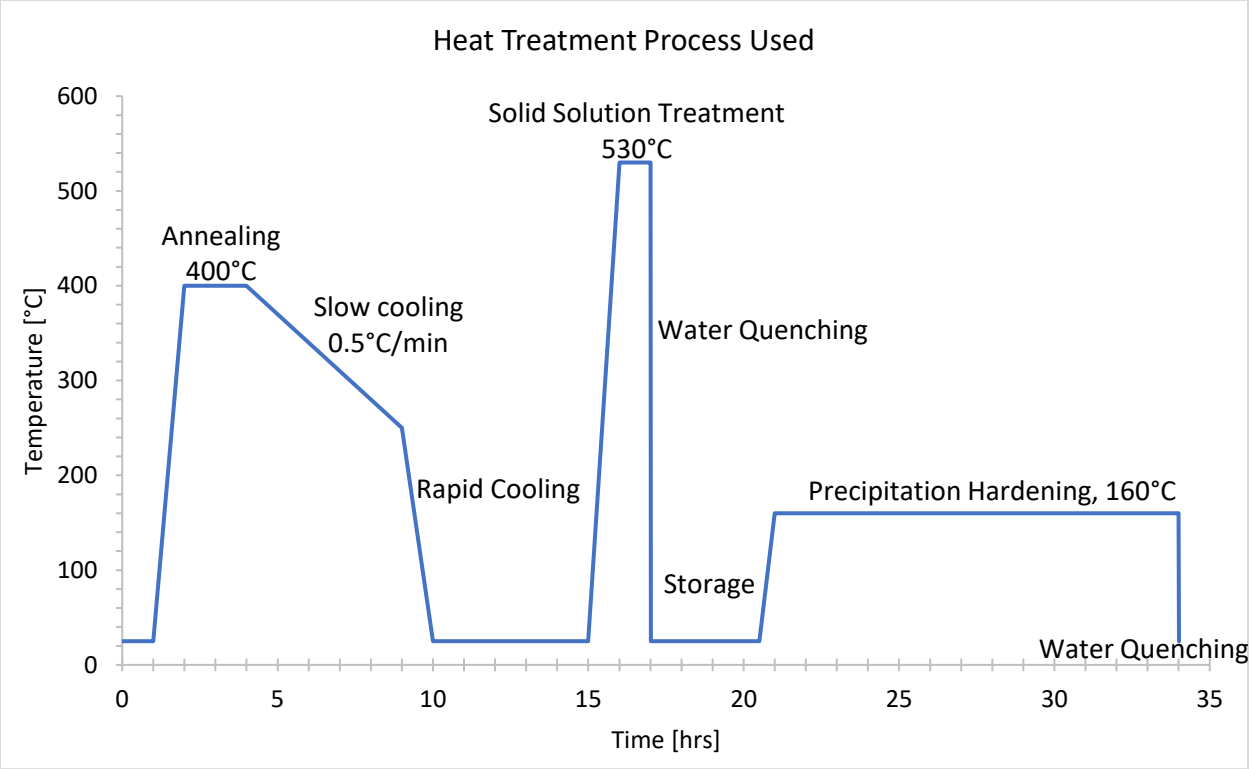

Figure 18 - Process diagram of the proposed T6 process. Storage time shortened in the figure to improve readability.

8 cubic 15mm samples of AA2196 were solutionised at 530°C for 1 hour and subsequently precipitation hardened at either 150°C or 180°C for a length varying from 8 to 20 hours, as seen in Table 2. Prior to aging, the samples were naturally aged for 24 hours.

Alloy and Sample Number	***Solutionising Treatment Temperature [°C] and Time***	***Precipitation hardening Time [hrs]***	***Precipitation Hardening Temperature [°C]***
AA2196 - 1	530 – 1 hr	8	150
AA2196 - 2	530 – 1 hr	12	150
AA2196 – 3	530 – 1 hr	16	150
AA2196 – 4	530 – 1 hr	20	150
AA2196 – 5	530 – 1 hr	8	180
AA2196 – 6	530 – 1 hr	12	180
AA2196 – 7	530 – 1 hr	16	180
AA2196 - 8	530 – 1 hr	20	180

Table 2 - Table showing heat treatment conducted for AA2196 to obtain age hardening curves.

Contrary to AA2196, AA7090 was annealed at 410°C for two hours. Afterwards, the alloy was cooled to 250°C at a rate of 0.5°C/min. Solutionising treatment was conducted using a two-part process. Firstly, AA7090 was preheated in a muffle furnace at 200°C for 20 minutes, in one of the aforementioned muffle furnaces, before it was emerged into a salt bath, "Saltbad 5" or "Saltbad 6", at 480°C for 20 minutes. Subsequently, the alloy was quenched in water at room temperature. Age hardening for the AA7090 cubic samples was conducted utilizing two muffle furnaces, N11/R and N15/65HA, at 120°C. Samples were age hardened from 8 to 24 hours, as seen in Table 3.

Alloy and sample number	***Age hardening time [hrs]***	***Age hardening temperature [°C]***
AA7090 – 1	8	120
AA7090 – 2	12	120
AA7090 – 3	16	120
AA7090 – 4	20	120
AA7090 – 5	24	120

Table 3 - Table indicating the age hardening time and temperatures performed on AA7090.

Charpy samples and tensile testing samples of AA2196 were annealed using the abovementioned process, solutionised at T=530°C for 1 hour, allowed to naturally age for 24 hours and precipitation hardened at 160°C for 12 hours. All heat treatment for these samples was conducted using either N15/65HA or N17/HR.

For heat treatment conducted on any Charpy sample or tensile test sample of AA7090, the samples were homogenised in a muffle furnace at 490°C for 4 hours. At least 90 minutes were spent in the 250-400°C region, during heating to the homogenisation temperature. Subsequently, the samples were heat treated according to the heat treatment mentioned in the previous paragraph. The heat treatment of AA7090 is based on internal documents at NAMMO Raufoss. N15/HA and N17/HR were used to conduct the heat treatment.

It was found that a furnace, N11/R, did not heat samples to the designated temperature, hence causing mistreatment of several samples. As there was no record of which samples that were affected, a list providing the samples that may have been affected is instead listed in Table 4.

Type	***Description***
Precipitation curves	All
Pressed samples	All
Tensile testing rods	0%CW AA7090
Charpy samples	None

Table 4 - Table showing the samples that might have been heat treated by N11/R.

3.3 Preparation and Testing of Tensile Testing Rods

All tensile testing samples were constructed by "Finmekanisk verksted" at NTNU. All tensile testing rods were round. Two different sizes were used for the tensile testing rods, seen in Appendix D as Figure 97 and Figure 98.

For approximately 10%CW AA2196, 0% CW AA7090 and for AA2196-T8511 tensile testing rods with a diameter of 10mm at the head, 6mm in the necking region and a length of 109.6 mm were used.

Due to size limitations for the samples cold worked 19.0%, 39.0% and 56.3% for AA2196 and 9.2%, 18.6% and 39.1% for AA7090 a smaller variation of tensile testing rods was used, with a diameter of 5mm, a necking region of 3mm and a total length of 70mm.

Tensile testing was conducted until fracture using an MTS 810 Hydraulic Tensile tester machine 100 kN, "Hydraulisk Strekkprøvetester" in Norwegian, a 647 Hydraulic Wedge Grip and an extensometer, as seen in Figure 19. The strain rate was 2.000 mm/min. For several tensile test samples, the Walter & Bai Hydraulic tensile testing machine 100kN was used instead of the MTS 810 Hydraulic tensile tester machine seen in Figure 20.

Figure 19 - Tensile test setup for MTS 810 Hydraulic Tensiletestermachine.

Figure 20 - Walter & Bai Hydraulic tensile testing machine 100kN.

3.4 Charpy Testing

Charpy samples prepared for impact testing were constructed according to the NS-EN ISO 148-1:2016 standard, seen in Figure 99 in Appendix J. A slightly downsized variation with a width of 5 instead of 10 mm were used in order to save material.

Due to the thickness of the AA7090 samples delivered being only 10 mm, it was not possible to cold roll AA7090 to 60% and still create Charpy samples. The respective alloy and their degree of cold work can be observed in Table 5. The Charpy samples were notched in the transverse direction.

Cold worked samples made into Charpy samples					
Alloy	***0%CW***	***10%CW***	***20%CW***	***40%CW***	***60%CW***
AA2196	Yes	Yes	Yes	Yes	Yes
AA7090	Yes	Yes	Yes	Yes	No

Table 5 - Table showing which alloys and which cold worked samples that were made into Charpy samples.

The Charpy tester used was an Instron MPX 450. The following calibration settings were used: the weight was 32.475 kg, the latch angle was -149.832 and the friction angle was 0.630. The calibration date was in March 2019 and according to the standard ISO148-02.

Figure 21 - The Charpy tester used.

3.5 Grinding and Polishing

All samples were grinded before hardness testing to a maximum grain size of 22 µm using either a Saphir 330 or a Stuers RotoPol-21 with a SiC paper. The coarsest paper used was FEPA P#800 which gives the aforesaid grain size of 22 µm. Between each paper used the samples were rinsed with water and after the final grinding, with ethanol as well to prevent any reaction with water.

Before OM and SEM the samples required polishing. A Stuers DP-U3 using a Stuers MDMol polishing sheet with a 300 mm diameter, a lubricant of 5-15% ethylene glycol and 95-85% ethanol and a DP-Suspension P spray of first 3 µm diamond particles, and lastly 1 µm particles, were used to obtain a fine enough grain size.

Vibration polishing was utilized to polish samples sufficiently for SEM, using a Buehler VibroMet 2 vibratory polisher with a Buehler MasterMet 2. The amplitude was set at 60%-80%, with samples polished between 1 hour and 72 hours.

3.6 Hardness Measurements

Hardness testing was conducted utilizing a Zwick/Roell ZHV30 hardness tester with 15 seconds dwell time and a load of 5kgf. The analysing program Zwick Roell ZHµHD was employed to measure the indented area and to calculate the hardness. All hardness values are given in Vickers hardness (HV).

3.7 Cold Rolling

AA2196 and AA7090 were cold rolled 10-60% using rollers with diameters of 200 mm. Cold rolling was conducted in the extrusion direction. The roller was lubricated using oil. The height was adjusted such that the rods were rolled less than one millimetre each time through the roller. The roller can be seen in Figure 22.

Figure 22 - Roller used for cold rolling.

3.8 Cold Pressing of Samples

15 mm cubic samples were cold pressed in a "1000 kN MTS 311 Hydraulic Press". A speed of 2 mm/minute was used, with a layer of Teflon added below and above the sample to reduce friction, as seen in Figure 23. Samples were pressed in either the extrusion direction or in the transverse direction.

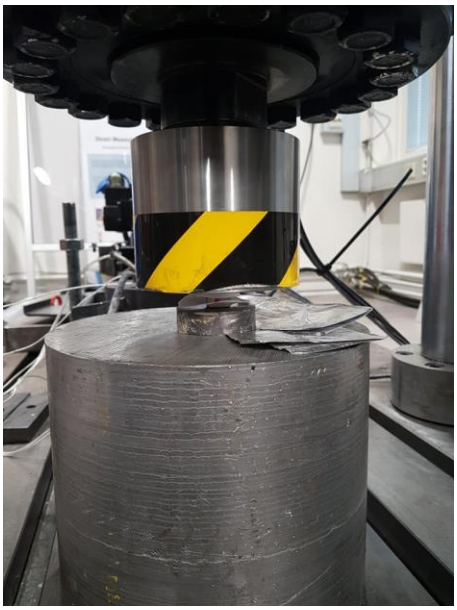

Figure 23 - Picture showing a pressed sample and the hydraulic press.

3.9 Data Logging of Furnace Temperature

An Omega HH1384 data logger was used as the logging instrument, while three thermocouples type K were utilised as sensors in order to determine the muffle furnace temperatures. The data logger was set to automatic recording, with one logging occurring every 10 seconds. The uncertainty of the data logger when using thermocouples type K in the range of -100-999°C was ±0.05% of reading or ±1°C, whichever were the largest. Additionally, the sensors have an uncertainty of either ±2.2°C or ±0.75% of reading. It has been assumed in this master's thesis that the best description of the combined uncertainty for the data logger and the sensor is to use the sum of the two uncertainties. Consequently, ±3.2°C or ±0.8% of reading has been used.

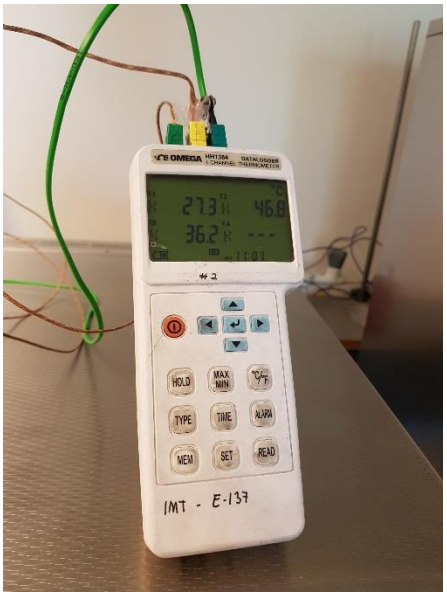

Figure 24 - The data logger used during testing with the thermocouples connected.

An AA2196 disc was used as the test material, seen in Figure 25. The height was approximately 15 mm, while the diameter was that of the extrusion. A hole was drilled into the sample to find the temperature of the sample instead of the temperature in the furnace. The sample, and every other heat-treated material, was placed on a stone, thus having one side that worked effectively as an insulator source during heat treatment. The setup can be seen in Figure 25.

When constructing time-temperature plots from the loggings, an estimate of the display temperature has been used, in which constant heating has been assumed. Consequently, if a furnace was set to go from 100 to 200°C in 100 minutes, this would result in 1°/min in the plot.

Figure 25 - The AA2196 sample piece used when measuring the temperature inside the alloy with respect to that of the furnace.

Figure 26 - Setup with a thermocouple inside the sample and a thermocouple in the air just above the sample.

3.10 Microscopy

After polishing, specimens selected for investigation in the OM were anodised by employing a 5% HBF_4 solution in a steel cup connected to a power supply, while the power supply was connected to the sample simultaneously. The surface area to be examined in the microscope was submerged in the HBF_4 solution for 90 seconds. The microscope used for all samples was a LEICA MEF4M type 381401 microscope. Pictures were captured using the computer program ProgRes CapturePro v2.8.8.

Specimens chosen for examination in the SEM were vibration polished instead of anodised. A Hitachi SU6600 FEG SEM owned by NTNU was used to analyse the samples. The microscope was equipped with an EBSD apparatus. For analyzation of the electron pictures, the computer program NORDIF was used. The working distance ranged from 23 to 24 micrometres, the voltage was 20 kV, the "High Current Analyisis Mode" was used and the tilting angle was 70°. Magnification was 50X. The computer program "TSL OIM Data Collection 7" was used for indexing the Kikuchi pattern.

Indexing was done utilizing the program "TSL OIM Data Collection 7". Pole figures were constructed using the computer program "TSL OIM Analysis 7" after indexing of the pattern. The grain angle tolerance used was 5°, while the minimum grain size was 2µm.

Due to every direction other than the extrusion direction having similar properties, as AA2196 was extruded, there have been made no distinction between the normal and transverse direction and both of these directions are mixed interchangeably as "the transverse direction" and "the second transverse direction".

3.11 Determination of Material Data

The engineering stress was found using Equation 1, while Equation 2 was utilized in order to determine the engineering strain.

The %elongation was found by employing Hooke's Law, Equation 3, to calculate the amount of elastic strain at the point of fracture using the true fracture stress and the respective modulus of elasticity. For AA2196 76.5GPa was used, while for AA7090 72 GPa was used. This value was then subtracted from the engineering fracture strain in order to find the plastic fracture strain. Equation 4 was then utilized to get %Elongation. Specific strength was found by utilizing Equation 6. Equation 7 has been used throughout this thesis to determine the amount of cold work undergone by a sample or rod.

True stress was found by using Equation 9 while Equation 8 was used to find the true stress. Constant volume has been assumed and the necking region has been removed from true

stress-strain graphs. Strain hardening was found by subtracting the engineering yield strength of the tensile strength, thus finding the strength increase due to cold work.

The tensile toughness was found by employing the trapezoid method, finding the area for a trapezoid using $0.5*(f_2+f_1)*(x_2-x_1)$, and then summarizing every trapezoid.

The thickness/diameter of tensile test rods was measured prior to tensile testing, giving the initial area as the samples were round. To calculate the reduction in area, the resulting height was required. To obtain the resulting diameter of the samples, the broken pieces were put together, as illustrated in Figure 27. While the two pieces were held together, the thickness was measured. The diameter was measured using a sliding gauge. Calculations were done by employing Equation 5.

Figure 27 - Figure showing how the samples were held together when measuring.

4. Results

4.1 Cold Work due to Pressing

5 samples were pressed with a hydraulic press, resulting in various percent of cold work, as seen in Table 6. Some samples were pressed in the transverse direction and some in the extrusion direction.

Number	***Pressing direction***	***Initial height [mm]***	***Resulting height [mm]***	***Percent cold worked [%CW]***
1	Extrusion	15.23	13.69	10.1
2	Extrusion	14.73	11.80	19.9
3	Transverse	15.00	8.98	40.1
4	Transverse	14.99	6.19	58.7
5	Extrusion	14.12	8.40	40.5
6	Extrusion	13.26	5.90	55.5
7	Transverse	15.09	13.97	7.4
8	Transverse	15.17	12.34	18.7

Table 6 – Table showing the initial and resulting height and resulting cold work for various samples pressed in either the transverse or the extrusion direction. All samples had an area of 15*15mm and a height given in the table above.

A ninth cubic sample was cold worked more than 70% in the extrusion direction, but this sample suffered cracking, as seen in Figure 28.

Figure 28 - Image showing cracks in a cubic sample cold pressed more than 70%.

4.2 Cold Rolling of Samples

Several samples of both AA2196 and AA7090 were cold rolled in the range of 10-60% using the cold roller mentioned in 3.7. The percent cold work conducted on each rod is given in Table 7. For some rods, an average of the height values for each end were used, seen in Table 21 in Appendix C.

Alloy and sample number	***Initial height [mm]***	***Resulting height [mm]***	***Percent cold worked [%CW]***
AA2196 - 1	15.12	12.25	19.0
AA2196 – 2	15.18	12.29	19.0
AA2196 – 3	14.99	13.62	9.1
AA2196 – 4	15.08	13.53	10.3
AA2196 – 5	15.21	12.21	19.7
AA2196 – 6	14.96	11.73	21.6
AA2196 – 7	14.44	12.70	12.0
AA2196 – 8	12.57	7.67	39.0
AA2196 - 9	12.55	5.49	56.3
AA2196 – 10	12.52	10.12	19.2
AA7090 – B3	9.85	8.94	9.2
AA7090 – B4	9.65	4.41	55.2
AA7090 – B5	9.82	7.99	18.6
AA7090 – B6	9.83	5.99	39.1

Table 7 - Table showing the respective alloy and sample number of cold rolled samples used for tensile testing and Charpy testing.

4.3 Grain Structure and Grain Size Observed after Cold Working

4.3.1 By Optical Microscope

Figure 29 shows the microstructure of AA2196 as delivered in a T8511 state. Image was taken from previous work (Kyllingstad, 2018). A fibrous structure may be seen.

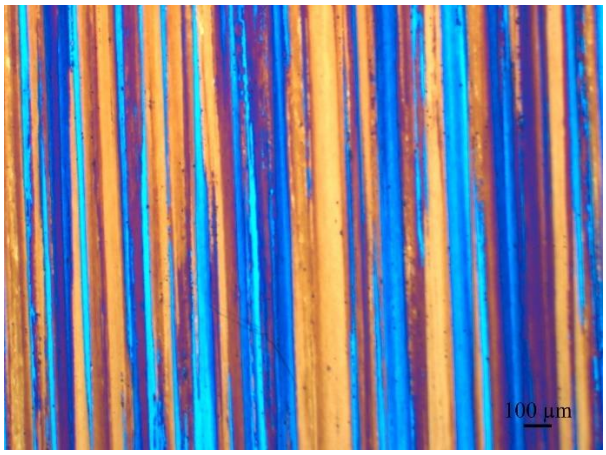

Figure 29 - The microstructure of AA2196 in a T8511 state as delivered. (Kyllingstad, 2018)

Samples cold worked by pressing, see 4.1, and a non-deformed sample was examined in an optical microscope. All samples were examined in both transverse directions, as well as the extrusion direction. Grain sizes were found for the extrusion direction using a SEM and an EBSD detector. Figure 30 to Figure 33 shows the microstructure in the extrusion direction and for one transverse direction for samples cold pressed 10.1-55.5% in the extrusion direction. Figure 34 to Figure 37 indicates the extrusion direction and the pressed transverse direction for samples cold pressed 7.4-58.7% in one of the transverse directions. To limit the number of pictures, images showing the second, and non-pressed transverse direction, have been moved to Appendix D. In Appendix D, Figure 75 to Figure 78 shows the second transverse direction when pressed in the extrusion direction, while Figure 79 to Figure 82 shows the non-pressed transverse direction for samples pressed in the transverse direction.

The average grain size seems to decrease with an increase in cold work for samples pressed in the extrusion direction, while the grain size in the transverse direction for the same samples seems to increase. For samples pressed in the transverse direction, the average grain size seems to decrease in all directions, although not significantly in the pressed direction.

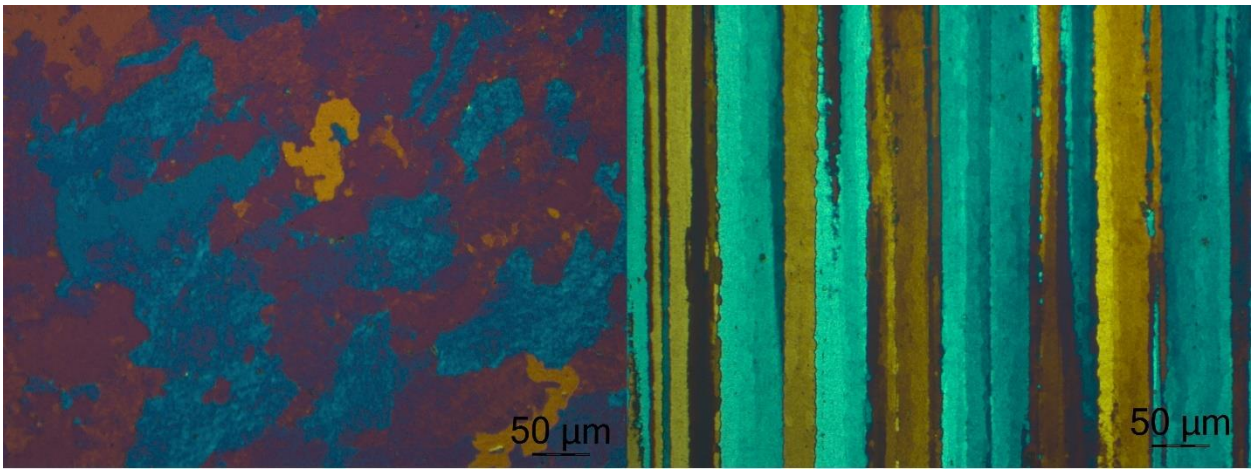

Figure 30 - Image of the microstructure in the extrusion direction and the transverse direction respectively for a 10.1%CW sample pressed in the extrusion direction.

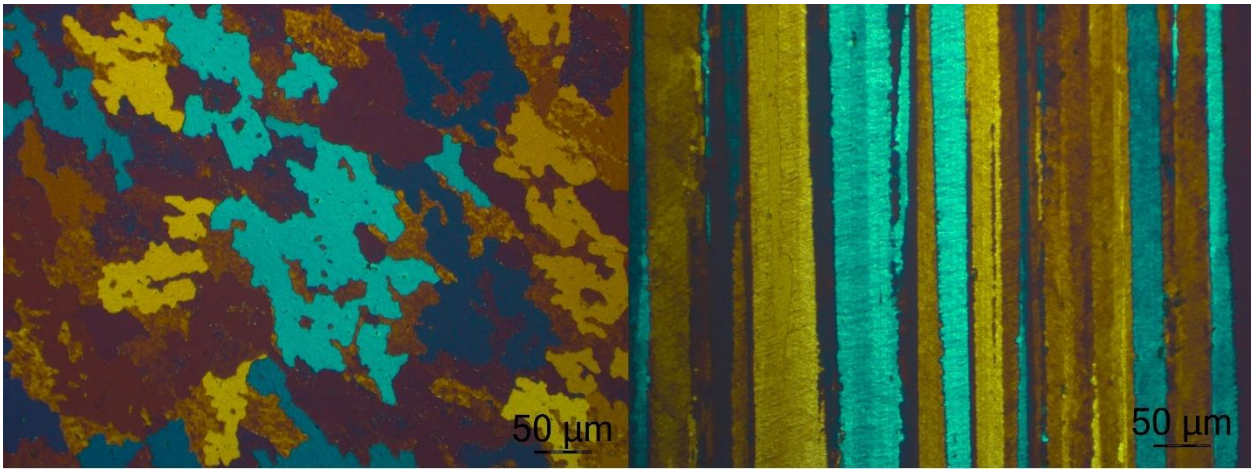

Figure 31 - Image of the microstructure in the extrusion and the transverse direction respectively for a 19.9%CW sample pressed in the extrusion direction.

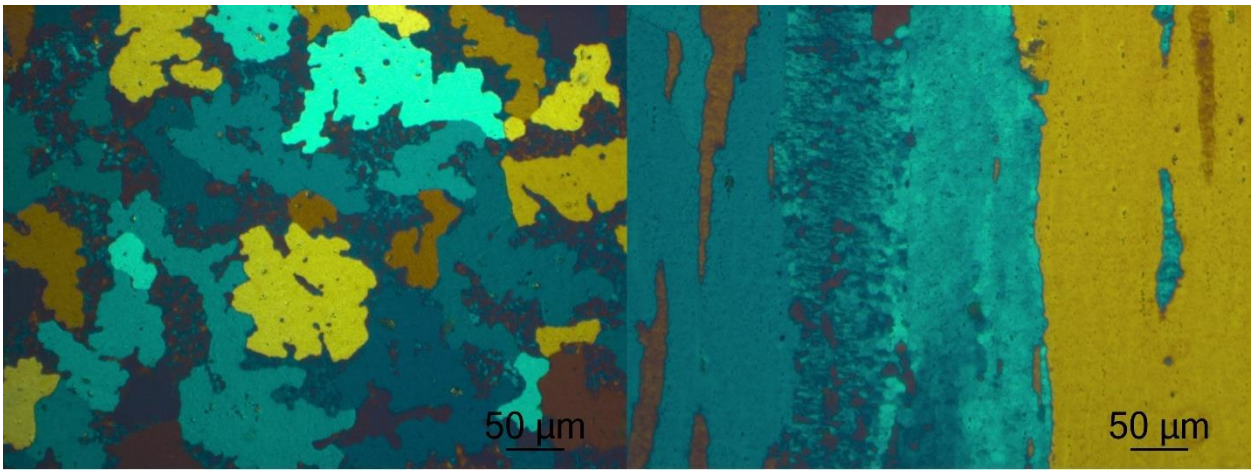

Figure 32 - Image of the microstructure in the extrusion and the transverse direction respectively for a 40.5%CW sample pressed in the extrusion direction.

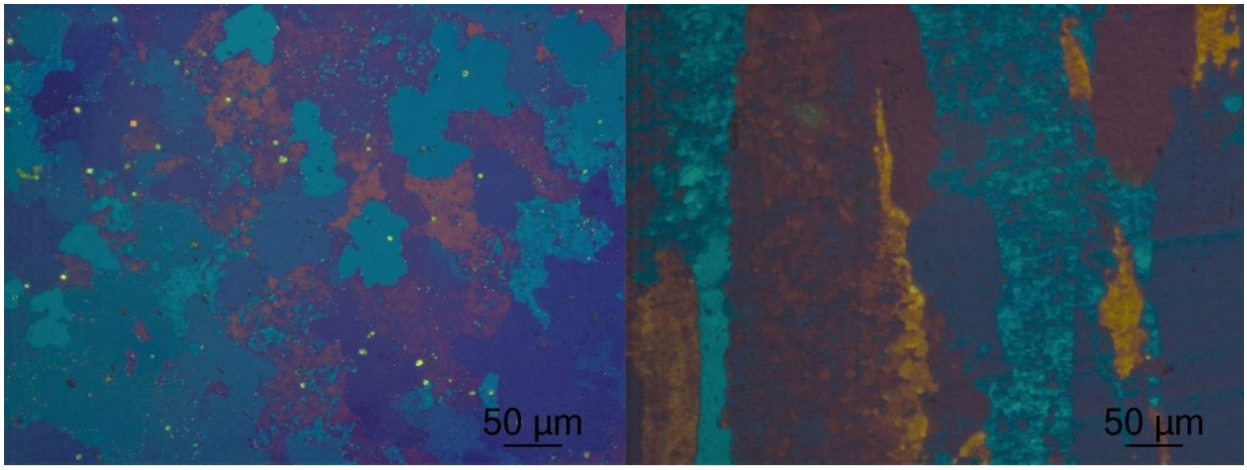

Figure 33 - Image of the microstructure in the extrusion and the transverse direction respectively for a 55.5%CW sample pressed in the extrusion direction.

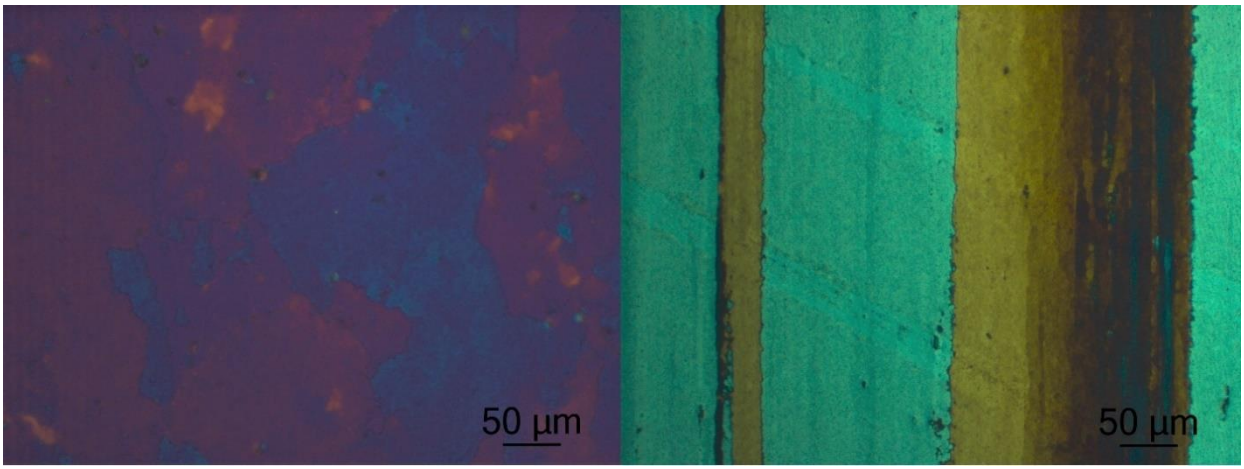

Figure 34 - Image of the microstructure in the extrusion and the pressed transverse direction respectively for a 7.4%CW sample pressed in the transverse direction.

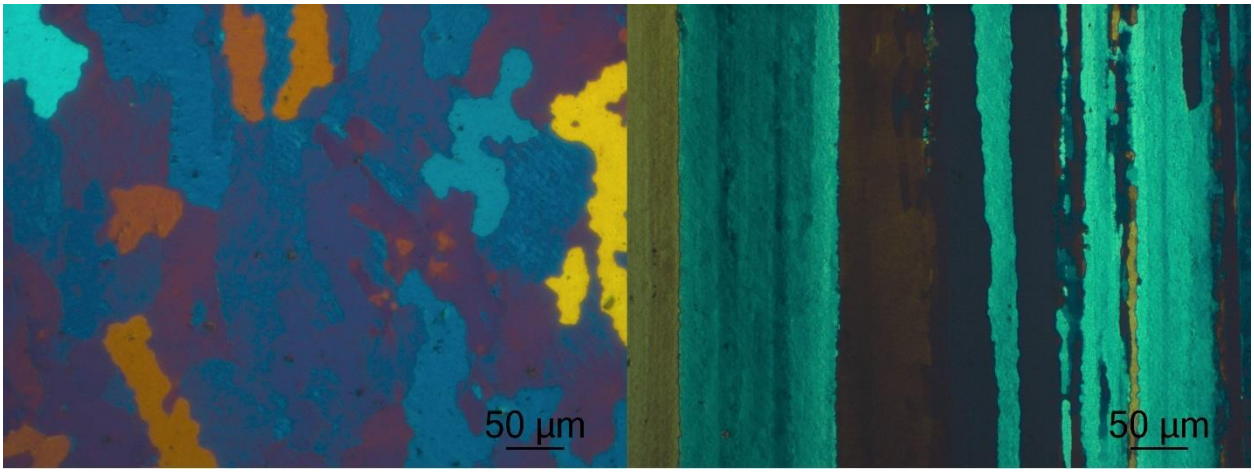

Figure 35 - Image of the microstructure in the extrusion and the pressed transverse direction respectively for an 18.7%CW sample pressed in the transverse direction.

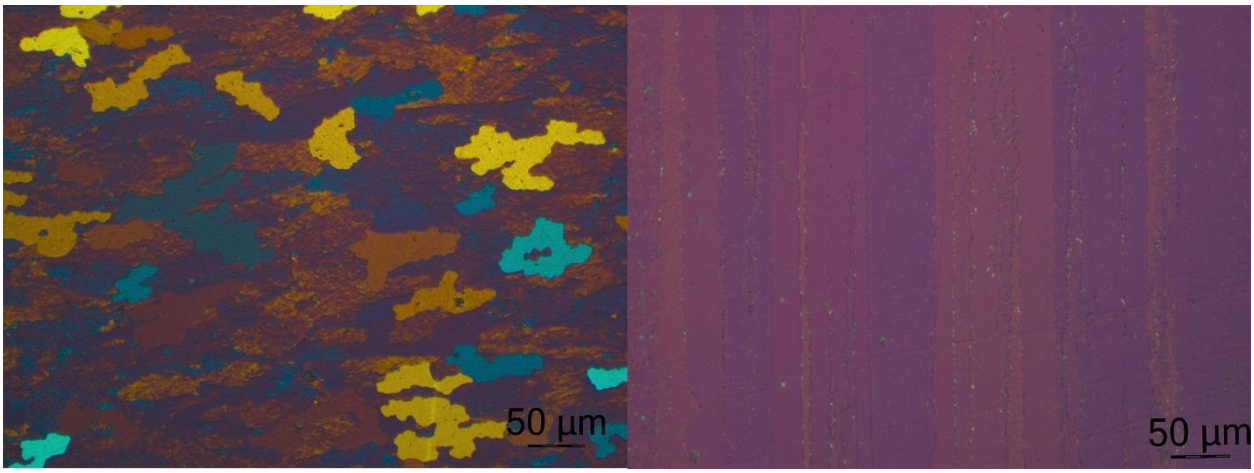

Figure 36 - Image of the microstructure in the extrusion and the pressed transverse direction respectively for a 40.1%CW sample pressed in the transverse direction.

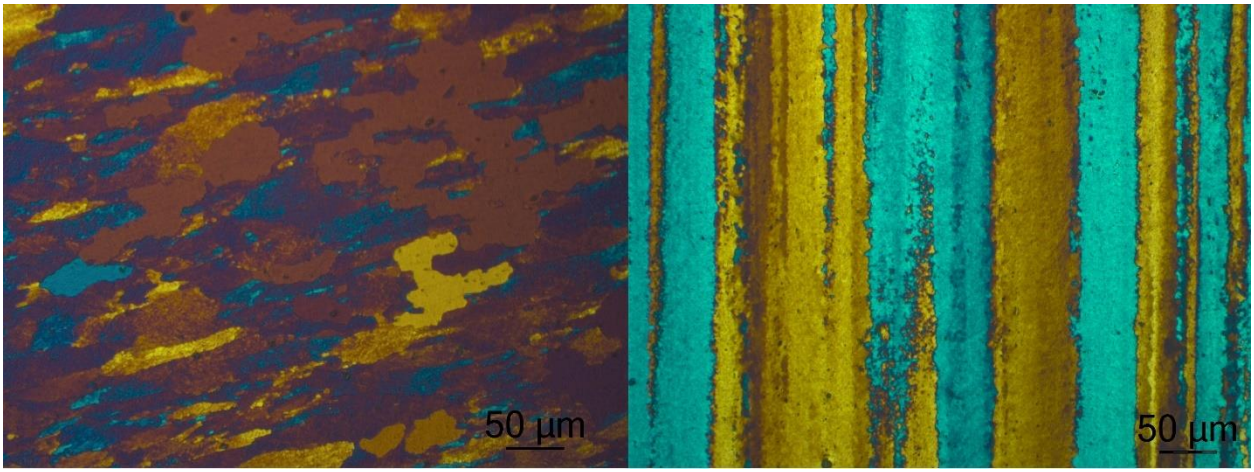

Figure 37 - Image of the microstructure in the extrusion and the pressed transverse direction respectively for a 58.7%CW sample pressed in the transverse direction.

4.3.2 By EBSD Analysis

Table 8 shows the average grain size found using EBSD analysis for cold pressed samples in either the transverse direction or in the extrusion direction. As seen by comparing with section 4.3.1, there is some variation, that is thought to be due to the existence of small sub-grains. For the EBSD analysis, a grain angle tolerance of 5° was used, thusly including sub-grains.

Pressing direction	***%Cold worked***	***Average Grain Size [µm]***	***Standard Deviation [µm]***
Extrusion	0	12.8	15.5
Extrusion	10.1	11.4	12.3
Extrusion	19.9	9.1	15.1
Extrusion	40.5	8.6	16.5
Extrusion	55.5	7.8	7.1
Transverse	0	15.7	30.9
Transverse	7.4	15.4	39.4
Transverse	18.7	15.3	40.5
Transverse	40.1	14.6	32.2
Transverse	58.7	7.6	12.5

Table 8 - Table showing the grain size and respective standard deviation for 0-58.7% cold pressed samples of AA2196 in either the transverse direction or the extrusion direction.

Figure 38 is a plot of the average grain size in the extrusion direction. The grain size decreases with an increase in cold work, with the sharpest decline between 10.1% and 19.9% cold work.

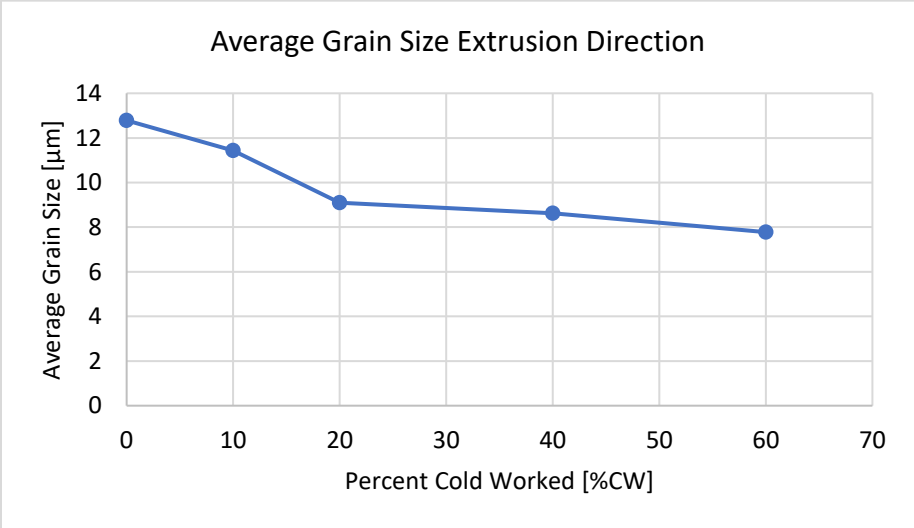

Figure 38 - Average grain size in the extrusion direction for samples cold pressed 0-55.5% in the extrusion direction.

The grain size in the extrusion direction found for a T8511 heat treated sample as delivered from Constellium was 10.7946 µm with a standard deviation of 11.584 µm, seen in Figure 84 in Appendix F. The fraction distribution per intercept length may be seen in Figure 39. The distribution seems to be relatively even, although slightly better in the horizontal direction. Additionally, the grain size is relatively similar for vertical and horizontal lines.

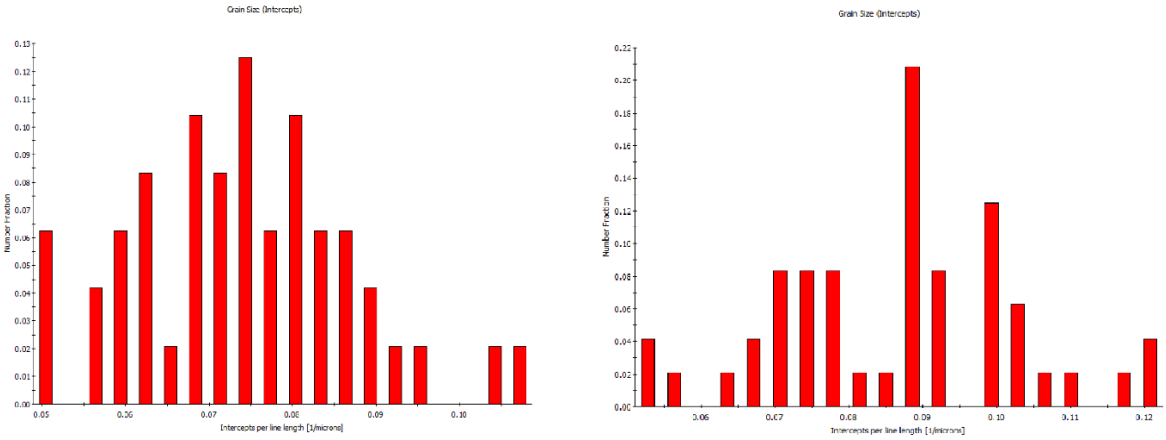

Figure 39 - Fraction distribution per intercept length for T8 treated sample in the extrusion direction as delivered from Constellium. The left figure is with horisontal lines and the right with vertical lines.

Figure 40 shows the average grain size in the pressed transverse direction. The grain size is initially noticeably higher than in the extrusion direction seen above, but after 58.7% CW the grain size is approximately the same in both the transverse and the extrusion direction. There is little change in grain size with respect to cold work until 58.7% cold work is achieved, in which there was a large decrease in grain size.

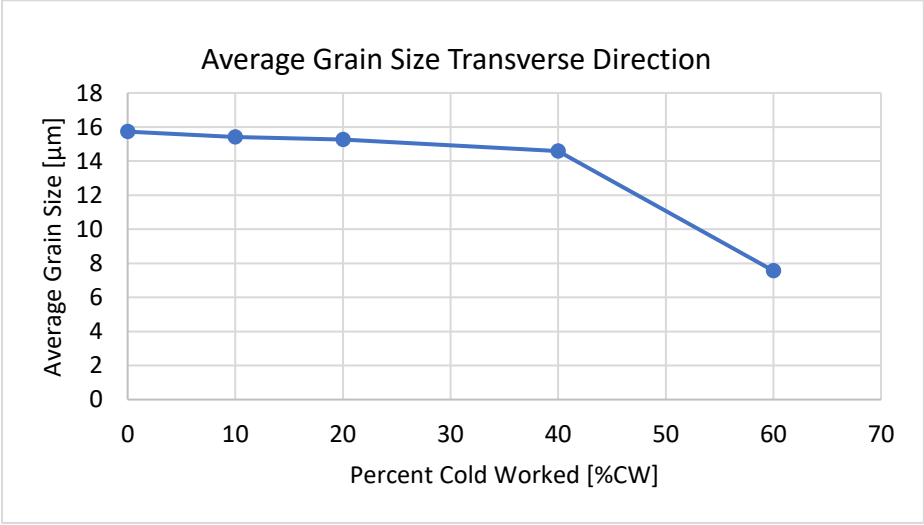

Figure 40 - The average grain size in the pressed transverse direction for samples cold pressed 0-58.7% in the transverse direction

The average grain size in the pressed transverse direction for the T8 tempered material as delivered was 3.09276 µm with a standard deviation of 7.63626 µm, see Figure 83 in Appendix F for the grain distribution. Preheat treatment, the grain size was significantly lower than those obtained in this paper for the transverse direction. Figure 41 gives the fraction distribution per intercept line for the transverse direction as delivered. There was a significant spread in the intercept length for horizontal lines, suggesting the lines were along the elongated grains. Thus, by examining the vertical lines, it is observed that the thickness of the elongated grains is very closely spread.

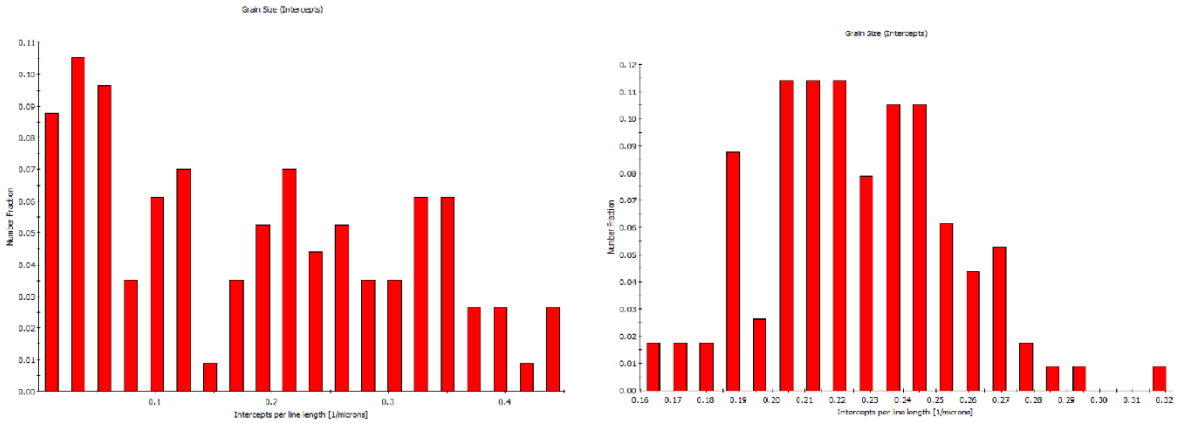

Figure 41 - Fraction distribution per intercept line for a T8 treated sample as delivered from Constellium in the transverse direction. The left plot is for horizontal lines and the right for vertical lines used.

4.4 Anisotropy after Cold Working

Figure 42 shows the (111) and (001) pole figures for AA2196-T8511 samples as delivered from Constellium. Extrusion directions are horizontally, while the transverse directions are out of the plane and vertically. The bands observed indicates anisotropy.

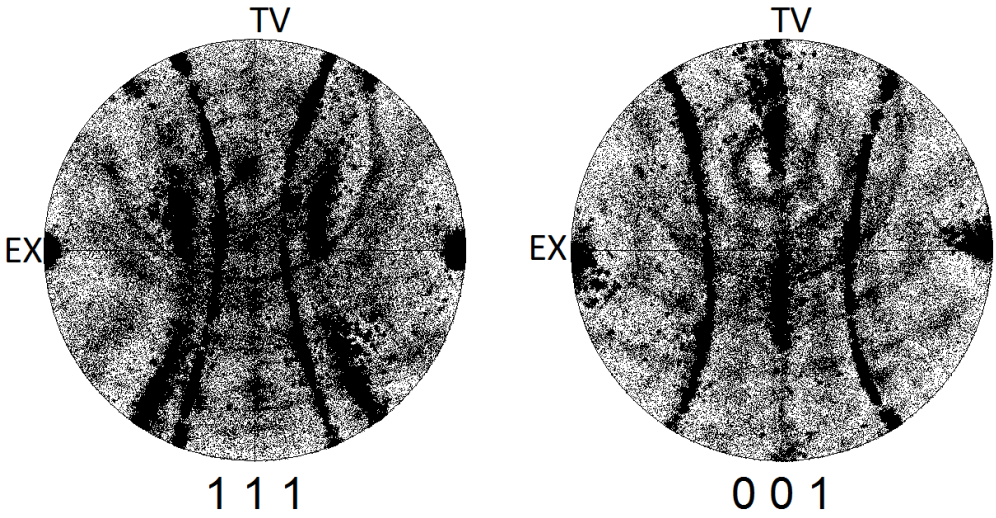

Figure 42 - Pole figure of the initial T8 material seen in the transverse direction.

Figure 43 and Figure 44 shows the (001) and (111) pole figures respectively for AA2196 samples pressed in the extrusion direction ranging from 0-55.5%CW. Extrusion direction is out of the plane, indicated by ex, while the transverse directions are in the directions of the axes. The distinct circles representing anisotropy for Al-Li, as seen in Figure 9, seem to become less prominent with an increased amount of cold work. Worth noting is that the angle of observation is different for the samples pressed in the extrusion direction, thereby a similar texture will look different, i.e. the belts seen in Figure 42 will become circles in Figure 43 and Figure 44.

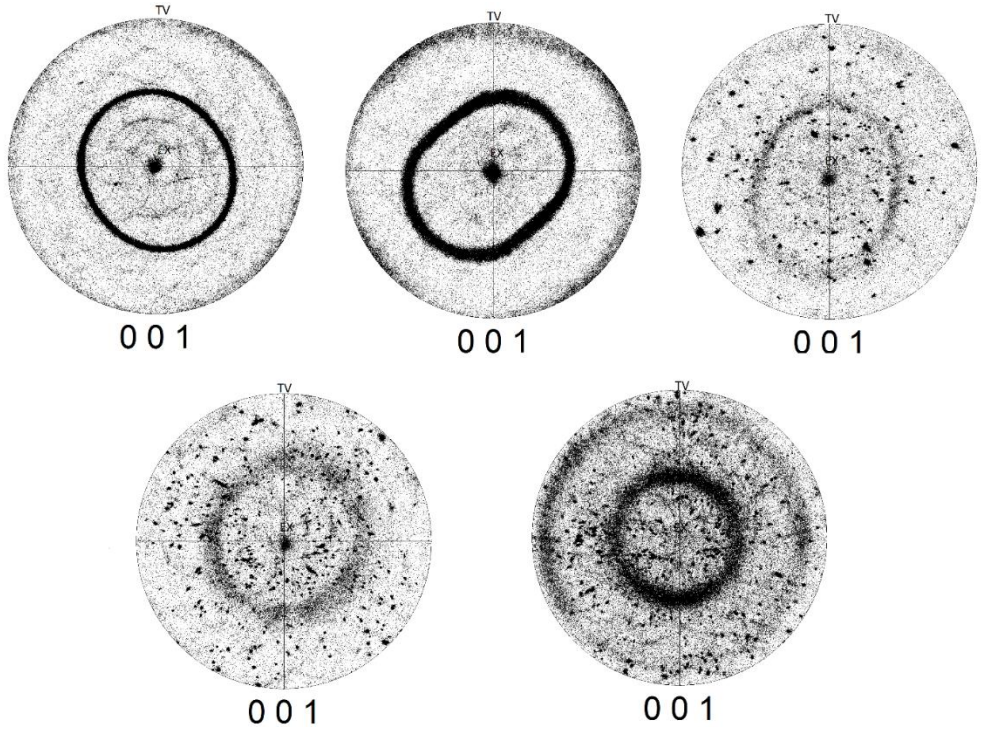

Figure 43 – (100) Pole figures of samples pressed in the extrusion direction. The samples are, from left to right and top to bottom, 0%CW, 10.1%CW, 19.9%CW, 40.5% CW and 55.5%CW. The extrusion direction is out of the plane.

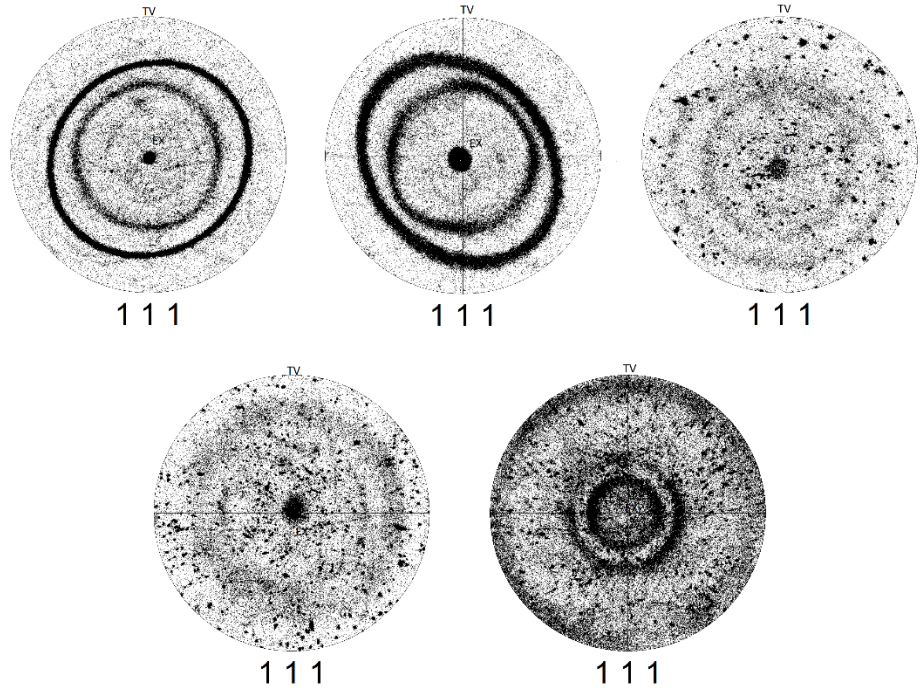

Figure 44 – (111) Pole figures of samples pressed in the extrusion direction. The samples are, from left to right and top to bottom, 0%CW, 10.1%CW, 19.9%CW, 40.5% CW and 55.5%CW. The extrusion direction is out of the plane.

Figure 45 indicated the inverse pole figure of a 40.5%CW AA2196 cold pressed in the extrusion direction. No clear fibrous texture can be seen.

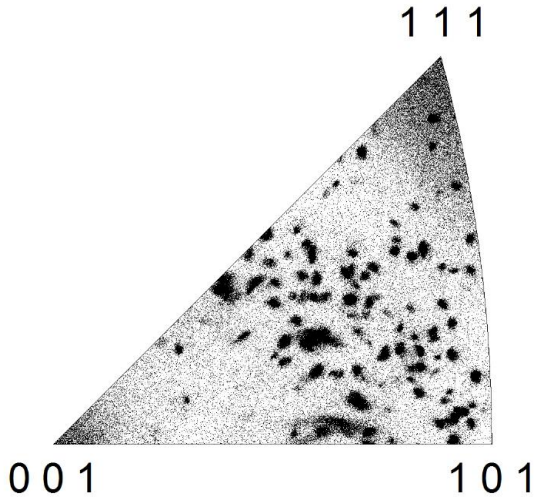

Figure 45 - The inverse pole figure of a 40.5%CW AA2196 sample cold pressed in the extrusion direction.

Figure 46 shows the inverse pole figure for 55.5%CW AA2196 pressed in the transverse direction. There seems to be a strong tendency for points to cluster close to the ⟨110⟩ fiber.

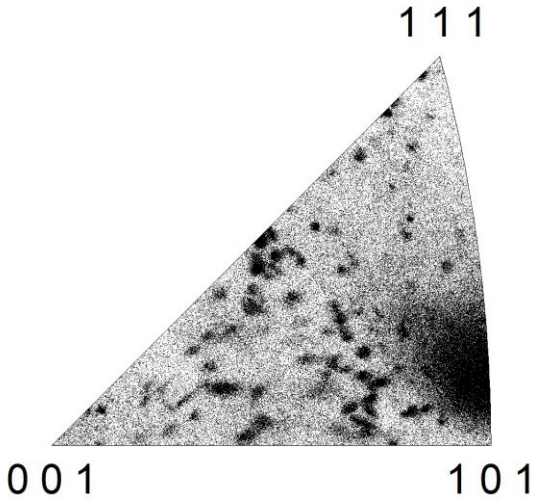

Figure 46 - Inverse pole figure of 55.5%CW AA2196 pressed in the extrusion direction.

Figure 47 and Figure 48 shows the (001) and (111) pole figures respectively for AA2196 samples pressed in the transverse direction ranging from 0-58.7%CW. Extrusion direction, indicated by ex, is horizontally for 0% and 7.4%CW and vertically for 18.7-58.7%CW, while the pressed transverse direction is out of the plane and the second transverse direction is either vertically or horizontally respectively. The distinct circles representing anisotropy for Al-Li, as seen in Figure 9, seem to become less prominent with an increased amount of cold work.

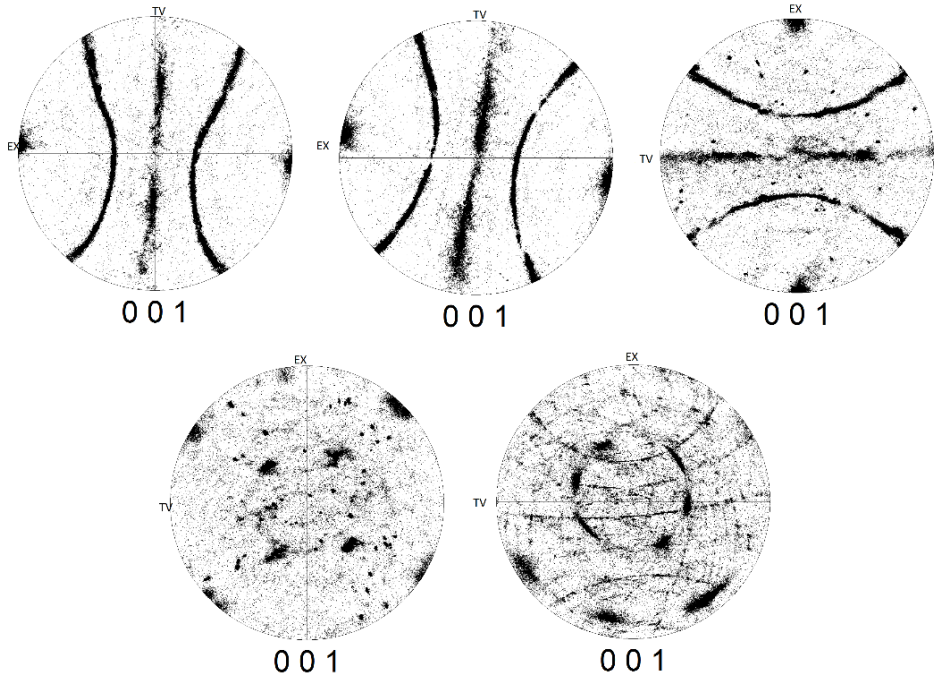

Figure 47 – (001) Pole figures of samples pressed in the transverse direction. The samples are, from left to right and top to bottom, 0%CW, 7.4%CW, 18.7%CW, 40.1% CW and 58.7%CW. The extrusion direction is horizontally for 0% and 7.4% CW, and vertically for 18.7-58.7% CW. The pressed transverse direction is out of the plane.

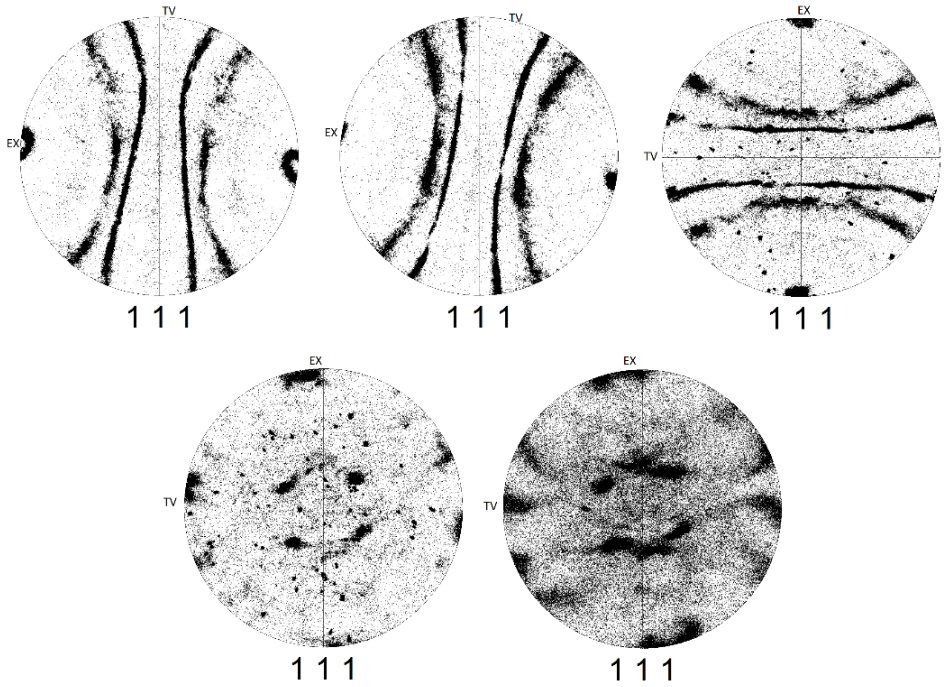

Figure 48 – (111) Pole figures of samples pressed in the transverse direction. The samples are, from left to right and top to bottom, 0%CW, 7.4%CW, 18.7%CW, 40.1% CW and 58.7%CW. The extrusion direction is horizontally for 0% and 7.4% CW, and vertically for 18.7-58.7% CW. The pressed transverse direction is out of the plane.

4.5 Charpy Testing

Cold rolled samples from Table 7 were made into Charpy samples and tested. The fracture energy is given in Table 9. Figure 49 shows the fracture energies plotted against percent cold work. The fracture energies for AA2196 seems to decrease with an increase in cold work and were significantly higher than those measured for AA7090. For AA2196 there seems to be a higher variance in measured energies.

Alloy and sample number	***Nominal % CW***	***% CW per sample***	***Energy to fracture [J]***
2196 - 10	0	0, 0, 0, 0	16.66, 23.59, 16.20, 22.15
2196 - 7/3/4	10	12.0, 12.0, 9.1, 10.3	21.41, 21.91, 13.04, 21.48
2196 - 2	20	19.0, 19.0, 19.0, 19.0	12.53, 13.81, 20.14, 13.02
2196 - 8	40	39.0, 39.0, 39.0, 39.0	9.74, 12.37, 15.62, 10.44
2196 - 9	60	56.3, 56.3, 56.3, 56.3	7.5, 8.39, 9.25, 8.56
7090 - B8	0	0, 0, 0, 0	2.48, 2.50, 2.50, 2.44
7090 - B3	10	9.2, 9.2, 9.2, 9.2	2.54, 2.82, 2.64, 2.66
7090 - B5	20	18.6, 18.6, 18.6, 18.6	2.56, 2.86, 2.74, 2.58
7090 - B6	40	39.1, 39.1, 39.1, 39.1	1.65, 1.69, 1.34, 1.34

Table 9 - Table showing the fracture energy after Charpy testing for cold rolled samples of AA2196 and AA7090.

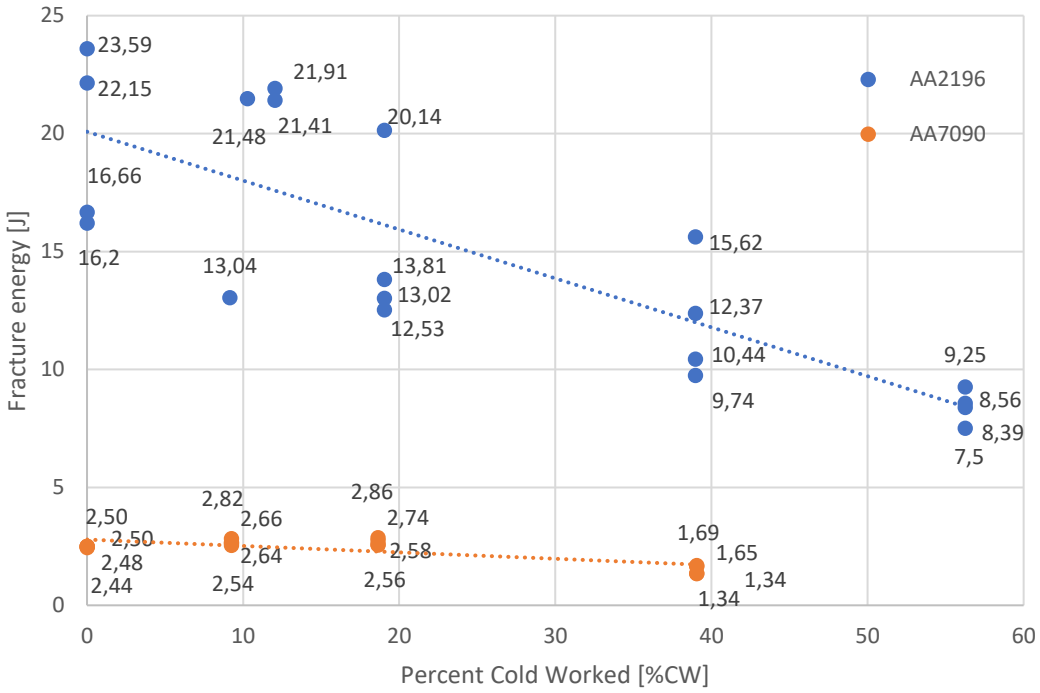

Figure 49 - Plot showing the fracture energies for both AA2196 and AA7090 at various degrees of cold work.

Figure 50 shows the fracture surfaces for 0-56.3%CW AA2196. 0%CW is to the top left of the picture and cold work increases from left to right and top to bottom. As seen in the pictures, there is significant deformation of the Charpy samples, suggesting that some energy has gone into propagating the crack and a more ductile fracture. A similar picture can be seen for AA7090 in Appendix H. AA7090 seem to have experienced a more granular fracture and thus less ductile.

Figure 50 – The fracture surfaces of Charpy samples for 0-56.3%CW AA2196. Cold work is increasing from left to right and top to bottom.

From Table 10 a small hardness increase may be seen between an area close to the surface of the sample and approximately in the middle of the Charpy sample. By examining Figure 51, the microstructure 0.54 ± 0.04 mm into the sample, and Figure 52, the microstructure 2.53 ± 0.15 mm into the sample, a difference in grain size may be observed. Fewer grains were observed on the surface of the sample, while the core of the sample had a much finer grain structure with a larger amount of grains.

Sample and location	***Hardness [HV5]***	***Average [HV5]***
0% CW, 0.54 ± 0.04 mm into the sample	133, 132, 135, 129, 135	132.8
0% CW, 2.53 ± 0.15 mm into the sample	139, 142, 141, 134, 135	138.2

Table 10 - Table showing the hardness in an AA2196 0%CW Charpy sample at the surface and inside the material. Due to a slight curvature of the sample after polishing, there was a variation of approximately 0.15 mm in depth when conducting hardness testing.

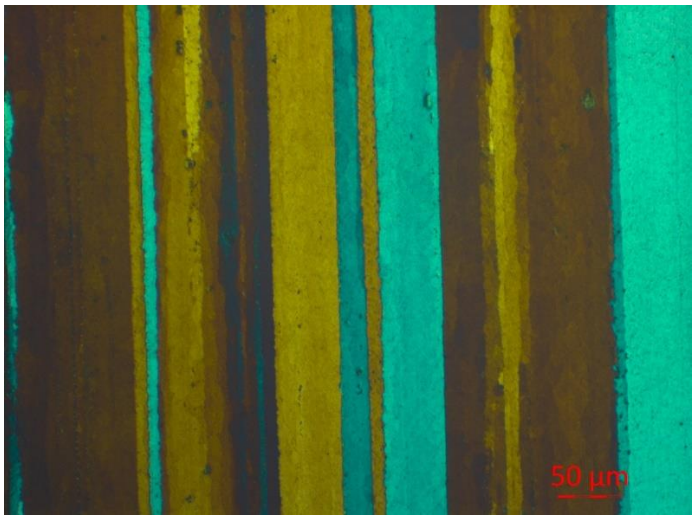

Figure 51 - The grain structure of a 0% CW AA2196 Charpy sample 0.54mm into the surface.

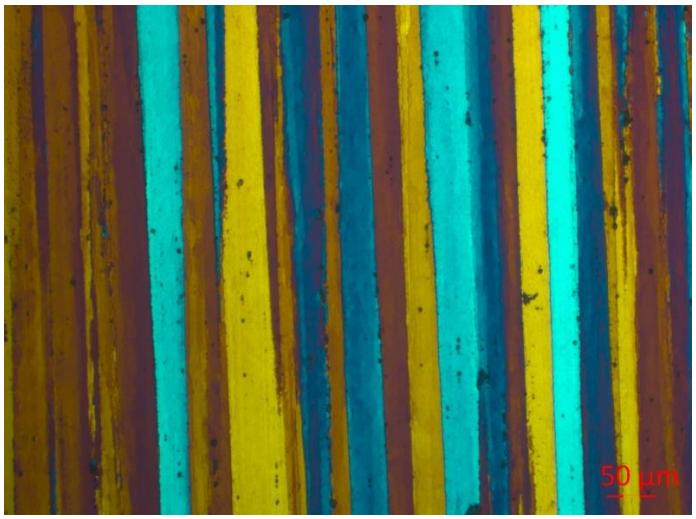

Figure 52 - The grain structure of a 0%CW AA2196 Charpy sample 2.53 mm into the sample.

4.6 Temperature Differences in the Furnaces Utilized

It was found that the temperature experienced by samples in the furnace N11/R did not match the display temperature. Consequently, a test was conducted to find the relative error between the actual temperature experienced compared to the set temperature. Figure 95 indicates the temperature experienced either inside an aluminium test piece or in the air either 0.5 cm above the sample or 2 cm above the sample.

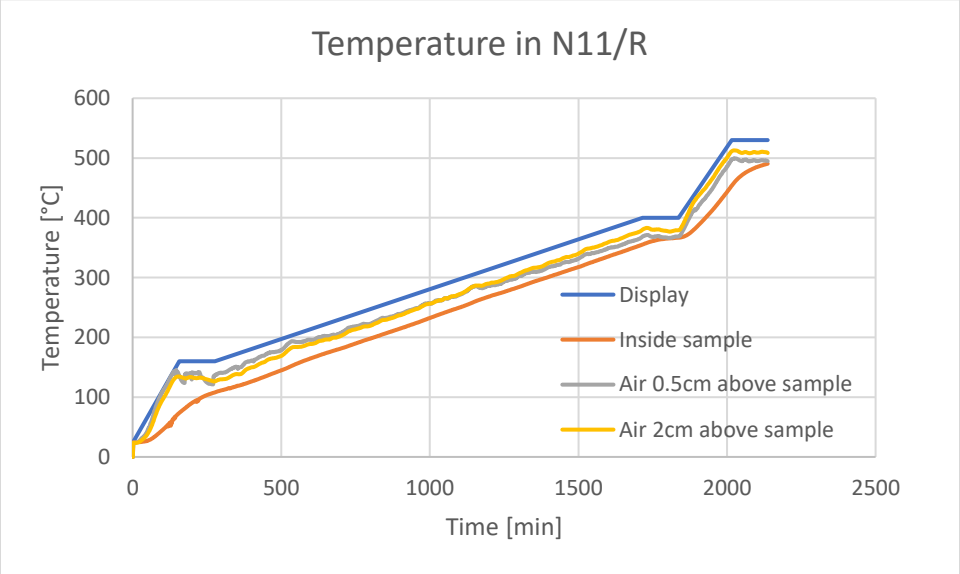

Figure 53 - Time-temperature logging of the temperature within a sample, 5 mm above the sample and 20 mm above the sample for N11/R.

Table 11 gives some of the temperature deviations found in Figure 53. As seen, the temperature deviation is large, thereby damaging the credibility of several heat-treated samples.

Average Temperature during	Annealing [°C]	Solid solution heat treatment [°C]	Precipitation hardening [°C]
Display	400	530	160
5 mm above sample	368.5 ± 3.2	496.3 ± 4.0	131.6 ± 3.2
20 mm above sample	376.6 ± 3.2	509.9 ± 4.1	130.2 ± 3.2

Table 11 - Table showing the average temperature measured 5mm and 20 mm above a sample by thermocouples at various temperatures.

Figure 54 shows the temperature development for the annealing process, both inside an AA2196 sample piece and two separate measurements of the furnace air. Heating time to 400°C was 25 minutes. During gradual cooling to 250°C at a speed of 0.5°C/min, the sample piece seemed to cool relatively close that of the display. As seen, the temperature is

relatively homogenous within the furnace. Figure 55 indicates the cooling process for the test piece when the furnace door was opened and thus cooled by the outside air. After 132 minutes the sample was removed as the temperature was relatively low, 62.5°C. The furnace utilized was N15/HA.

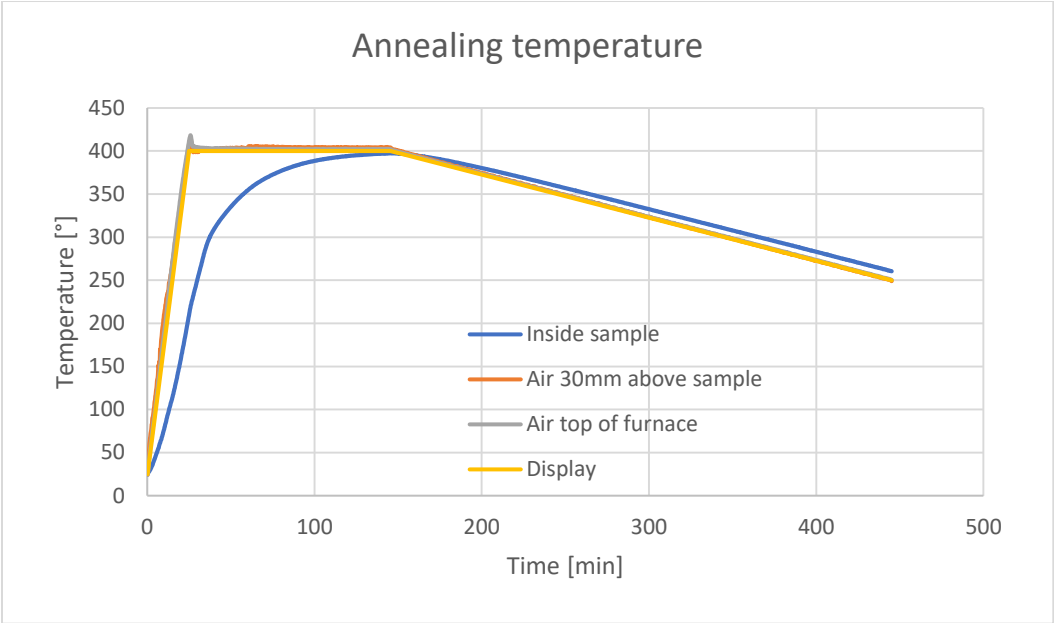

Figure 54 - Plot showing the temperature inside the sample, for the air inside the furnace, both 3cm above the sample and in the top of the sample, and the display temperature for the annealing process conducted. The furnace N15/HA was used.

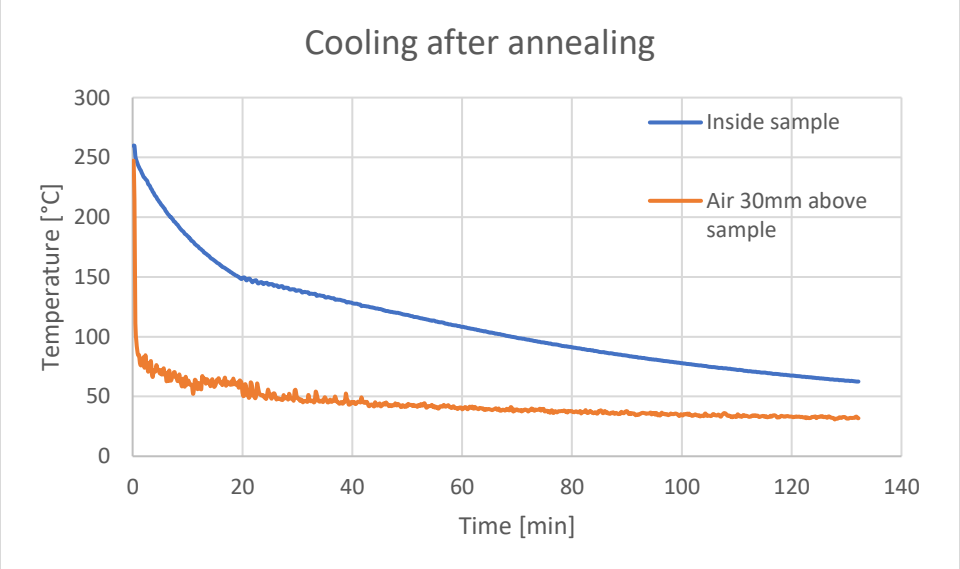

Figure 55 - Figure showing the cooling process for the sample and the air above the sample in a furnace with the door open.

Figure 56 and Figure 57 shows the temperature in the furnace air and inside a test AA2196 piece when conducting heat treatment at similar temperatures to solutionising and precipitation hardening heat treatment. At 530°C, the time holding time was equivalent to the holding time used, 60 minutes, while at 160°C the holding time was 300 minutes. Heating time to the respective temperatures were 23 and 10 minutes. For both Figure 56 and Figure 57 N17/HR was used.

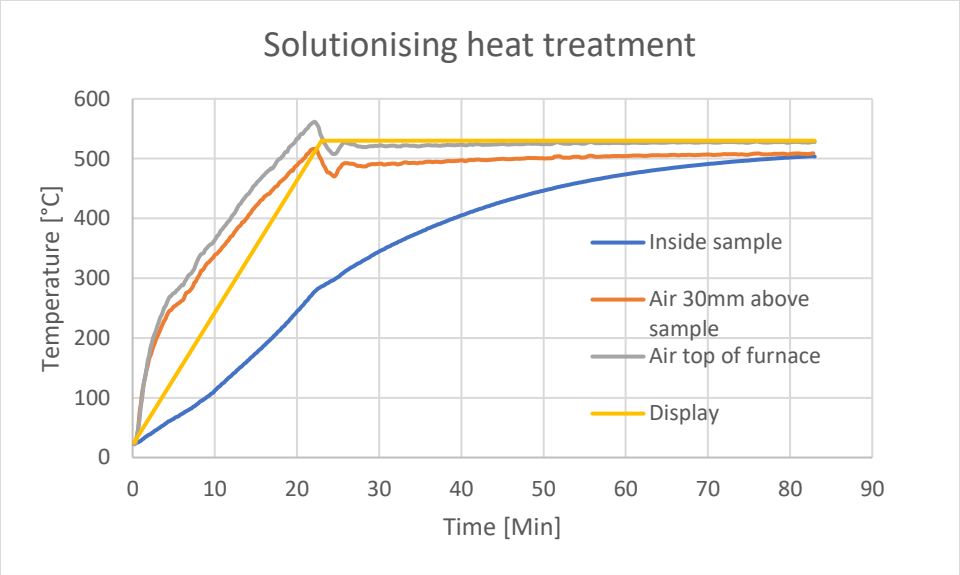

Figure 56 - Plot showing the temperature in the furnace compared to inside the AA2196 sample piece for solutionising heat treatment. The furnace N17/HR was utilised.

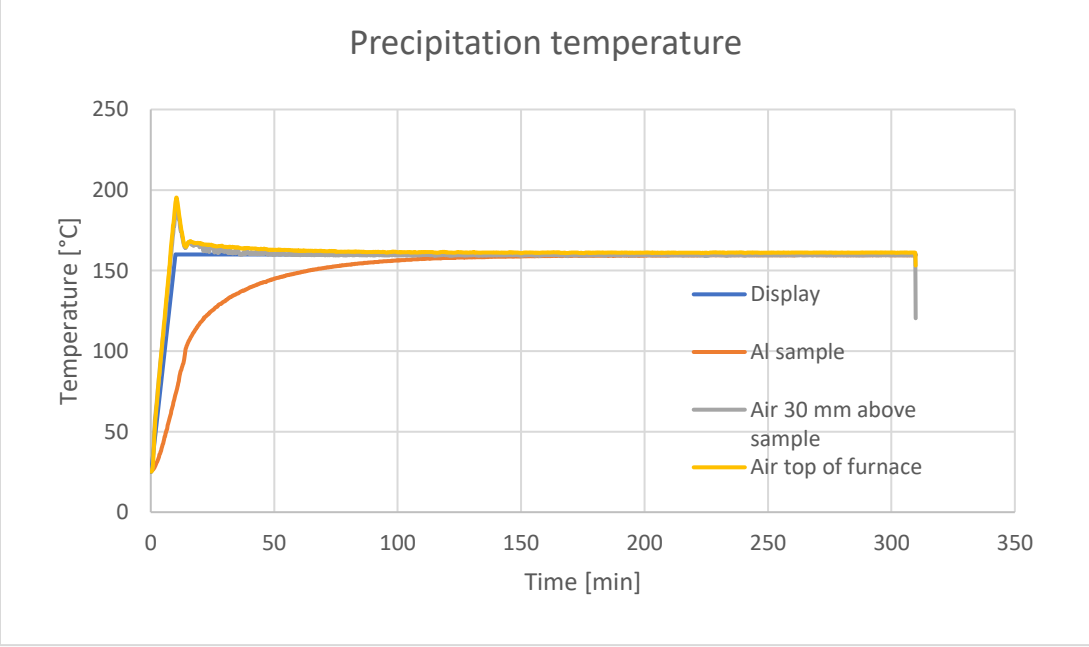

Figure 57 - Plot showing the display temperature, the temperature in an Al sample piece, in the air circa 2 cm above the sample and at the top of the furnace. The furnace N17/HR was used.

From the aforementioned graphs, Figure 54, Figure 56 and Figure 57, an estimate of the true holding times at their respective temperatures may be observed. These values have been summarised in Table 12. As tabulated, the holding time for solid solution heat treatment was significantly lower than the set holding time, with the material using approximately 78 minutes to reach 500°C, thus into the one-phase area seen in Figure 2.

Heat treatment	***Desired Temperature [°C]***	***Holding time set [min]***	***Heating time to max temperature [min]***	***Temperature achieved [°C]***	***Holding time at desired temperature [min]***
Annealing	400 ± 5	120	124	397.3 ± 3.2	21
Solutionising	530 (above 500)	60	78 min to 500°C	504.1 ± 4.0	5 min above 500°C
Precipitation hardening	160 ± 1	300	156	159.5 ± 3.2	154

Table 12 - Table showing the holding time and heating time to the respective temperatures for annealing, solutionising treatment and precipitation hardening. For precipitation hardening, a shorter time was conducted than during actual treatment.

Table 13 gives a summary of the assumed holding times during various heat treatments undergone and the actual holding time at the various temperatures.

Heat treatment	***Desired Temperature [°C]***	***Assumed holding time [min]***	***Actual holding time [min]***
Annealing	400 ± 5	120	21
Solutionising	530 (above 500)	60	0 (5 above 500°C)
Precipitation hardening	160 ± 1	720	564

Table 13 - Actual heat treatment undergone for heat treated AA2196.

4.7 Precipitation Hardening Curves for AA2196 and AA7090

AA2196 was precipitation hardened at 150°C and 180°C, seen in Table 2, which were combined with previous precipitation curves, giving Figure 58. Additionally, data for an aging curve at 160°C from previous work were used (Kyllingstad, 2018). The hardness measurements for this curve may be seen in Table 20 in Appendix B. A longer aging time was used for AA7090 to achieve a T6 temper which, according to internal documents at NAMMO Raufoss, occurs after 24 hours.

The hardness of AA2196 seemed to increase with respect to both time and temperature, while the hardness of AA7090 is relatively stable throughout the time interval. According to Figure 49, AA7090 has a distinctly higher hardness than AA2196.

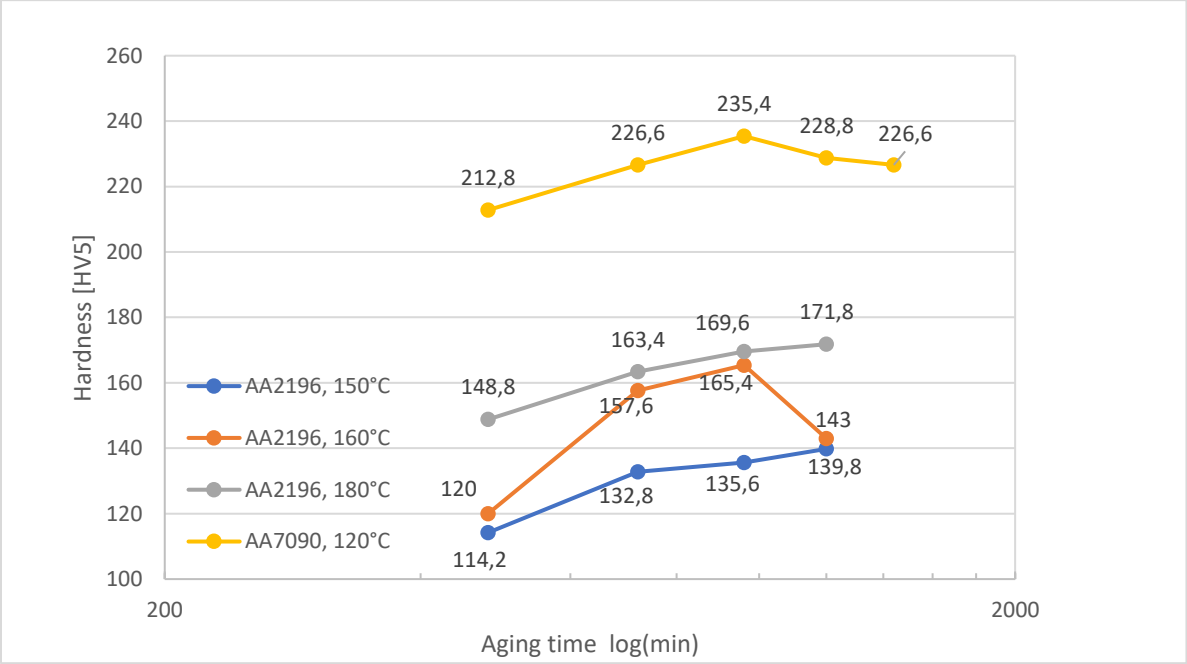

Figure 58 - Precipitation hardening curves at various temperatures for AA2196 and at 120°C for AA7090. Aging times were 8-20 hours for AA2196 and 8-24 hours for 7090. Graph for aged AA2196 at 160°C taken from previous work (Kyllingstad, 2018).

4.8 Tensile Testing of AA2196 and AA7090

AA2196 was tensile tested to provide a baseline strength and elongation prior to any heat treatment, as seen in Figure 59. Testing indicated that AA2196 exhibited a high yield strength, approximately 656 MPa compared to 490MPa in the datasheet and displayed a similar elongation 5.7% to 5% (Uféras, 2017b). Additionally, the specific strength of AA2196 was high.

Alloy	***Engineering Yield Strength [MPa]***	***Engineering Tensile Strength [MPa]***	***%Elongation***	***Specific Strength [kPa m³/kg]***
AA2196	654, 658, 656, 656	660, 665, 664, 662	5.36, 6.45, 5.56, 5.36	251.0, 252.9, 252.5, 251.7

Table 14 - Table showing the strength, %elongation and specific strength obtained for four tensile test rods of AA2196-T8511.

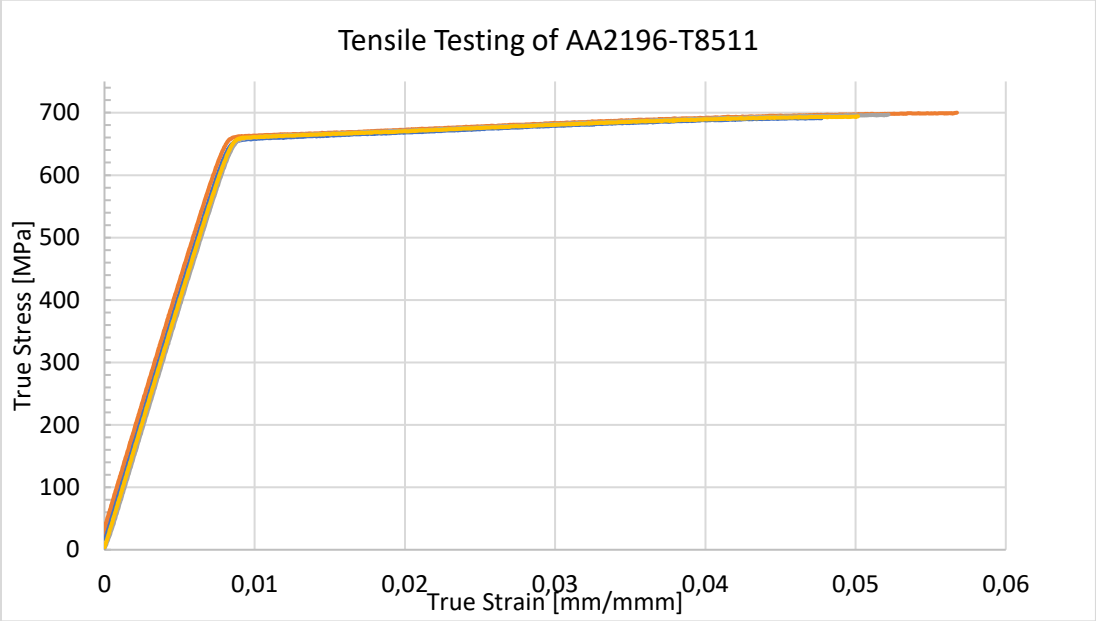

Figure 59 – True stress-strain curve for AA2196 as delivered in a T8511 state.

It was experienced that the stress-strain curve for the smaller tensile testing rods exhibited significant noise in the testing, resulting in the slightly wobbly curves seen below for 19.0%, 39.0% and 56.3%CW for AA2196 and 9.2%, 18.6% and 39.1%CW for AA7090. These wobbly curves are thought to be the results of the load, 2-3 kN, required for the smaller tensile testing rods to be in the lower area for the tensile testing machine which has a range of 0-100kN.

Figure 60-Figure 63 shows the true stress-strain curves for 0-39.1%CW for AA7090. The yield and tensile strength were distinctly lower and %elongation was significantly higher for 0%CW AA7090 than for 9.2-39.1%CW AA7090. 0%CW were heat treated before the discovery that N11/R were not calibrated and thus the material may have been aged at a lower temperature. With increased cold work there were registered an increase in elongation and a decrease in both yield and tensile strength for AA7090.

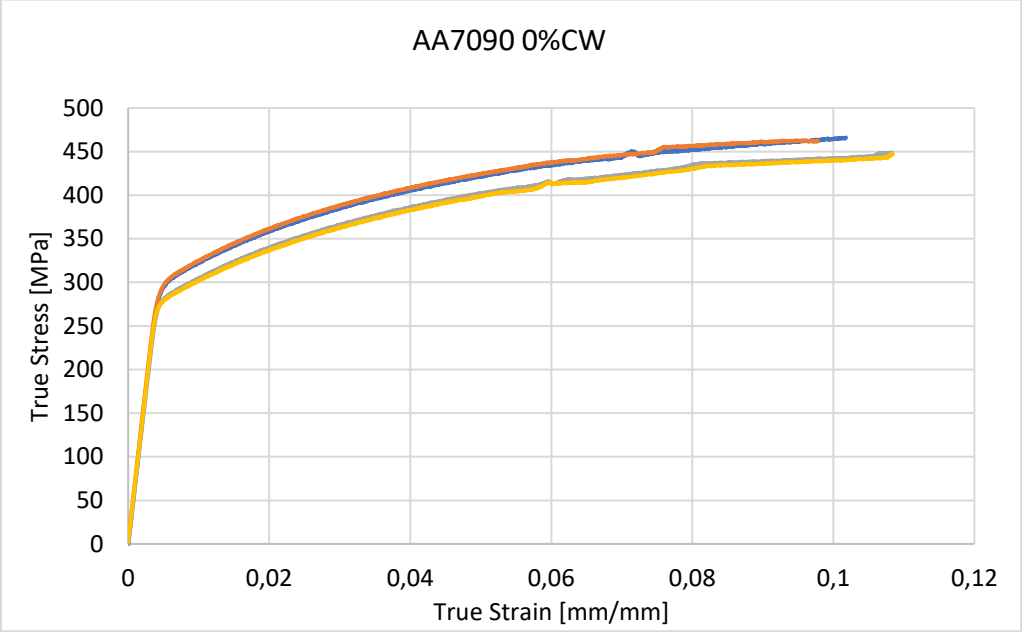

Figure 60 – True Stress-strain curve for 0%CW AA7090.

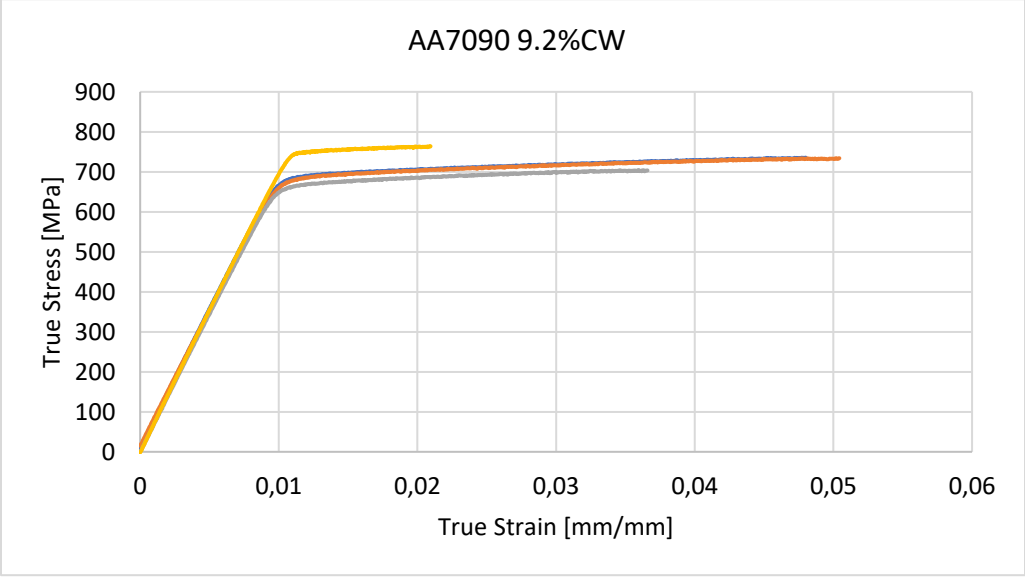

Figure 61 – True stress-strain curve for 9.2%CW AA7090.

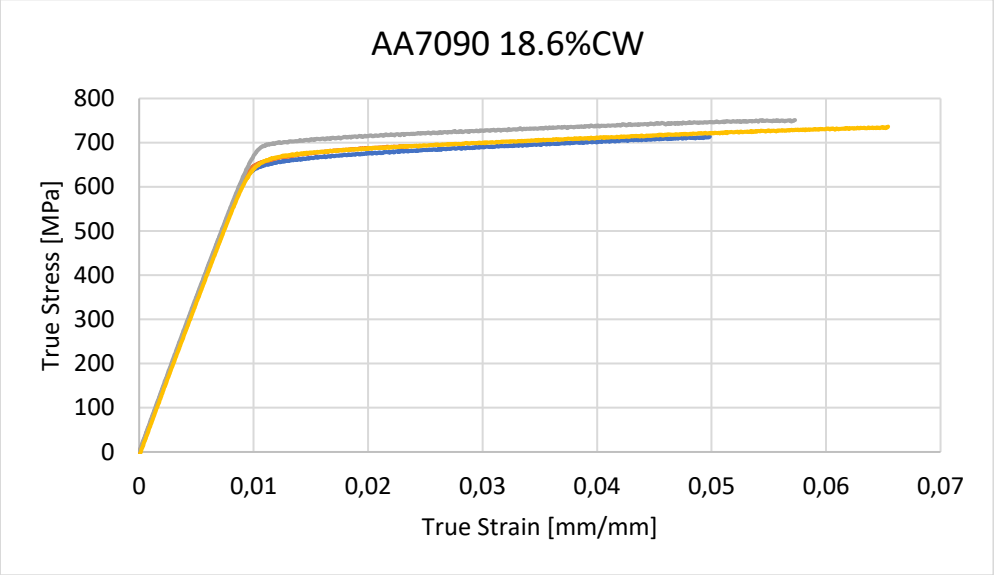

Figure 62 - True stress-strain curve for 18.6%CW AA7090.

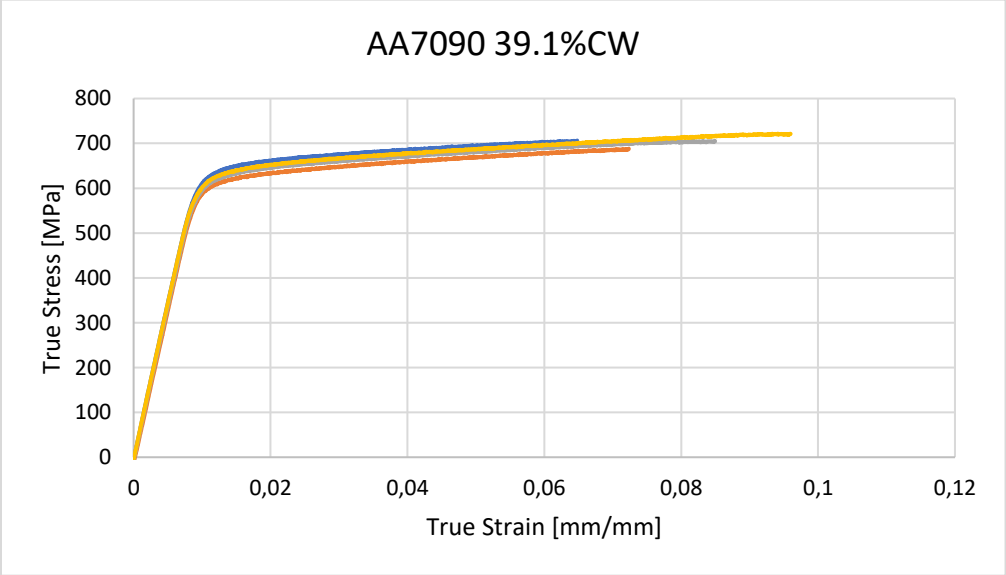

Figure 63 - True stress-strain curve for 39.1%CW AA7090.

Figure 64-Figure 67 are the true stress-strain curves for AA2196 cold worked either approximately 10%, 19.0%, 39.0% or 56.3% respectively. From the stress-strain curves, there may be observed a trend in which an increase in cold work results in an increase in ductility, indicated by %elongation, at the cost of yield and tensile strength.

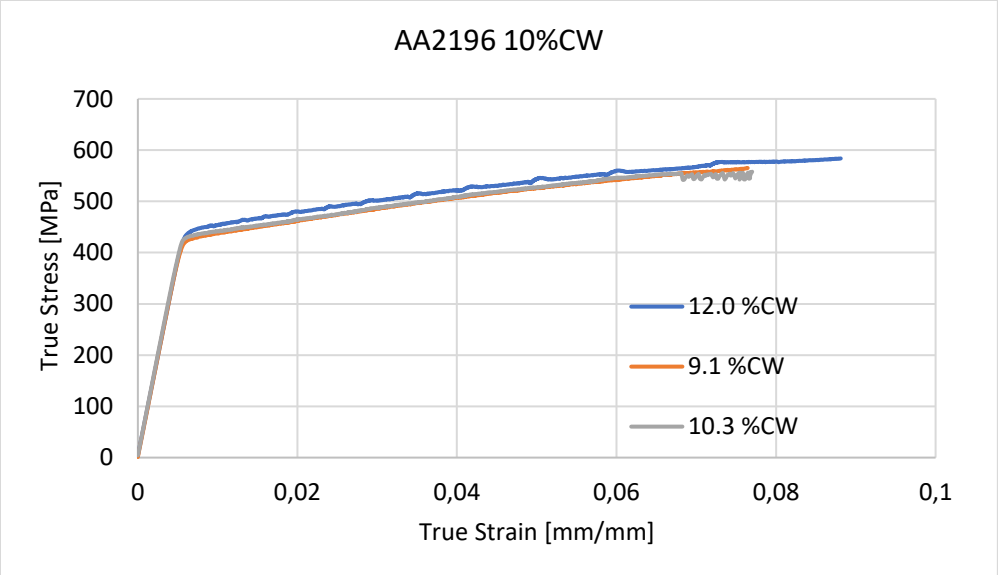

Figure 64 – True stress-strain curve for 12.0, 9.1 and 10.3%CW AA2196 respectively.

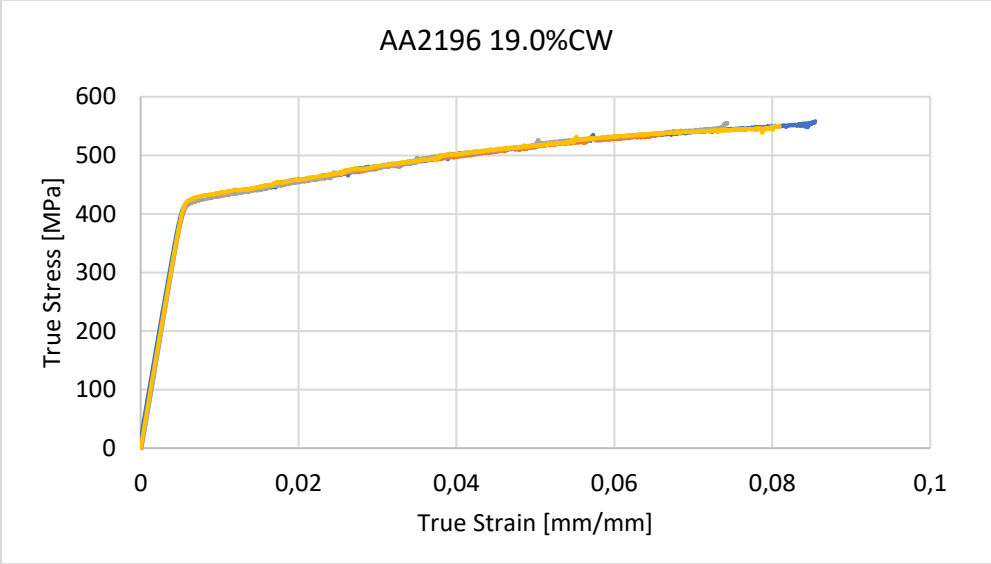

Figure 65 – True stress-strain curve for 19.0%CW AA2196.

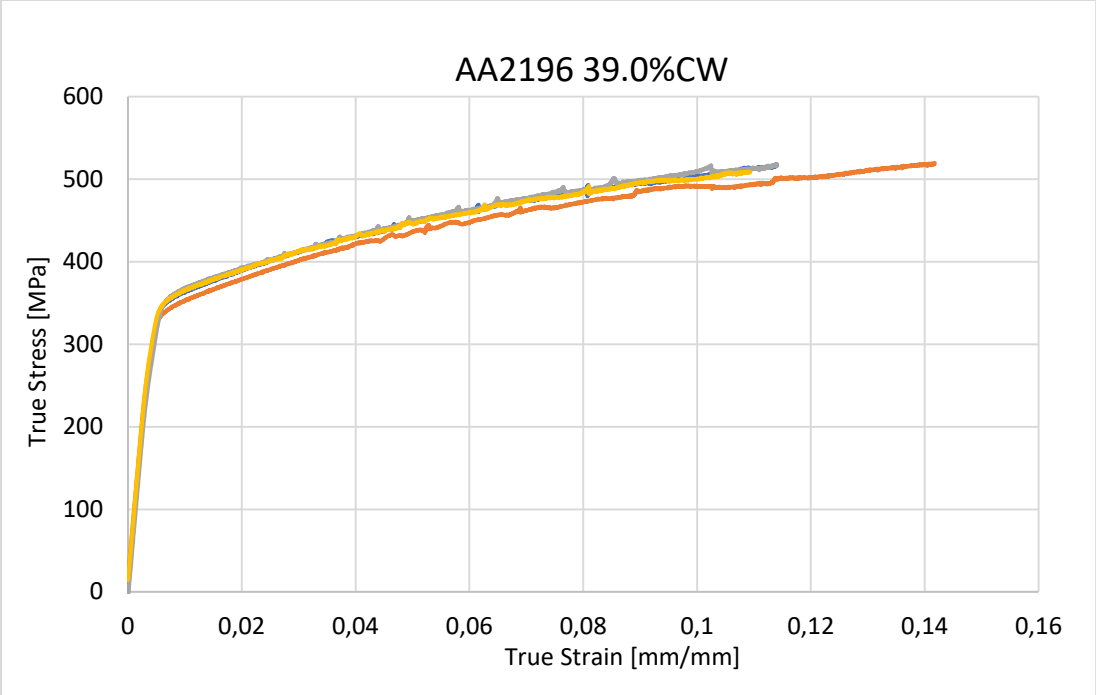

Figure 66 – True stress-strain curve for 39.0%CW AA2196.

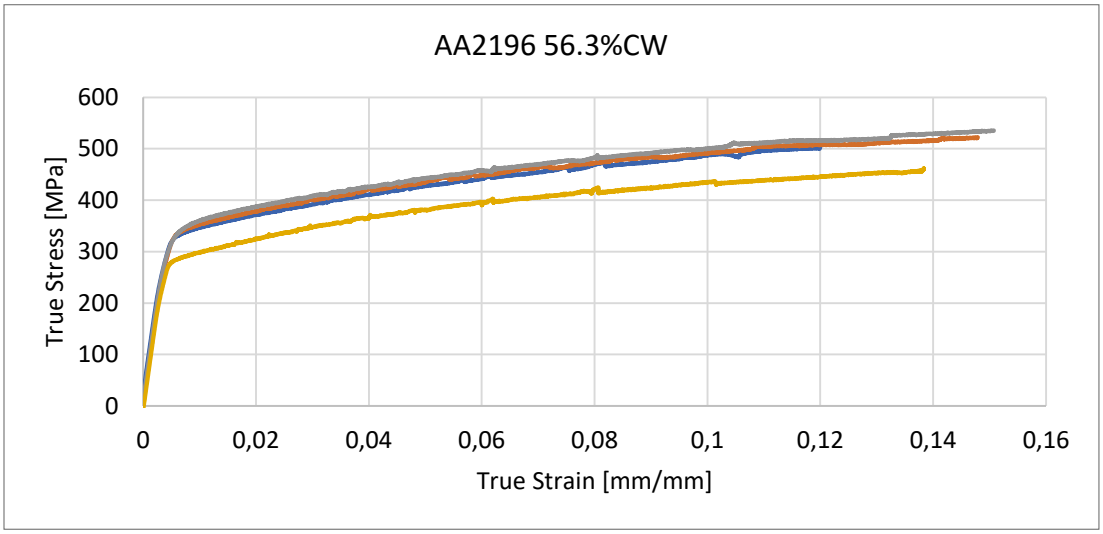

Figure 67 – True stress-strain curve for 56.3%CW AA2196.

Table 22, Table 23 and Table 24 in Appendix D are tabulated values given from Figure 60-Figure 67, while Table 15, Table 16 and Table 17 give the average values. Strain hardening and tensile toughness have been found using engineering stress and strain. For approximately 10%CW of AA2196, the specific values are given and not the average one, as these had slight variations in percent cold worked. Generally, AA2196 has a higher ductility

and a lower strength than that of AA7090. The densities used for AA2196 and AA7090 were 2.63 g/cm^3 and 2.83 g/cm^3 respectively.

Alloy	***% Cold Worked***	***Average Engineering Yield Strength [MPa], $R_{p0.2}$***	***Average Engineering Tensile Strength [MPa], R_m***	***Average %Elongation***
2196	12.0, 9.1, 10.3	445, 428, 432	536, 523, 517	8.59, 7.27, 7.67
2196	19.2	423	510	7.43
2196	39.0	347	457	12.68
2196	56.3	321	440	15.49
7090	0	296	412	10.81
7090	9.2	691	707	3.37
7090	18.6	663	689	4.67
7090	39.1	609	653	9.03

Table 15 - The average values for yield strength, tensile strength and %elongation of AA2196 and AA7090 at various degrees of cold work.

Table 16 shows the calculated specific strength for each tensile test rod for AA2196 and AA7090. The densities used for AA2196 and AA7090 were 2.63 g/cm^3 and 2.83 g/cm^3 respectively.

Alloy	***% Cold Worked***	***Average Specific Yield Strength [kPa m^3/kg]***
2196	12.0, 9.1, 10.3	203.8, 198.9, 196.6
2196	19.2	193.9
2196	39.0	173.9
2196	56.3	167.2
7090	0	145.4
7090	9.2	249.5
7090	18.6	243.3
7090	39.1	230.6

Table 16 - The average specific strength at various degrees of cold work for AA2196 and AA7090.

From Table 17 the tensile toughness is observed to increase with an increase in cold work prior to solid solution treatment. Additionally, both strain hardening and %RA increased with an increase in cold work. Tabulated values for 0%CW AA7090 indicate a much more ductile and less strong material that the values for 9.2-39.1%CW for AA7090.

Alloy	% Cold Worked	Average Strain Hardening [MPa]	Average Tensile Toughness [MJ/m³]	Average %Reduction in Area, %RA
2196	12.0, 9.1, 10.3	91, 95, 85	39.02, 44.98, 36.96	10.33, 14.65, 8.12
2196	19.2	87	37.06	11.65
2196	39.0	111	55.19	23.90
2196	56.3	119	64.65	28.17
7090	0	116	42.44	15.05
7090	9.2	16	26.63	14.75
7090	18.6	26	34.90	13.34
7090	39.1	44	60.50	24.71

Table 17 - The average strain hardening, tensile toughness and %reduction in area at various degrees of cold work for AA2196 and AA7090.

4.9 Influence of Cold Work on Ductility and Strength

From Figure 68 and Figure 69 there seems to be a tendency for cold work prior to solid solution heat treatment to give an increase in elongation and a decrease in tensile strength. The data used in these figures are from Table 15. No trendline for Figure 69 has been included, due to the outlier values found at 0%CW.

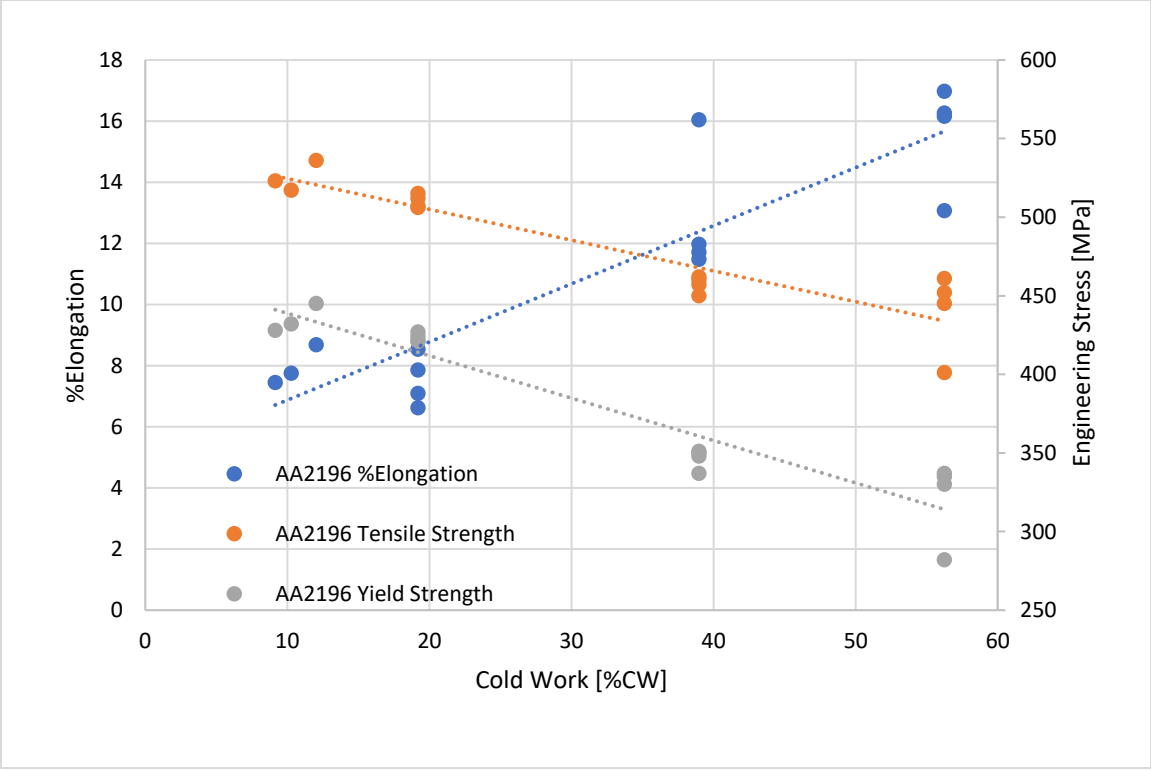

Figure 68 - Plot showing the influence of cold work prior to solutionising heat treatment on ductility and strength in AA2196.

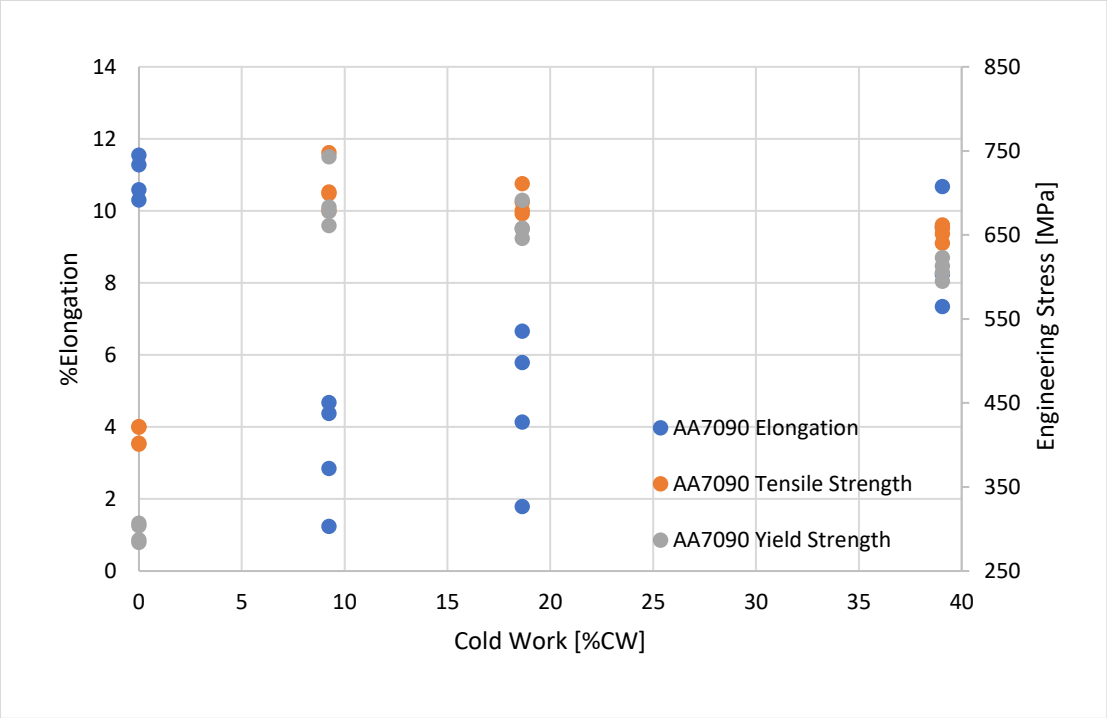

Figure 69 - Plot showing the influence of cold work prior to solutionising on ductility and strength in AA7090.

By comparing and plotting the values in Table 22, Figure 70 was obtained. The tensile strength of AA7090 was noticeably higher than those of AA2196, approximately 150-200 MPa higher than the highest obtained for AA2196, but at the cost of ductility.

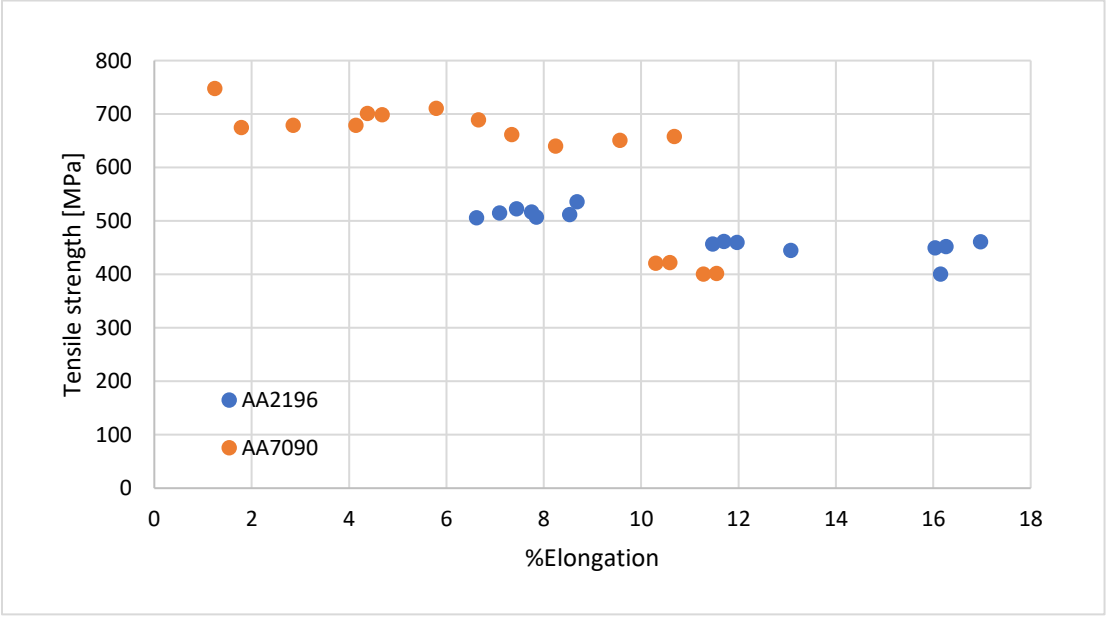

Figure 70 - Plot of the engineering tensile strength and %elongation for AA2196 and AA7090.

Figure 71 shows a trend in which increased cold work prior to solutionising heat treatment results in an increased ductility, supporting a similar trend found when using %elongation. The variation within a respective group is large, as the measurement method used was inaccurate.

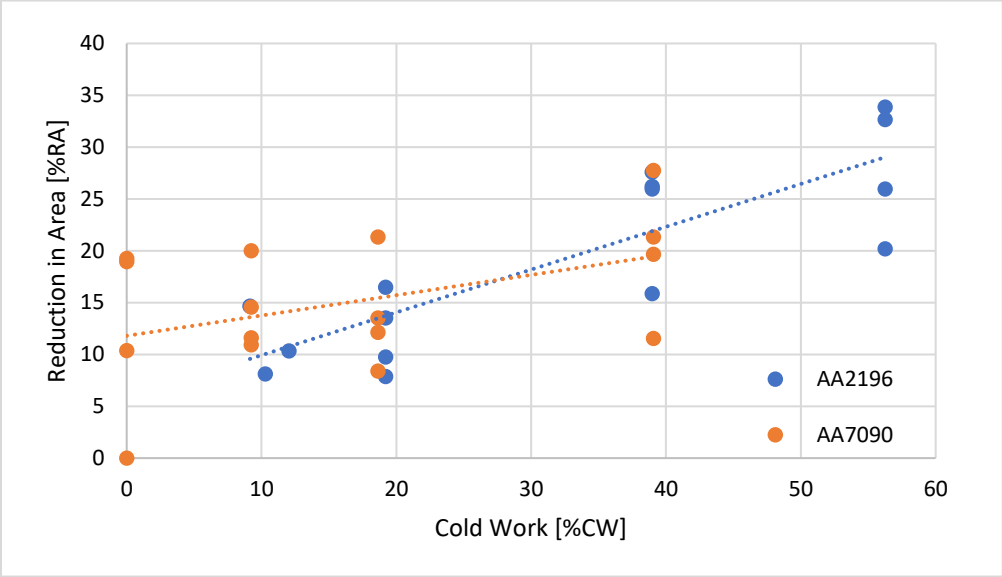

Figure 71 - Plot showing the reduction in area with respect to cold work for AA2196 and AA7090.

In Figure 72, the specific strength has been plotted against percent cold work. AA7090 exhibits a larger specific strength than AA2196 and the specific strength decreases with the amount of cold work. No trendline has been included for AA7090, as there was first a sharp increase and then a slow decline with cold work.

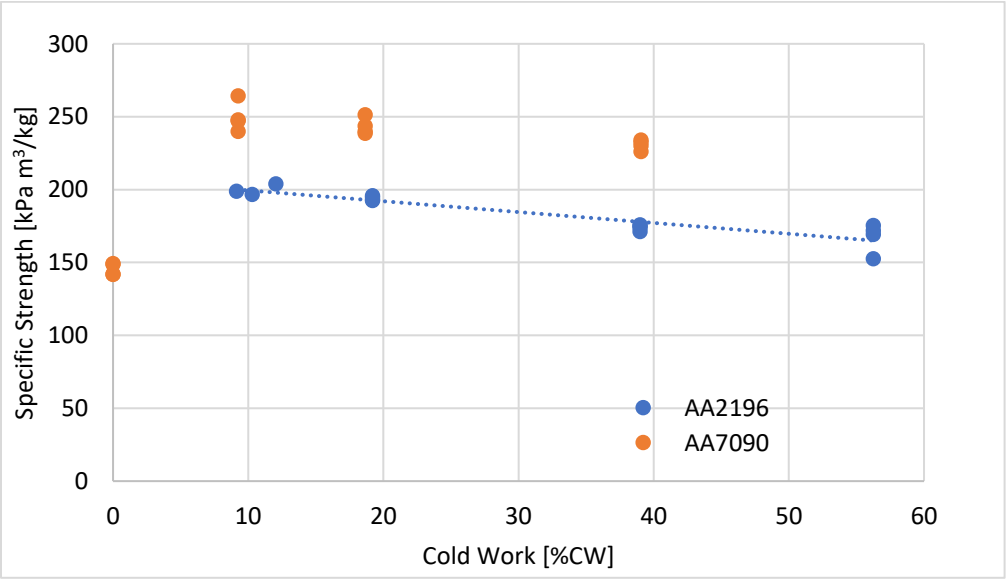

Figure 72 - Specific strength for AA2196 and AA7090 plotted against cold work.

From Figure 73 it can be observed that AA2196 and AA7090 have comparable tensile toughness due to the high ductility of AA2196 and the high strength of AA7090. Toughness generally increases with an increase in cold work.

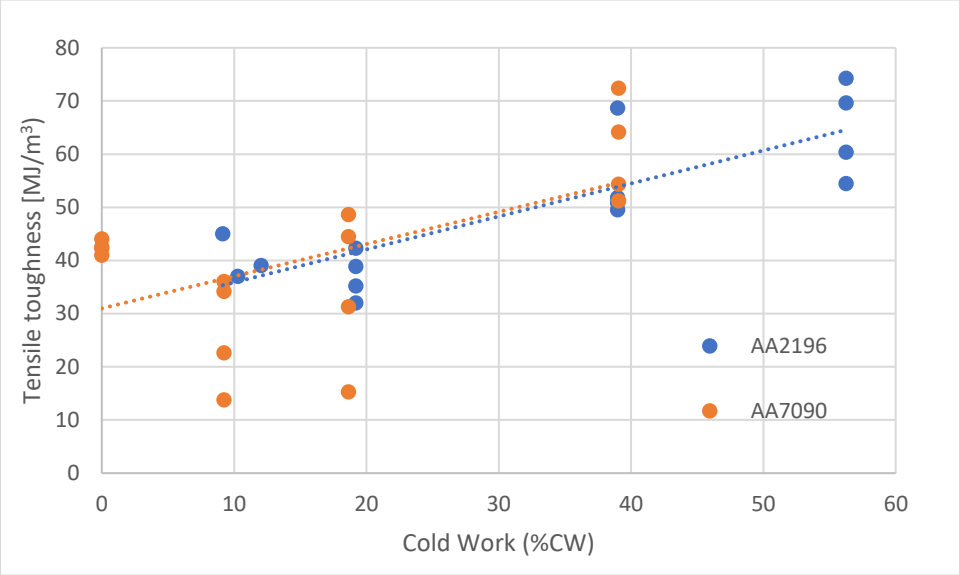

Figure 73 - Plot showing the correlation between cold work and tensile toughness for AA2196 and AA7090.

5. Discussion

In this master's thesis, a third-generation Al-Li alloy has been investigated to determine the suitability of AA2196 in propulsion systems for aerospace applications. A heat treatment process including an annealing step, storage time, a solutionising heat treatment step and an aging step have been used to achieve precipitation hardening. The strength and ductility of AA2196 cold worked from 0-56.3% have been investigated using tensile testing and Charpy testing, and the anisotropy and grain size have been investigated using LOM and EBSD analysis. Additionally, the temperature within an alloy sample has been investigated to determine the deviation between the set temperature and the temperature experienced within the alloy. Furthermore, the strength and ductility of AA2196 have been compared with a 7xxx-series competitor, AA7090, in order to find a baseline.

Tensile testing showed that an increase in cold work resulted in a decrease in yield and tensile strength and an increase in ductility, expressed through %elongation, for both AA2196 and AA7009. The increase in ductility is supported by the fact that %reduction in area showed a similar trend to that of %elongation, but due to the highly uncertain method used in order to determine the resulting area after tensile testing, these values should be viewed with some scepticism and only used as an indication. Although there was a decrease in strength and an increase in ductility, the measured tensile toughness of said materials were found to increase with cold work. This corresponds well with the average grain size seen in Figure 38 and Figure 40, as according to Humphreys and Hatherly (2004) a decreased grain size increases toughness. However, this assumes the nucleation of sub-grains and subsequent grain growth of the sub-grains.

AA2196 exhibited a higher %EL than AA7090, which may have been due to the precipitation structure. 7xxx aluminium alloys are mainly strengthened by the T-phase ($MgZn_2$) and M'-phase ($Al_2Mg_3Zn_3$) particles (Bjerkestrand, 2018), while AA2196 are mainly strengthened by T_1 and θ', although several others, such as δ', contribute. The precipitation structure in AA2196, mayhap due to a large number of strengthening particles, seems to be able to spread the strain hardening throughout a large part of the sample, while AA7090 experiences more local strain hardening, resulting in a lower elongation due to earlier necking. The lower strain hardening may be due to the precipitates in AA7090 being cut by dislocations, while the precipitates in AA2196 require such a high stress to cut that it is beneficial to move around the precipitates instead. Consequently, a higher dislocation density can be sustained for AA2196. However, when comparing the %RA for the two alloys, the initial %reduction in area was larger for 9.2%CW AA7090 than for approximately 10%CW AA2196, suggesting that the ductility difference between AA2196 and AA7090 may not be as large as suggested by %EL. Is should be noted that there was substantial uncertainty when measuring %RA, as this was done using a sliding gauge.

The initial tensile testing of AA2196 indicated a yield and tensile strength ranging from 654 to 658 MPa and from 660 to 665 MPa respectively, while the elongation was in the range of 5.36-6.45 %. This is significantly higher than the minimum strength given in the datasheet for AA2196 of 490MPa and 538 MPa (Uféras, 2017b). The material properties found during tensile testing were quite close to those given for this specific alloy, seen in Appendix A, although the %elongation was significantly lower at 5.7% to 8.5%. This may be due to local variations in the tensile test rods, which, if Constellium has used larger tensile testing rods,

may have been avoided due to the bulk effect averaging out any local inhomogeneities during the initial testing.

The main strengthening factor in AA2196 is assumed to be precipitation hardening, mostly through the existence of two main strengthening particles, T_1, Al_2CuLi, and θ', Al_2Cu. In this master's thesis, it has been assumed that the increased stress in the material induced during cold work due to an increase in dislocation density has been relieved. However, as the total solid solution heat treatment time was relatively short, approximately 60 minutes plus 30 minutes heating, it may not have been sufficient time to reduce the dislocation density by a large extent. As there was a decrease in strength with an increase in cold work, the strain hardening induced prior to solutionising heat treatment seems to be of little direct consequence when determining the strength of the material.

Nevertheless, cold work may play an important indirect role as the precipitate distribution is governed by the distribution of dislocations, due to dislocations being favourable nucleation sites, particularly for T_1. T_1 precipitates with a high-density both in the matrix and on grain boundaries (Hekmat-Ardakan et al., 2012), and could be beneficial for the strengthening process. However, this requires the existence of any remaining dislocations following solutionising treatment or introduction of dislocations after solid solution treatment through cold work. In the case of this heat treatment, it is unlikely that there was a high density of dislocations following solid solution heat treatment, consequently reducing the overall strength of the material due to less T_1 precipitated.

Introducing a deformation step following solid solution strengthening, effectively making the heat treatment a T8 process, may increase the performance of the material significantly and may help mitigate the precipitate free zones experienced in previous Al-Li alloy generations due to the precipitation of T_1 on dislocations (Hekmat-Ardakan et al., 2012) (Jha, Sanders, & Dayananda, 1987), thus improving the reliability of the material by preventing any stress concentrations. Additionally, cold work prevents precipitates from forming on the grain boundaries (Rioja & Liu, 2012). Additionally, a significant amount of the strength and toughness increase experienced after cold work prior to aging is a consequence of the increased precipitation of T_1. Furthermore, a deformation step would facilitate the improvement of the heat treatment process using in this master's thesis, as there would be two main sources of strengthening in the alloy, instead of one.

A point worth noting if any machining or deformation on AA2196 is to be conducted is that significant cracks formed for AA2196 cold deformed more than 70%, seen in Figure 28. Hence, the material has some design limitations in the number of shapes it may be deformed to avoid the possibility of fracture.

Comparing the yield and tensile strengths of 9.1-56.3%CW of AA2196 with those of AA7090, it was found that AA7090 exhibited a significantly higher strength at the cost of ductility, although the tensile toughness of AA2196 and AA7090 were relatively similar. Additionally, the specific strength of AA7090 was found to be superior to that of AA2196, as seen in Table 23 to be averaged to 249.7 kPa m^3/kg. However, the specific strength found for AA2196 prior to any heat treatment was almost identical, 252.0 kPa m^3/kg, to the one found for 9.2%CW AA7090, thusly showing the potential of AA2196. As the specific strength seemed to decrease with an increase in cold work, the specific strength of non-cold worked AA7090 might be higher than AA2196-T8511, if it is assumed that the heat treatment

conducted for 0%CW AA7090 were not appropriately conducted due to furnace temperature deviation. Nevertheless, both AA2196 and AA7090 show the potential for excellent specific strength.

A result of increased cold worked were appeared to be a significant increase in strain hardening for both AA2196 and AA7090. Comparison between AA2196 and AA7090 showed that the AA2196 alloy was able to withstand a considerably higher amount of strain hardening, approximately 111 MPa to 44 MPa at 39.0%CW, thus bridging some of the substantial gap in strength between AA2196 and AA7090. For aerospace applications, strain hardening may be an important factor, as it increases the plastic elongation and thus increases toughness. Additionally, strain hardening may be beneficial during machining of parts and since an increased strain hardening will increase the amount of strain required in order to achieve plastic instability, i.e. localised deformation, thus making it an easier material to work with.

The increase in ductility and decrease in hardness with increased cold work may be affected by to two competing phenomena, recovery and recrystallisation. As seen from Figure 8, recrystallisation, the nucleation of new grains, leads to a decrease in strength but with the benefit of an increase in ductility. As both recovery and recrystallisation results in a decrease in internal strain, one will therefore only expand at the cost of the other.

Examination of the LOM pictures for pressing in the extrusion and the transverse direction reveals a microstructure that is similar to the microstructure seen prior to heat treatment, suggesting that little, if any, recrystallisation have occurred. Considering the decrease in average grain size with an increase in percent cold work and the OM pictures showing no signs of recrystallisation, it is natural to assume that a significant amount of the material has been recovered at 19.9-55.5% cold work when pressed in the extrusion direction. This corresponds well with literature, as increased dislocation density will result in a larger driving force for both recrystallisation and recovery.

Consequently, AA2196 seems to have an outstanding ability to resist recrystallisation. It is thought that a combination of effects may have affected the recrystallisation ability for AA2196, such as the fact that several alloying elements have been added to retard the recrystallisation process in AA2196, such as Mn, Mg, Zr and Ti, and due to Cu and Li in solid solution. Zr and Mn alloying elements are supposed to hinder recrystallisation by Zener pinning. Solutes such as Cu and Li hinder recrystallisation by retarding the grain boundary mobility, though recovery is allowed to occur (Engler, 1999).

By examining the LOM photos for pressing in the extrusion direction, the grain size in the transverse direction seemed to increase with an increase in cold work, although the pictures appeared to agree with the EBSD data that the grain size in the pressed extrusion direction decreased. When pressing in the transverse direction, no significant change in grain size was measured until the samples were pressed 58.7%. The LOM photos for pressing in the transverse direction showed a decrease in grain size for the extrusion direction with increased cold work. Additionally, the LOM pictures in Appendix D for the non-pressed transverse direction showed similar results with grain size, the grain size increased when pressing in the extrusion direction and decreased when pressing in the other transverse direction. Consequently, it may be beneficial for the material as a whole to cold work in the transverse direction when constructing parts out of AA2196, as there appeared to be two directions with a noticeable decrease in grain size instead of just one as was the case for

the extrusion direction. Although, it should be noted that 58.7%CW is required to get any significant change in grain size in the cold pressed transverse direction.

In contrast, the average grain size found for the initial T8511 heat-treated material was 10.8 µm in the extrusion direction and 3.1 µm in the transverse direction. Noticeably, the average grain size was lower in the transverse direction, where elongated grains are expected, than in the extrusion direction, where smaller rounder grains were expected. The fraction distribution in the transverse direction suggests that the length of the elongated grains vary significantly, while the fraction distribution for the extrusion direction suggests relatively round grains with approximately the same length in each direction. Interestingly, the grain size in the transverse direction was significantly shorter than those found after cold pressing, while in the extrusion direction approximately 19.9% cold pressing was required in order to get finer grains than those observed prior to any heat treatment.

Local variation in both AA7090 and AA2196 seem to play a significant role in the performance of the material, for example for 9.2%CW AA7090, Figure 61, where there was a quite large variation in ductility and strength, with the difference in yield strength being 661 MPa at the lowest and 743 MPa at the highest and %elongation ranging from 1.36 to 4.75%. Similar, although not as distinct variations, may be observed at other percent cold worked of AA7090 and in AA2196. These variations may be due to inhomogeneity included during heat treatment, or it may be due to natural local variations in a material that will have a significant effect, especially as small tensile test rods were used.

Considering that strength is an important factor when designing propulsion systems for aerospace applications, AA7090 might seem to be a better candidate. However, high ductility and damage tolerance are also important factors(Rioja & Liu, 2012), which are factors that speak in the favour of AA2196. Charpy testing was conducted on both 0-56.3%CW AA2196 and 0-39.1%CW AA7090. The overall fracture energies absorbed in AA2196 were significantly higher than those obtained for AA7090, with values ranging 23.59-7.50 J and 2.86-1.54 J respectively. While the overall fracture energy for AA7090 was relatively stable until 39.1%CW, AA2196 suffered a persistent decline in fracture energy with increased cold work. The larger fracture energy of AA2196 corresponds well with literature, as AA2196 is claimed to have a large damage tolerance (Uféras, 2017b). It should be noted that as the ductility and tensile toughness of the AA2196 increases, the damage tolerance decreases.

Additionally, while fracture energies for AA7090 were relatively stable, there was a large variance within a group of similar samples. This variance may be due to inhomogeneities within the material, causing their properties to vary, though these variations may be local (Dieter, 1988e). Furthermore, the variance may be due to user error, as the samples were placed manually on a platform in front of the pendulum. As seen in Figure 50, there was significant deformation of the AA2196 Charpy samples, suggesting that some energy has been absorbed in order to propagate the crack and thus a more ductile fracture. AA7090, on the other hand, experienced a more granular fracture, which may signify a less ductile nature. This corresponds well with both literature (Dieter, 1988e) and with tensile testing where AA2196 also was found to generally have a higher elongation. An example graph showing the propagation energy during Charpy testing may be seen in Figure 16. To further investigate the fracture energies, an instrumented Charpy tester should be used. Thusly, the initiation energy and the propagation energy could be decided, thereby allowing a better comparison between AA2196 and AA7090 and their ductile nature.

The homogeneity within a Charpy sample was investigated in two ways, firstly by hardness testing and by OM pictures. It was discovered that there was a slight change in hardness between 0.5 mm into a sample and 2.5 mm into the sample. The hardness values were 132.8 HV5 and 138.2 HV5 respectively. By examining the LOM pictures, Figure 51 and Figure 52, there appears to be a decrease in grain size further into the material. Hence, it is reasonable to assume that the Charpy samples were not homogenous throughout the samples. Furthermore, the lower grain size seems to indicate that there might have been a discrepancy between the surface of samples and the core temperatures, mayhap due to slow heating, causing grain growth in at the surface but not within the sample core. This grain growth may be a consequence of the samples being placed on a stone within the furnaces during heat treatment, effectively making a heating source for one of the surfaces of the sample.

Initial tensile testing of 0%CW AA7090 showed a relatively low yield strength, 401-422 MPa, when compared with the highest strengths obtained for cold worked AA7090, 679-748 MPa. Additionally, 0%CW AA7090 exhibited a high ductility, with elongation in the range of 10.17-11.45%. Consequently, this uncharacteristic low strength and high ductility of 0%CW AA7090 compared to 9.2-39.1% CW may be the result of incorrect heat treatment as it cannot be guaranteed that these tensile test rods were not heat treated using the faulty furnace N11/R. The tensile testing rods of 0%CW AA7090 were heat treated prior to the discovery that the furnace temperature within N11/HR was significantly lower than those desired. However, these deviations from the trend seen for 9.2-39.1%CW AA709 may be due to inhomogeneities within the extrusion delivered from NAMMO Raufoss.

Figure 53 shows that there was a deviation between the display and the furnace air 5 mm above the sample, and the deviations are summarised in Table 11. By observing this table, a major temperature deviation is noticed for all holding temperatures used at various stages in heat treatment. Annealing was conducted at a lower temperature than desired, solid solution treatment was conducted at a temperature below 500°C where the documented single-phase exists and precipitation hardening was effectively conducted at approximately 30°C lower than desired. However, as precipitation curves were still obtained, it may be assumed that the single-phase area exists at a lower temperature than 500°C or that the samples eventually reached 500°C, as all were subjected to precipitation hardening.

As no definitive answer can be given regarding the temperature for the various aging curves for AA2196 and AA7090, each graph should be viewed with some scepticism. Although the temperature deviation between the N11/R display and the actual temperature experienced were found to be approximately 30°C, the aging curves cannot be viewed as simply 30°C lower than the given temperature, as some curves might have been heat-treated in other furnaces and therefore the given temperature would be correct. However, these precipitation curves may be used as indications that an increased aging time will result in increased hardness and consequently also an increase in strength (van Mourik, van Dam, & Picken, 2012) (Ceschini, Morri, Morri, Gamberini, & Messieri, 2009) due to the tendency for all samples used for an aging curve to be heat treated using the same furnace, thus allowing for some trends with respect to time to be observed.

N11/R was not used for aging at 160°C, though prior heat treatment cannot be guaranteed, and the hardness decrease after 20 hours suggests that the material might have reached peak hardness somewhere between 16 and 20 hours and therefore have been overaged at 20 hours. Additionally, the hardness of AA7090 was found to be significantly higher than that of AA2196, suggesting that AA7090 may have intrinsically a higher strength. Initial

tensile testing supports this claim, as the strength of AA7090 was found to be significantly higher. For AA7090, there was little change in hardness with respect to time, suggesting that either AA7090 has other main strengthening mechanisms or that the temperature was insufficient in reaching peak hardness within the timeframe.

As seen in Figure 2, AA2196 reaches a single phase area at 500°C, causing alloying elements to go in solid solution. The heating time for the alloy test piece to a temperature above 500°C was approximately 78 minutes, observed from Figure 56 and given in Table 12. Consequently, when a holding time of 60 minutes was used and with a heating time to 500°C of approximately 23 minutes, the actual holding time was close to 5 minutes, indicated by Table 13. For such a low holding time it is reasonable to assume that the alloy had not reached equilibrium, and hence that there may be alloying elements not in solid solution and thus there may be phases present that were formed during annealing. A lower supersaturation of alloying elements will result in a lower precipitation rate than a higher one and thus a lower strength material (Dieter, 1988b). As a result, significant strength improvements for AA2196 may be achieved by increasing the holding time above 500°C.

Similarly to the solid solution heat treatment temperature, the annealing temperature, 400±5°C, was reached much later than anticipated. With a heating time of 124 minutes to reach 395°C, the holding time was just 24 minutes instead of 120 minutes as thought when estimating a 25-minute heating time for the furnace. Hence, the annealing of the alloy was undergone at a lower temperature than desired and may have led to an unsuccessful attempt at relieving the alloy of internal stress and may be a reason why recrystallisation have not been observed in any OM photos. Due to recovery behind favoured at lower temperatures, such as observed by Engler (1999) at 350°C, a temperature close to what the cold pressed samples may have experienced, this is likely to have affected the overall recrystallisation rate.

During the slow cooling from 400°C to 250°C with a rate of 0.5°C/min, the material was found to follow reasonably well. The deviation became larger the closer to 250°C the temperature got, but with the sample holding a temperature of 260°C after the 6 hours of cooling. Thusly proving that this cooling method was effective.

After reaching 250°C, the furnace doors were opened in order to provide a middle ground between slow cooling within the furnace and rapid cooling in air. During the 132 minutes waited for this test, a sample cooled from 250°C to 62.5°C. Contrary to the linear cooling of 1°C/min within the furnace, a more exponential decay was experienced, seen in Figure 55. However, as the temperature had sunk 100°C within the first 20 minutes, the rate of cooling was substantially slower than that of water or air quenching, hence making it a viable option when slow cooling is desired. It should be noted that as the samples were placed on a stone which may have effectively acted as a heating source, there was likely a temperature gradient within the material, which may have caused an inhomogeneous material to form. Hence, this may explain the discrepancy observed for the Charpy sample between the core and the surface.

For aging it was found that time until designated temperature, 160±1°C, was 156 minutes. Due to a holding time of 12 hours, 720 minutes, there is little consequence for the aging other than that the actual aging at that temperature was close to 564 minutes and that the

alloy was aged for some time at a lower temperature which may have resulted in other precipitates forming such as GP-zones, θ″ and δ′. Increased precipitation hardening temperature would be an effective method to increase the precipitation rate, thus compensating for the reduced aging time. To achieve an increased precipitation rate, the temperature could be increased from 160°C to 180-240°C, as in this area according to Figure 6 the time until nucleation is shortened. Additionally, the same main strengthening particles, T_1 and θ′, would still form.

Prior to heat treatment, a texture was observed. This texture corresponds well with the extrusion texture seen in Figure 9 for an Al-Li alloy. By examining the pole figures for samples heat treated in both the extrusion direction and the transverse direction a clear extrusion texture can be seen initially. As the amount of cold work increased, the texture seemed to become less and less prominent, as for 19.9% and 40.5%CW in the extrusion direction the texture was faintly visible. However, for 55.5% CW the texture seems to become clearer. By examining Figure 46 and comparing it to Figure 11, the inverse pole figure for uniaxially compressed Cu, there seems to be a similarity. Both are clustered around the ⟨110⟩ fiber and both have been compressed. As the sample of 55.5%CW AA2196 were slightly crooked, it is unreasonable to assume that the compression has been uniaxially, but reasonable to approximate uniaxial compression. Consequently, by cold pressing the AA2196 55.5% in the extrusion direction in order to remove texture, a new texture has been created. It should be noted that there may be some extrusion texture left in the 55.5%CW sample, as the rings seen in the pole figures are prominent and could very well be extrusion texture.

For 40.1% and 58.7%CW in the transverse direction, there was little trace of the extrusion texture. Instead, there were several clusters around the pressed transverse direction, which share some similarities with the cube texture seen in Figure 10 a) and b). However, as AA2196 contains a significant amount of copper, 3.07 wt%, there may be some R orientation as well, especially for 58.7%CW where the cubic structure was less visible and may instead be a mixture of cube and R orientation. Both cube and R structure are typical recrystallisation structures, signifying that significant recovery must have occurred, as there was little indication that recrystallisation has occurred. Nevertheless, both cases showed signs of a clear texture, even though the texture was different than the initial extrusion texture.

According to Engler (1999), a high annealing temperature will result in the cube orientation formation instead of R formation. In addition, Li additions slow down the grain boundary mobility, which is vital for cube orientation formation, leading to more R orientation formed. This may have been the case for this alloy, as the annealing temperature used was the solid solution temperature of 530°C, though approximately 505°C was the most experienced by the material. As there seemed to be more of a cube structure for both 40.1% and 58.7%CW in the transverse direction, this seems to be a likely occurrence.

As a result of the little, if any, recrystallisation observed in AA2196, there has been little nucleation of grains with a random orientation, hence not combating the texture seen prior, and after, heat treatment. Consequently, cold work prior to solid solution treatment may not be the most effective method for dampening the texture seen.

It should be noted that the texture profile of compression is simple compared to other cold working methods such as cold rolling. Consequently, the texture formation may become increasingly complicated by adding cold rolling, especially as the R orientation during recrystallisation and recovery is similar to a previous cold rolling texture known as S orientation and may nucleate on said orientation (Engler, 1999).

Considerably better results may be achieved with a lower volume of air compared to the sample size, by lowering the height of the furnace and increasing the heating rate, thus lowering the temperature differences within the furnace. A lower volume of air would result in a less air to heat and therefore increase the heating rate. Additionally, each heat-treated sample was placed on a stone, effectively making an insulator on one side of the samples. As a result, the assumption that every heat treated AA2196 piece was homogeneous is unrealistic, given the low holding time during solutionising heat treatment and the uneven temperature gradient within the furnaces. Uniform heating from the top and the bottom of the furnace should improve homogeneity within the material. Combining top and bottom heating with the aforementioned lower furnace height would result in a decreased temperature gradient within the furnace, thusly the temperature within the furnace would be more uniform.

Due to the relatively short heating time for solutionising treatment, there may not have been enough time for considerable grain growth to occur. However, if the holding time were to be increased to get a larger amount of Li and Cu in solid solution to get a more effective precipitation hardening, it would be at the risk of larger grains and thus a lower strength. Due to the presence of recrystallisation retarding effects, an increase in solid solution heat treatment holding time may be a beneficial choice, especially as only a minor increase in time would result in a considerable increase in the fraction of time spent above 500°C. This may also lead to the grain growth of sub-grains, which may grow to become high-angle grains.

Pre-heating prior to solutionising treatment and annealing might be beneficial in order to achieve the desired temperatures at a faster rate. This heating should be conducted at a sufficiently low temperature that there is no phase transformation nor dissolution of any of the beneficial particles within AA2196. In addition, an argon atmosphere or similar atmosphere might be advantageous to prevent any lithium from reacting with oxygen or hydroxide to form lithium oxide or lithium hydroxide. However, for this master's thesis, aluminium foil has proven a sufficient cover for the samples at elevated temperatures as no determinantal effects have been discovered due to lithium oxide nor lithium hydroxide. However, as both lithium oxide and lithium hydroxide are corrosive, safety considerations should be implemented during large scale production.

In order to reach the precipitation hardening temperature more rapidly, a salt bath could be beneficial. An important note is that Al-Li has explosion potential with a salt bath if the alloy is treated to temperatures in which the alloy begins to melt. At temperatures safely below this threshold, a salt bath may be an excellent alternative. Due to safety considerations, a salt bath was not chosen for this master's thesis, as the melting range of AA2196 is in the range of 508-648°C (Tian et al., 2016). However, a salt bath would be an effective method to increase the heating rate during solid solution heat treatment or artificial aging.

A central role in determining whether AA2196 would be a good candidate for aerospace applications would be to determine the properties of AA2196 in the transverse direction and 45° and 60° to the extrusion direction. Generally, 45° and 60° to the extrusion direction, in addition to the transverse direction, is where third-generation Al-Li alloys exhibit most texture (Jata, Panchanadeeswaran, & Vasudevan, 1998). Sadly, due to the lack of proper machining tools, this could not be done in this master's thesis, but it is recommended to examine such properties before any design decisions are made. Both tensile testing and Charpy testing would be beneficial, although tensile testing would be of most importance. In addition, similar tests should be conducted on AA7090, thus giving a better view into both the respective alloy's potential applicability.

Considering the fact that the degree of texture seemed to decline with increased amounts of cold work, it would be expected that the anisotropic effect would be lessened and that the tensile testing rods for samples highly cold worked prior to solid solution heat treatment would perform better compared to their extrusion direction strength. Similarly, Charpy samples from said samples would be expected to have a closer value to those values found for the extrusion direction in this master's thesis.

During this master's thesis, AA2196 has been allowed to naturally age for 24 hours. During natural aging δ′ particles are formed. δ′ were the main strengthening particles for earlier Al-Li alloy generations. δ′ decreases the fracture toughness of a material by precipitating on grain boundaries and may also increase the gravity of planar slip. Hence, it may be beneficial to reduce natural aging as much as possible. However, due to practical considerations, some natural aging should be allowed to occur as it is not practical to not allow for any time delay. Thusly, 24 hours have been chosen due to this being deemed the most realistic delay expected for the industry. From Figure 3 it can be seen that the natural aging slows down after approximately 24 hours, which may signify that further delay before commencing artificial aging would be of little consequence, within a reasonable timeframe.

It should be noted that there is substantial uncertainty for some of the values found during this master's thesis. There is the built-in uncertainty for the hardness tester and the tensile testing machine, in addition to user error. In addition, there would be uncertainty due to local variation and inhomogeneity in the material. Hardness tests were used to discover overarching trends and would therefore have little impact on the overall result. Similarly, tensile testing should be conducted in a larger volume to precisely determine the mean strength and ductility of AA2196 and AA7090. When determining the amount of cold work the initial and resulting height was measured by hand using a sliding gauge, and should therefore represent estimations of overarching trends as the amount of cold work within a sample may vary.

For thermocouples and the logged temperature, there were to main sources of uncertainty, the error from the thermocouples themselves and for the data logger. In this master's thesis, it has been assumed that the uncertainty was the sum of the individual components but it is likely that there is some correlation between the sensor and the reading device. However, as it was not given in the manual for the data logger, it has been assumed that the uncertainty is not the standard deviation, and hence such formulas for combining the uncertainty have not been used.

The uncertainty for the furnaces used has been attempted to chart using the aforementioned data logger and thermocouples to facilitate the usage of the data found in this report for further use. The uncertainty regarding Charpy testing included the uncertainty for the Charpy tester, and the far larger uncertainty of user error. Charpy samples were placed manually, and there is therefore the risk that each sample has not been placed correctly, both concerning the distance from the pendulum and when centralising the notch with respect to the pendulum strike area.

It may be beneficial to investigate the usage of AA2195 instead of AA2196. AA2195 has been used in propulsion systems for a significant amount of time and has, among other things, excellent cryogenic properties which may play a significant role. Additionally, according to the AA2195 has a higher modulus of elasticity and higher strength in the longitudinal direction, 555 MPa compared to 538 MPa, at the cost of a slightly higher density (Uféras, 2017a, 2017b). It should be noted that AA2195 is delivered as a cold-rolled sheet, which may complicate the anisotropic behaviour when compared to the extruded AA2196, as the cold rolled texture is more complicated and diverse than the extruded texture seen in this master's thesis. Additionally, cold rolling may lead to a more advanced recrystallisation texture by initiating more R orientation formation. Due to the similarities between AA2195 and AA2196, this thesis may be a good basis to use as an indication.

During testing of AA7090 and AA2196 in this paper, both alloys have displayed excellent properties. AA2196 generally exhibited the highest ductility and damage tolerance, while AA7090 had a substantially higher strength. Both alloys showed, coincidentally, a quite similar tensile toughness. As the strength, and especially specific strength, is of vital importance for the aerospace industry, AA7090 is thought to be the most suitable candidate. However, it should be noted that there are vast areas for improvement for the heat treatment process conducted in this master's thesis that may vastly improve the properties of AA2196. In addition, the specific strength exhibited by AA2196 prior to heat treatment were similar to those obtained for AA7090. Thus, further study into AA2196 is recommended, as it is thought that AA2196 has considerable potential and may prove to be an excellent and versatile alloy.

6. Conclusion

A heat treatment process involving annealing, solid solution treatment, cold working and precipitation hardening was conducted on an AA2196-T8511 treated alloy delivered from Constellium. Prior to artificial aging, the alloy was allowed to naturally age for 24 hours. The process was conducted successfully and resulted in a strength and hardness increase following precipitation hardening compared to the annealed state. Consequently, this process may be utilized in order to increase the malleability of the alloy, manufacture aerospace, or other, components and subsequently get a high strength aluminium alloy using precipitation hardening.

Tensile testing of an approximately 10%CW AA2196 sample was found to give an average yield strength of 435 MPa, a tensile strength of 525 MPa and an elongation of 7.84%, compared to the initial values of 656MPa, 663 MPa and 5.68 % for the T8511 treated material. With an increase in cold work, the strength was found to decrease while the elongation increased, giving a resulting average of 321 MPa yield strength, 440 MPa tensile strength and 15.49% elongation for a 56.3 %CW AA2196 sample. There was registered a decrease in strength and increase in ductility when compared to similarly deformed AA7090. Tensile testing of AA7090 reviled a significantly higher strength than AA2196, although there was a large discrepancy between 0%CW and 9.2%CW AA7090, ranging from an average of 296MPa yield strength, 412 MPa tensile strength and 10.81% elongation to 691 MPa, 707 MPa and 3.37%. In addition to exhibiting the highest strength, AA7090 also exhibited the highest average specific strength of 249.7 kPa m^3/kg. Similar tensile toughness was found for both AA2196 and AA7090 and was found to increase with the amount of cold work.

Charpy testing resulted in a fibrous fracture for AA2196 and a significantly higher fracture energy in comparison to the more granular fracture for AA7090. It is assumed that some of the energy absorbed for AA2196 was in fact propagation energy, thus giving a higher measured fracture energy. An increase in the amount of cold work resulted in a decrease in fracture energy absorbed for AA2196. AA7090 Charpy samples absorbed substantially lower amounts of energy, in the range of 1.34-2.86J, while AA2196 absorbed energy in the range of 7.5-23.59J. An AA2196 Charpy sample was hardness tested and examined using a LOM both 0.54 mm into the sample and 2.53mm into a 5mm thick sample. It was found that at the centre of the sample there were a minor hardness increase and there appeared to be a reduction in grain size.

The grain size was found to decrease in the direction of the cold work with increased cold pressing. This was supported by LOM pictures of the same samples, which seemed to give a similar indication. Additionally, LOM pictures of the cold pressed samples suggested that when pressed in the extrusion direction, the grain size in both of the transverse direction would increase. On the contrary, when pressed in a transverse direction, the grain size in the non-pressed transverse direction and the extrusion direction seemed to decrease. Initial EBSD of the T8511 treated AA2196 suggested a grain size of 10.8 μm in the extrusion direction and 3.1 μm in the transverse direction. A lower grain size than the initial grain size was achieved in the extrusion direction with more than 19.9% CW, resulting in a final grain size of 7.8 μm. The finest grain size achieved in the transverse direction were 7.6 μm after 58.7 %CW, thus noticeably higher than the initial grain size. Examination of the OM pictures

revealed no recrystallisation, hence it is assumed that the reduction in grain size is due to nucleation and growth of sub-grains.

EBSD analysis suggested that AA2196-T8511 exhibited anisotropic behaviour, due to extrusion texture being displayed. After heat treatment, a similar texture was found. By increasing the amount of cold work, the extrusion texture was lessened. However, if the sample were cold pressed 55.5% in the extrusion direction, a signature texture due to uniaxial compression was seen using an inverse pole figure. Similarly, 40.1.-58.7%CW in the transverse direction resulted in what seemed to be recrystallisation texture, particularly cube orientation. For 19.9-40.5%CW in the extrusion direction, only a weak extrusion texture was seen, suggesting the most optimal amount of cold work to be in this range when considering texture.

Data logging revealed that the solid solution heat treatment holding time was not 60 minutes at 530°C as assumed, but 5 minutes above 500°C, where there is proven to be a single-phase area. Consequently, full solid solution of Cu and Li may not have been achieved. Furthermore, a discrepancy was found between the display temperature and the furnace temperature where samples were placed for the furnace N11/R. Consequently, the aging curves constructed at 150°C, 160°C and 180°C for AA2196 are unreliable, as well as the tensile testing rods of 0%CW AA7090 and the aging curve for AA7090 at 120°C. This discrepancy may explain the large variation in strength and ductility between 0%CW and 9.2%CW AA7090. Due to the temperature deviation in a furnace that have been used at various points during the heat treatment of the aging curves, their values must be considered a tendency at best.

Aging curves for AA2196 were conducted at 150°C, 160°C and 180°C, between 6-20 hours. An increase in precipitation hardening time generally resulted in an increase in hardness. AA7090 was aged for 8-24 hours at 120°C, and did not show a substantial increase in hardness, although all hardness values were higher than those found for AA2196.

Several suggestions have been made in order to improve the performance of the heat treatment, such as prolonging the holding time at 530°C, pre-heating prior to annealing and solutionising, introducing a deformation step after solid solution strengthening and to introduce a low volume to area furnace in order to dampen air temperature fluctuations. It is argued that one of the main strengthening particles, T_1, precipitates on dislocations. This would cause both higher strength and an increased toughness, thus justifying the increased effort as the alloy may be vastly improved. AA2195 may be a suitable material in propulsion systems for aerospace applications and has been proposed as an alternative.

Due to AA7090 exhibiting the highest specific strength, AA7090 has been proposed as the initial best candidate, despite the fact that AA7090 was a less ductile material than AA2196. However, due to the wide array of potential improvements in the heat treatment process and the excellent properties exhibited for AA2196 prior to heat treatment, a further development of the heat treatment process for AA2196 is recommended and may provide a different result.

7. References

Abd El-Aty, A., Xu, Y., Guo, X., Zhang, S.-H., Ma, Y., & Chen, D. (2018). Strengthening mechanisms, deformation behavior, and anisotropic mechanical properties of Al-Li alloys: A review. *Journal of Advanced Research, 10*, 49-67. doi:10.1016/j.jare.2017.12.004

Ahlborn, H., Hornbogen, E., & Köster, U. (1969). Recrystallisation mechanism and annealing texture in aluminium-copper alloys. *Journal of Materials Science, 4*(11), 944-950. doi:10.1007/BF00555308

Alekseev, A. A., & Lukina, E. A. (2016). Solid-solution thermodynamics in Al–Li alloys. *The Physics of Metals and Metallography, 117*(5), 466-471. doi:10.1134/S0031918X16050021

Alekseev, A. A., Zhuravleva, P. L., Onuchina, M. R., & Klochkova, Y. Y. (2015). Mechanisms of formation of hardening precipitates and hardening in aging of al-li-cu-mg model alloys with silver additions. *Russian Metallurgy (Metally), 2015*(11), 923-928. doi:10.1134/S0036029515110038

Bjerkestrand, V. J. (2018). *Characterization and Mechanical Testing of Co-Extruded Rods with an AA6082 Core and Rapidly Solidified AA7090/AA7090-Sc Sleeve.* (Master's), NTNU, Gløshaugen.

Blackman, A. G., Gahan, L. R., Aylward, G. H., & Findlay, T. J. V. (2014). *Aylward and Findlay's SI Chemical Data/ Allan Glackman Lawrence Gahan* (7th ed.): John Wiley & Sons Australia, Ltd.

Bray, G. H., Glazov, M., Rioja, R. J., Li, D., & Gangloff, R. P. (2001). Effect of artificial aging on the fatigue crack propagation resistance of 2000 series aluminum alloys. *International Journal of Fatigue, 23*, 265-276. doi:10.1016/S0142-1123(01)00159-1

Callister Jr, W. D., & Rethwisch, D. G. (2015a). 3.10 Anisotropy. In *Materials Science and Engineering SI VERSION* (Ninth ed., pp. 67-69): Wiley.

Callister Jr, W. D., & Rethwisch, D. G. (2015b). 6.4 Impurities in Solids. In *Materials Science and Engineering SI VERSION* (Ninth ed., pp. 149-151): Wiley.

Callister Jr, W. D., & Rethwisch, D. G. (2015c). 8 Mechanical Properties of Metals. In *Materials Science and Engineering SI VERSION* (Ninth ed., pp. 208-245): Wiley.

Callister Jr, W. D., & Rethwisch, D. G. (2015d). 9.8 Strengthening by Grain Size Reduction. In *Materials Science and Engineering SI VERSION* (Ninth ed., pp. 266-268): Wiley.

Callister Jr, W. D., & Rethwisch, D. G. (2015e). 9.10 Strain Hardening. In *Materials Science and Engineering SI VERSION* (Ninth ed., pp. 269-272): Wiley.

Callister Jr, W. D., & Rethwisch, D. G. (2015f). 13.5 Aluminium and its alloys. In *Materials Science and Engineering SI VERSION* (Ninth ed., pp. 447-450): Wiley.

Callister Jr, W. D., & Rethwisch, D. G. (2015g). 17.5 Annealing Processes. In *Materials Science and Engineering SI VERSION* (Ninth ed., pp. 591-593): Wiley.

Callister Jr, W. D., & Rethwisch, D. G. (2015h). 17.7 Precipitation hardening. In *Materials Science and Engineering SI VERSION* (Ninth ed., pp. 603-610): Wiley.

Callister Jr, W. D., & Rethwisch, D. G. (2015i). Glossary. In *Materials Science and Engineering SI VERSION* (Ninth ed., pp. 871): Wiley.

Ceschini, L., Morri, A., Morri, A., Gamberini, A., & Messieri, S. (2009). Correlation between ultimate tensile strength and solidification microstructure for the sand cast A357 aluminium alloy. *Materials & Design, 30*(10), 4525-4531. doi:10.1016/j.matdes.2009.05.012

Chen, P. S., & Bhat, B. N. (2002). Time-temperature-precipitaion behaviour in Al-Li alloy 2195. *Marshall Space Flight Center, MSFC Engineering Directorate*.

Daniélou, A., Ronxin, J. P., Nardin, C., & Ehrström, J. C. (2016, 2016//). *Fatigue Resistance of Al-Cu-Li and Comparison with 7xxx Aerospace Alloys.* Paper presented at the ICAA13 Pittsburgh, Cham.

Deschamps, A., de Geuser, F., Decreus, B., & Malard, B. (2012). Precipitation in Al-Cu-Li alloys: from the kinetics of T1 phase precipitation to microstructure development in friction stir welds. In H.

Weiland, A. D. Rollett, & W. A. Cassada (Eds.), *ICAA13 Pittsburgh* (pp. 1145-1154): Springer, Cham.

Deschamps, A., Decreus, B., De Geuser, F., Dorin, T., & Weyland, M. (2013). The influence of precipitation on plastic deformation of Al–Cu–Li alloys. *Acta Materialia, 61*(11), 4010-4021. doi:10.1016/j.actamat.2013.03.015

Dieter, G. E. (1988a). 6-7 Solid-Solution Strengthening. In D. Bacon (Ed.), *Mechanical Metallurgy, SI Metric Edition* (3rd ed., pp. 203-207). Singapore: McGraw-Hill Book Company.

Dieter, G. E. (1988b). 6-9 Strengthening from fine particle. In D. Bacon (Ed.), *Mechanical Metallurgy, SI Metric Edition* (3rd ed., pp. 212-220). Singapore: McGraw-Hill Book Company.

Dieter, G. E. (1988c). 6-14 Strain Hardening. In D. Bacon (Ed.), *Mechanical Metallurgy, SI Metric Edition* (3rd ed., pp. 231-233). Singapore: McGraw-Hill Book Company.

Dieter, G. E. (1988d). Chapter Eighteen Extrusion. In D. Bacon (Ed.), *Mechanical Metallurgy, SI Metric Edition* (3rd ed., pp. 616-634). Singapore: McGraw-Hill Book Company.

Dieter, G. E. (1988e). Part 3 Application to Materials Testing. In D. Bacon (Ed.), *Mechanical Metallurgy, SI Metric Edition* (3rd ed., pp. 275-500). Singapore: McGraw-Hill Book Company.

Draissia, M., & Debili, M.-Y. (2005). Study of solid-solution hardening in binary aluminium-based alloys. *Central European Journal of Physics, 3*(3), 395-408. doi:10.2478/BF02475646

Du, Y.-x., Zhang, X.-m., Ye, L.-y., & Liu, S.-d. (2006). Evolution of grain structure in AA2195 Al-Li alloy plate during recrystallization. *Transactions of Nonferrous Metals Society of China, 16*(2), 321-326. doi:10.1016/S1003-6326(06)60055-1

Dursun, T., & Soutis, C. (2014). Recent developments in advanced aircraft aluminium alloys. *Materials & Design (1980-2015), 56*, 862-871. doi:10.1016/j.matdes.2013.12.002

Elgallad, E. M., Lai, J., & Chen, X. G. (2014). Precipitation hardening of AA2195 DC cast alloy. *Canadian Metallurgical Quarterly, 53*(4), 494-502. doi:10.1179/1879139514Y.0000000149

Engler, O. (1999). On the origin of the R orientation in the recrystallization textures of aluminum alloys. *Metallurgical and Materials Transactions A, 30*(6), 1517-1527. doi:10.1007/s11661-999-0088-7

Engler, O., & Randle, V. (2010). *Introduction to Texture Analysis. Macrotexture, Microtexture, and Orientation Mapping* (Second ed.). Boca Raton: CRC Press.

Frank, W. B., Haupin, W. E., Vogt, H., Bruno, M., Thonstad, J., Dawless, R. K., . . . Taiwo, O. A. (2009). Aluminum. In *Ullmann's Encyclopedia of Industrial Chemistry*.

Giummarra, C., Thomas, B., & Rioja, R. J. (2007). *New aluminum lithium alloys for aerospace applications.* Paper presented at the Proceedings of the light metals technology conference.

Hekmat-Ardakan, A., Elgallad, E. M., Ajersch, F., & Chen, X. G. (2012). Microstructural evolution and mechanical properties of as-cast and T6-treated AA2195 DC cast alloy. *Materials Science and Engineering: A, 558*, 76-81. doi:10.1016/j.msea.2012.07.075

Hjelen, J. (1989). *Scanning elektron-mikroskopi*. Metallurgisk institutt, Trondheim: Metallurgisk institutt, NTH.

Hugaas, B. A. (1985). *Effekt av kalddeformasjon på utherdingsforløpet til en Al-Li-Mg-Cu- legering*. Retrieved from Fysikalsk metallurgi, NTH

Humphreys, F. J., & Hatherly, M. (2004). *Recrystallization and related annealing phenomena* (Second Edition ed.). Kidlington, Oxford: Elsevier Ltd.

James, R. S. (1990). ASM Handbook, Volume 2: Properties and Selection: Nonferrous Alloys and Special-Purpose Materials. In A. H. Committee; (Ed.), *ASM Handbook* (Vol. Volume 2, pp. 178-199): ASM International.

Jata, K. V., Panchanadeeswaran, S., & Vasudevan, A. K. (1998). Evolution of texture, micro structure and mechanical property anisotropy in an Al-Li-Cu alloy. *Materials Science and Engineering: A, 257*(1), 37-46. doi:10.1016/S0921-5093(98)00822-3

Jazaeri, H., & Humphreys, F. J. (2004). The transition from discontinuous to continuous recrystallization in some aluminium alloys: II – annealing behaviour. *Acta Materialia, 52*(11), 3251-3262. doi:10.1016/j.actamat.2004.03.031

Jha, S. C., Sanders, T. H., & Dayananda, M. A. (1987). Grain boundary precipitate free zones in Al-Li alloys. *Acta Metallurgica, 35*(2), 473-482. doi:10.1016/0001-6160(87)90253-7

Jiang, N., Gao, X., & Zheng, Z.-q. (2010). Microstructure evolution of aluminum-lithium alloy 2195 undergoing commercial production. *Transactions of Nonferrous Metals Society of China, 20*(5), 740-745. doi:10.1016/S1003-6326(09)60207-7

Kim, J.-H., Jeun, J.-H., Chun, H.-J., Lee, Y. R., Yoo, J.-T., Yoon, J.-H., & Lee, H.-S. (2016). Effect of precipitates on mechanical properties of AA2195. *Journal of Alloys and Compounds, 669*, 187-198. doi:10.1016/j.jallcom.2016.01.229

Klein, J., Schneider, J., Muske, M., Gall, S., & Fuhs, W. (2004). Aluminium-induced crystallisation of amorphous silicon: influence of the aluminium layer on the process. *Thin Solid Films, 451-452*, 481-484. doi:10.1016/j.tsf.2003.11.009

Kyllingstad, R. B. (2018). *Hardening in an Al-Cu-Li Alloy for Aerospace Applications;*. Department of Materials Science and Engineering. Norwegian University of Science and Technology. Gløshaugen, Trondheim;.

Lossin, A. (2001). Copper. *Ullmann's Encyclopedia of Industrial Chemistry*. doi:10.1002/14356007.a07_471

Marioara, C. D., Andersen, S. J., Jansen, J., & Zandbergen, H. W. (2003). The influence of temperature and storage time at RT on nucleation of the β" phase in a 6082 Al–Mg–Si alloy. *Acta Materialia, 51*(3), 789-796. doi:10.1016/S1359-6454(02)00470-6

Metz, D. F., Weishaupt, E. R., Barkey, M. E., & Fairbee, B. S. (2012). A Microstructure and Microhardness Characterization of a Friction Plug Weld in Friction Stir Welded 2195 Al-Li. *Journal of Engineering Materials and Technology, 134*(2), 021005-021005-021007. doi:10.1115/1.4006066

Nayan, N., Narayana Murty, S. V. S., Jha, A. K., Pant, B., Sharma, S. C., George, K. M., & Sastry, G. V. S. (2014). Mechanical properties of aluminium–copper–lithium alloy AA2195 at cryogenic temperatures. *Materials & Design, 58*, 445-450. doi:10.1016/j.matdes.2014.02.024

Niedzinski, M. (2019). The Evolution of Constellium Al-Li Alloys for Space Launch and Crew Module Applications;. *Light Metal Age*(February issue), 36-42.

Noble, B., & Bray, S. E. (1998). On the α(Al)/δ'(Al3Li) metastable solvus in aluminium–lithium alloys. *Acta Materialia, 46*(17), 6163-6171. doi:10.1016/S1359-6454(98)00263-8

Petzow, G., & Effenberg, G. (1991). *Ternary Alloys. A Comprehensive Compendium of Evaluated Constitutional Data and Phase Diagrams. Al-Cd-Ce ... Al-Cu-Ru;* (Vol. 4): VCH Weinheim.

Prior, D. J., Boyle, A. P., Brenker, F., Cheadle, M. C., Day, A., Lopez, G., . . . Zetterström, L. (1999). The application of electron backscatter diffraction and orientation contrast imaging in the SEM to textural problems in rocks. In *American Mineralogist* (Vol. 84, pp. 1741).

Ringer, S. P., & Hono, K. (2000). Microstructural Evolution and Age Hardening in Aluminium Alloys: Atom Probe Field-Ion Microscopy and Transmission Electron Microscopy Studies. *Materials Characterization, 44*(1), 101-131. doi:10.1016/S1044-5803(99)00051-0

Rioja, R. J. (1998). Fabrication methods to manufacture isotropic Al-Li alloys and products for space and aerospace applications. *Materials Science and Engineering: A, 257*(1), 100-107. doi:10.1016/S0921-5093(98)00827-2

Rioja, R. J., & Liu, J. (2012). The Evolution of Al-Li Base Products for Aerospace and Space Applications. *Metallurgical and Materials Transactions A, 43*(9), 3325-3337. doi:10.1007/s11661-012-1155-z

Solberg, J. K. (2014). *Teknologiske metaller og legeringer*. NTNU, Trondheim: Norges teknisk-naturvitenskapelige universitet, Fakultet og institutt for materialteknologi.

Solberg, J. K. (2016). *Lysmikroskopi*. NTNU, Trondheim: Institutt for materialteknologi, Norges teknisk-naturvitenskapelige universitet.

Starke, E. A., Jr., Gangloff, R. P., Herakovich, C. T., Scully, J. R., Shiflet, G. J., Stoner, G. E., & Wert, J. A. (1995). NASA-UVA light aerospace alloy and structures technology program (LA2ST). *United States*.

The Aluminium Association Incorporated. (1979). Aluminium standards and data 1979. In *Appendix*.

Tian, Y., Robson, J., Riekehr, S., Kashaev, N., Wang, L., Lowe, T., & Karanika, A. (2016). *Process Optimization of Dual-Laser Beam Welding of Advanced Al-Li Alloys Through Hot Cracking Susceptibility Modeling* (Vol. 47A).

Tsivoulas, D., & Prangnell, P. B. (2014). The effect of Mn and Zr dispersoid-forming additions on recrystallization resistance in Al–Cu–Li AA2198 sheet. *Acta Materialia, 77*, 1-16. doi:10.1016/j.actamat.2014.05.028

Tsivoulas, D., Robson, J. D., Sigli, C., & Prangnell, P. B. (2012). Interactions between zirconium and manganese dispersoid-forming elements on their combined addition in Al–Cu–Li alloys. *Acta Materialia, 60*(13), 5245-5259. doi:10.1016/j.actamat.2012.06.012

Uféras, G. (2017a). Airware® 2195-T84 PLATE. In Constellium (Ed.), *www.constellium.com/sites/default/files/markets/airware_2195_t84_plate.pdf*.

Uféras, G. (2017b). Airware® 2196-T8511 Extrusions. In Constellium (Ed.), *www.constellium.com/sites/default/files/markets/airware_2196_t8511_extrusions.pdf*.

van Mourik, P., van Dam, J., & Picken, S. (2012). *Material Science in Design and Engineering* (First Edition ed.). Delft, The Netherlands: VSDD.

Wang, W. Z., & Shenoy, R. (1998). *Microstructural Characterization of Aluminum-Lithium Alloys 1460 and 2195*. Retrieved from Analytical Services & Materials, Inc., Hampton, Virginia:

Wanhill, R. J. H., & Bray, G. H. (2014). Chapter 2 - Aerostructural Design and Its Application to Aluminum–Lithium Alloys. In N. Eswara Prasad, A. A. Gokhale, & R. J. H. Wanhill (Eds.), *Aluminum-lithium Alloys* (pp. 27-58). Boston: Butterworth-Heinemann.

Warner, T. (2006). Recently-Developed Aluminium Solutions for Aerospace Applications. *Materials Science Forum, 519-521*, 1271-1278. doi:10.4028/www.scientific.net/MSF.519-521.1271

Wietelmann, U., & Steinbild, M. (2014). Lithium and Lithium Compounds. *Ullmann's Encyclopedia of Industrial Chemistry*. doi:10.1002/14356007.a15_393.pub2

Witkin, D., Lee, Z., Rodriguez, R., Nutt, S., & Lavernia, E. (2003). Al–Mg alloy engineered with bimodal grain size for high strength and increased ductility. *Scripta Materialia, 49*(4), 297-302. doi:10.1016/S1359-6462(03)00283-5

8. Table of Figures

Appendix A. Material Characteristics of AA2196

Cast	Si	Fe	Cu	Mn	Mg	Cr	Ni	Zn	Ti	Zr	Li	Silve
2196	0,024	0,039	3,07	0,32	0,33	0,001	0,0033	0,07	0,03	0,11	1,7	0,27

Longitudinal direction		
UTS	YS	E
654	648	9
655	646	8
653	649	9
650	644	8

Transverse direction		
UTS	YS	E
531	505	6
530	507	6

Figure 74- Material characteristics of the delivered alloy.

Appendix B. Hardness Values for Aging Curves

Sample number	***Solutionising temperature [°C] and time [hrs]***	***Age hardening time [hrs]***	***Age hardening temperature [°C]***	***Hardness values [HV5]***	***Average hardness value [HV5]***
1	530 – 1 hr	8	180	148, 146, 151, 148, 151	148.8
2	530 – 1 hr	12	180	158, 162, 167, 165, 165	163.4
3	530 – 1 hr	16	180	164, 167, 171, 174, 172	169.6
4	530 – 1 hr	20	180	165, 176, 180, 165, 173	171.8
5	530 – 1 hr	8	150	112, 111, 117, 115, 116	114.2
6	530 – 1 hr	12	150	131, 133, 132, 132, 136	132.8
7	530 – 1 hr	16	150	132, 134, 137, 136, 139	135.6
8	530 – 1 hr	20	150	141, 139, 139, 141, 139	139.8

Table 18 - Table showing the hardness values obtained for AA2196 after age hardening at 150°C, 160°C and 180°C for 8-20 hours.

Sample number	***Pre heating parameters***	***Solutionising temperature [°C] and time [min]***	***Age hardening time [hrs]***	***Age hardening temperature [°C]***	***Hardness values [HV5]***	***Average hardness value [HV5]***
1	200°C – 20 min	480 – 20 min	8	120	214, 213, 214, 207, 216	212.8
2	200°C – 20 min	480 – 20 min	12	120	231, 222, 226, 225, 229	226.6
3	200°C – 20 min	480 – 20 min	16	120	230, 230, 245, 238, 234	235.4
4	200°C – 20 min	480 – 20 min	20	120	234, 230, 237, 227, 216	228.8
5	200°C – 20 min	480 – 20 min	24	120	230, 226, 227, 226, 224	226.6

Table 19 - Table reporting the hardness values measured for AA7090 after age hardening at 120°C for 8-24 hours.

Age hardening at T = 160°C	
Time [hrs]	***Hardness [HV5]***
8	117, 128, 123, 119, 113
12	151, 159, 152, 158, 168
16	168, 167, 165, 166, 161
20	142, 144, 144, 142, 143

Table 20 - Table showing the hardness values measured when precipitation hardening at T=160°C for 8-20 hours.

Appendix C. Cold Working Data

Rod number	***Alloy***	***Initial height [cm]***	***Resulting height at each end [cm]***	***Average height used for calculation [cm]***	***Percent cold worked [%CW]***
1	2196	15.12	12.21, 12.29	12.25	19.0
2	2196	15.18	12.27, 12.30	12.285	19.0
3	2196	14.99	13.68, 13.55	13.625	9.1
4	2196	15.08	13.68, 13.38	13.53	10.3
5	2196	15.21	12.20, 12.22	12.21	19.7
7	2196	14.44	12.75, 12.64	12.70	12.05
10	2196	12.52	10.13, 10.11	10.12	19.2

Table 21 - Table showing the height measurements as well as percent cold worked for several rods.

Appendix D. Tensile Testing Data

Alloy	***% Cold Worked***	***Engineering Yield Strength [MPa], $R_{p0.2}$***	***Engineering Tensile Strength [MPa], R_m***	***%Elongation***
2196	12.0, 9.1, 10.3	445, 428, 432	536, 523, 517	8.59, 7.27, 7.67
2196	19.2	424, 421, 421, 427	512, 506, 515, 507	8.44, 6.45, 7.04, 7.77
2196	39.0	348, 337, 350, 351	460, 450, 462, 457	11.85, 15.92, 11.59, 11.37
2196	56.3	330, 335, 337, 282	445, 452, 461, 401	12.94, 16.14, 16.85, 16.02
7090	0	304, 307, 287, 284	421, 422, 402, 401	10.17, 10.44, 11.45, 11.17
7090	9.2	683, 678, 661, 743	701, 699, 679, 748	4.45, 4.75, 2.92, 1.36
7090	18.6	646, 657, 691, 658	679, 675, 711, 689	4.23, 1.86, 5.86, 6.72
7090	39.1	623, 595, 605, 613	662, 640, 651, 658	7.44, 8.27, 9.65, 10.77

Table 22 - The yield strength, tensile strength and %elongation of AA2196 and AA7090 at various degrees of cold work.

Alloy	***% Cold Worked***	***Specific Yield Strength [kPa m^3/kg]***
2196	12.0, 9.1, 10.3	203.8, 198.9, 196.6
2196	19.2	194.7, 192.4, 195.8, 192.8
2196	39.0	174.9, 171.1, 175.7, 173.8
2196	56.3	169.2, 171.9, 175.3, 152.5
7090	0	148.8, 149.1, 142.0, 141.7
7090	9.2	247.7, 247.0, 239.9, 264.3
7090	18.6	239.9, 238.5, 251.2, 243.5
7090	39.1	233.9, 226.1, 230.0, 232.5

Table 23 - Table showing calculated specific strength for each tensile test rod of AA2196 and AA7090.

Alloy	***% Cold Worked***	***Strain Hardening [MPa]***	***Tensile Toughness [MJ/m^3]***	***% Reduction in Area (%RA)***
2196	12.0, 9.1, 10.3	91, 95, 85	39.02, 44.98, 36.96	10.33, 14.65, 8.12
2196	19.2	88, 85, 94, 80	42.25, 31.97, 35.15, 38.86	16.48, 8.75, 7.87, 13.51
2196	39.0	112, 113, 112, 106	51.79, 68.64, 50.81, 49.51	15.87, 26.20, 25.96, 27.58
2196	56.3	115, 117, 124, 119	54.42, 69.63, 74.25, 60.31	20.20, 33.85, 25.96, 32.66
7090	0	117, 115, 115, 117	40.95, 42.24, 44.01, 42.54	10.37, 19,27, 18,94, 11.60
7090	9.2	18, 21, 18, 5	34.16, 36.04, 22.59, 13.74	10,91, 20.01, 14.56, 13.51
7090	18.6	33, 18, 20, 31	31.24, 15.28, 44.46, 48.61	8.40, 12.11, 21.32, 11.53
7090	39.1	39, 45, 46, 45	51.18, 54.30, 64.15, 72.37	19.66, 27.75, 21.32, 30.10

Table 24 - The strain hardening, tensile toughness and % reduction in area for AA2196 and AA7090

Appendix E. OM Pictures of the Second Transverse Direction for Cold Pressed Samples

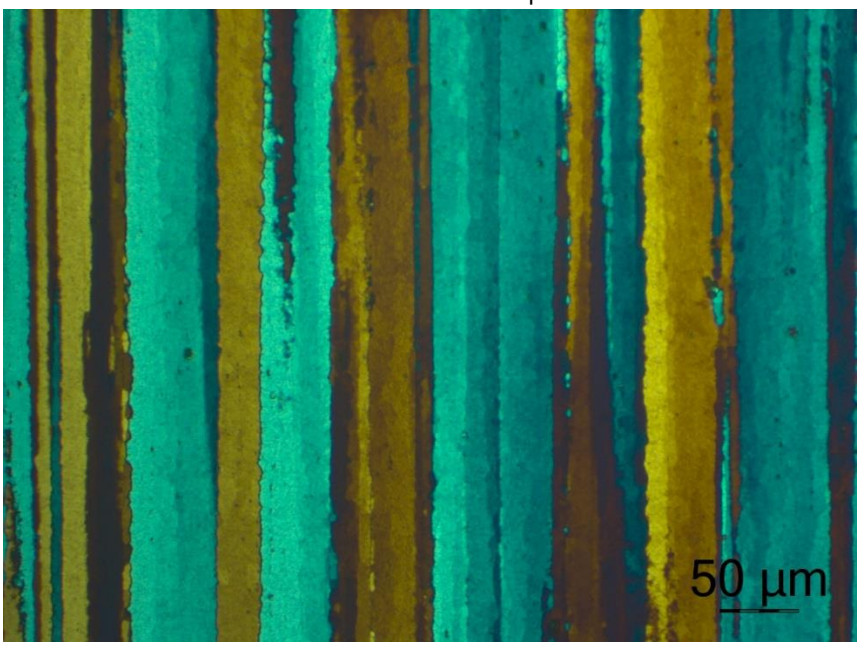

Figure 75 - Image of the microstructure in the second transverse direction for a 10.1%CW sample pressed in the extrusion.

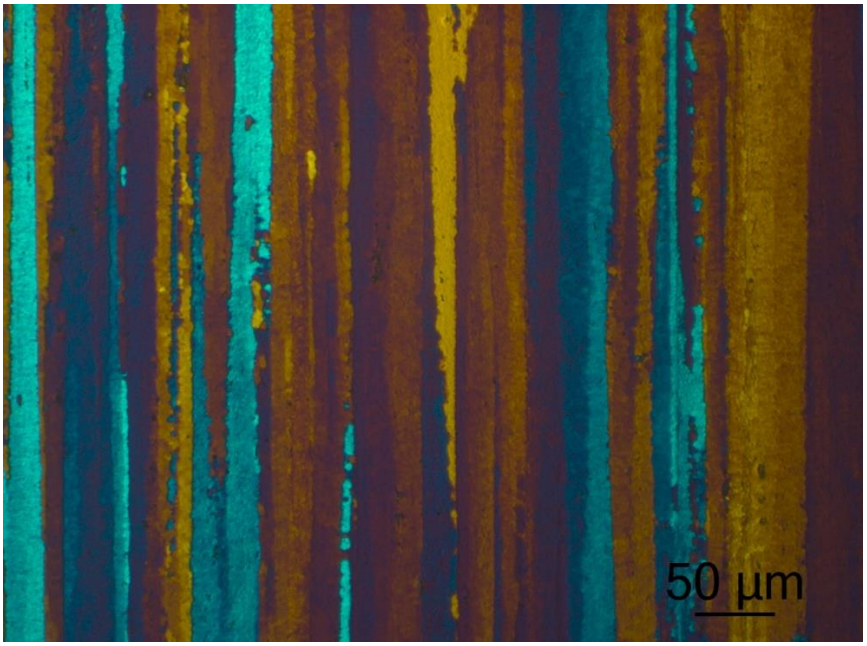

Figure 76 - Image of the microstructure in the second transverse direction for a 19.9%CW sample pressed in the extrusion direction.

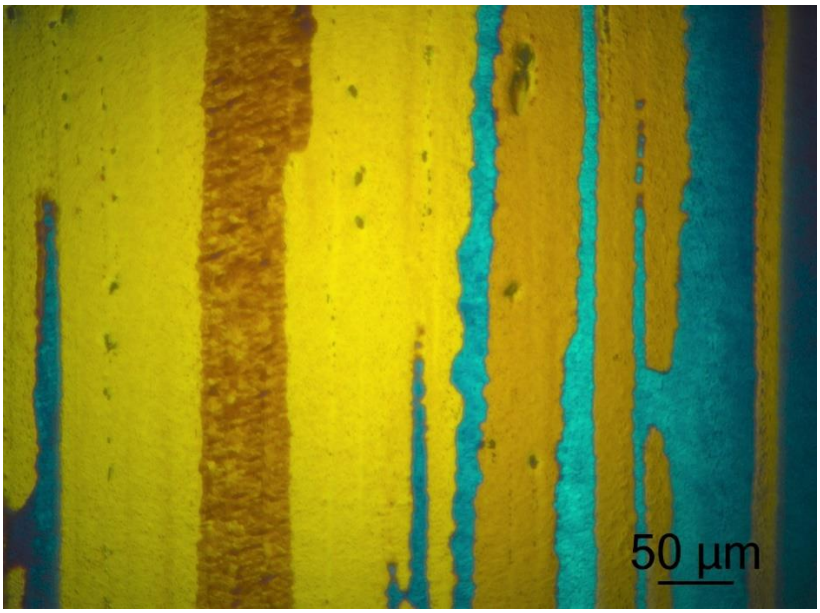

Figure 77 - Image of the microstructure in the second transverse direction for a 40.5%CW sample pressed in the extrusion direction.

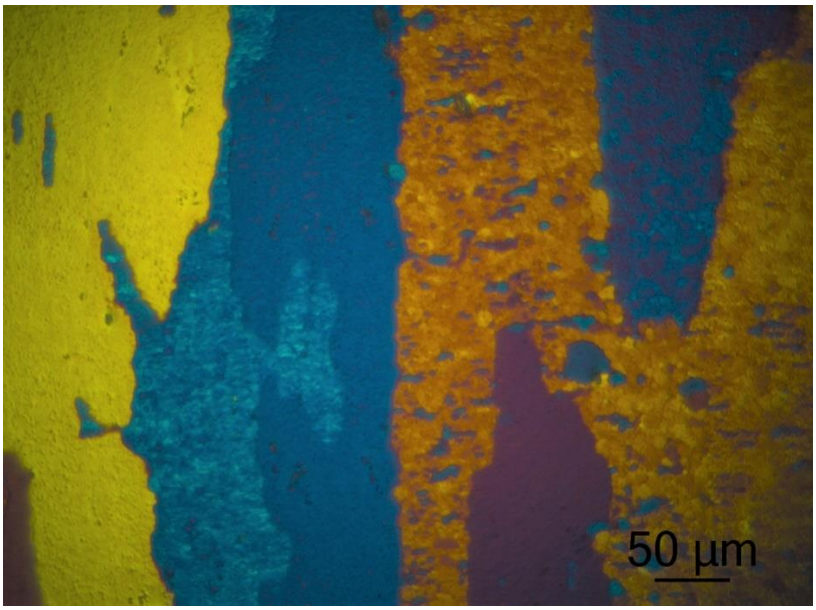

Figure 78 - Image of the microstructure in the second transverse direction for a 55.5%CW sample pressed in the extrusion direction.

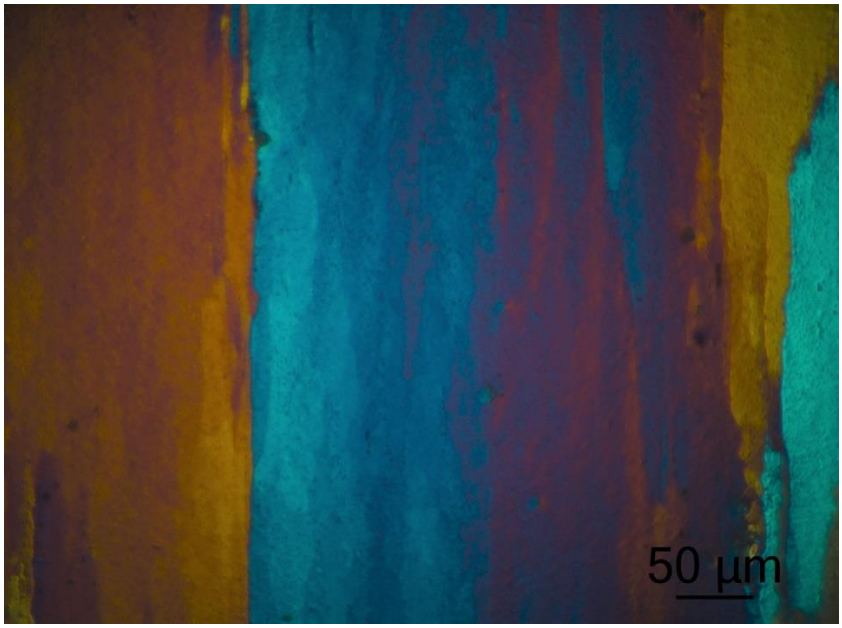

Figure 79 - Image of the microstructure in the non-pressed transverse direction for a 7.4%CW sample pressed in the transverse direction.

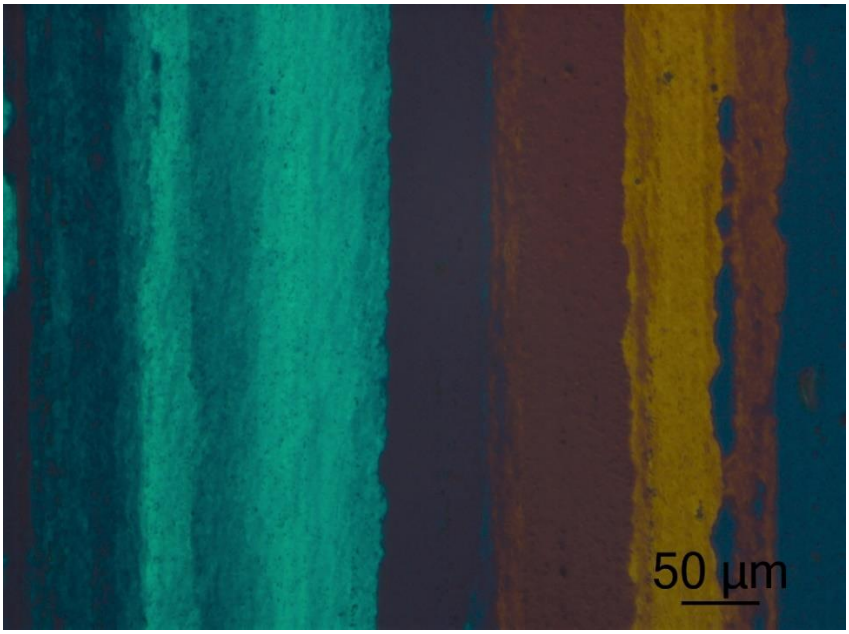

Figure 80 - Image of the microstructure in the non-pressed transverse direction for a 18.7%CW sample pressed in the transverse direction.

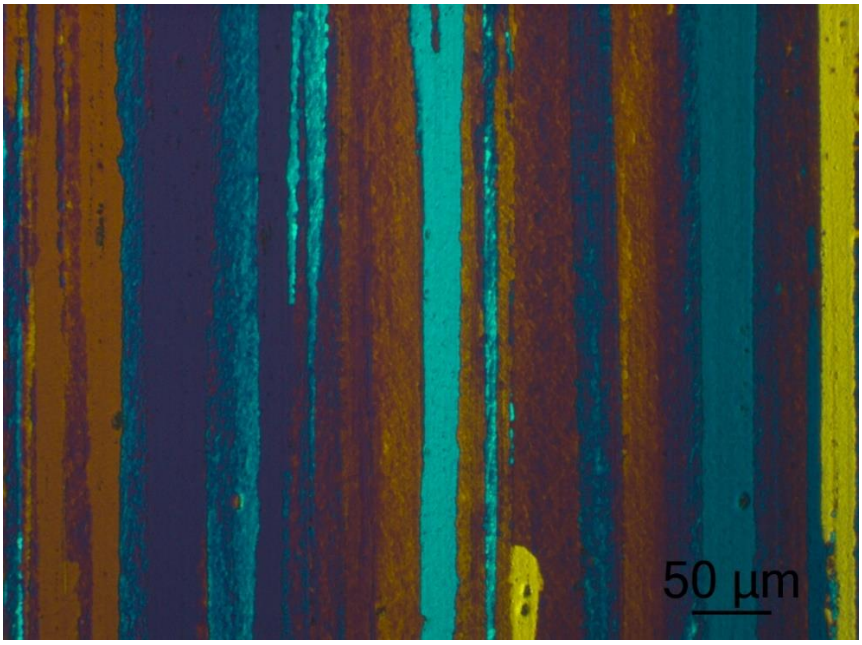

Figure 81 - Image of the microstructure in the non-pressed transverse direction for a 40.1%CW sample pressed in the transverse direction.

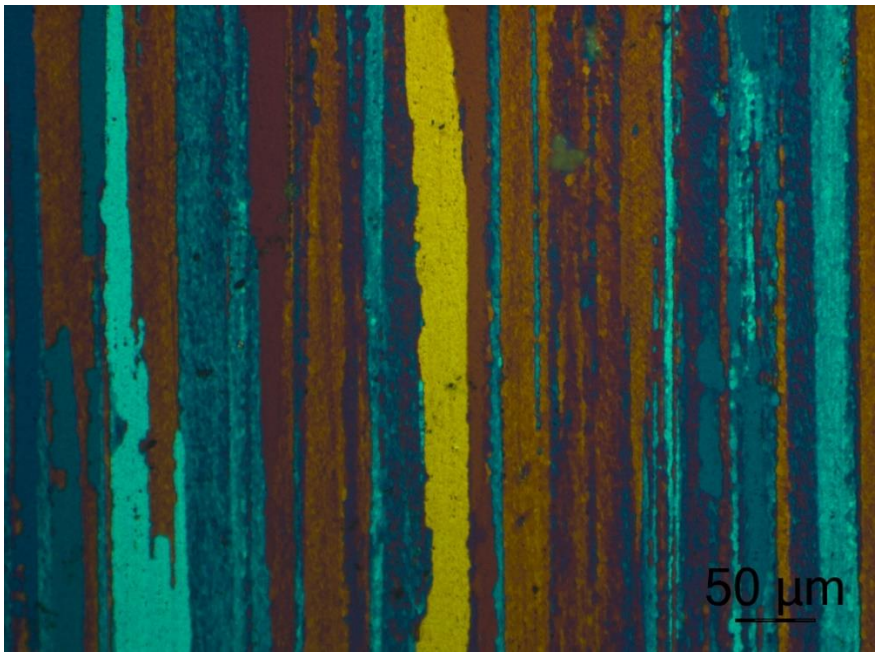

Figure 82 - Image of the microstructure in the non-pressed transverse direction for a 58.7%CW sample pressed in the transverse direction.

Appendix F. Grain Size Distribution using EBSD

Chart: Grain Size (diameter)

Edge grains included in analysis

Diameter [microns]	Area Fraction
1.0817	0.0083097
1.38064	0.00275319
1.7622	0.00257418
2.24921	0.00448244
2.8708	0.00512688
3.66418	0.00826316
4.67682	0.00913316
5.96931	0.0186029
7.619	0.0195695
9.7246	0.0312446
12.4121	0.0328486
15.8423	0.0273637
20.2205	0.0335324
25.8087	0.0474058
32.9413	0.0355194
42.045	0.0391605
53.6646	0.0384122
68.4954	0.112988
87.4249	0.117224
111.586	0.405486
Average	
Number	3.09276
Area	72.8643
Standard Deviation	
Number	7.63626
Area	43.3349

Figure 83 - Grain size distribution in the transverse direction for AA2196-T8511 as delivered from Constellium.

Chart: Grain Size (diameter)

Edge grains included in analysis

Diameter [microns]	Area Fraction
5.17864	0.0261495
6.0599	0.0224205
7.09112	0.0349492
8.29782	0.022951
9.70987	0.0160392
11.3622	0.0329833
13.2957	0.0286927
15.5583	0.0250573
18.2058	0.0259311
21.304	0.0346372
24.9293	0.0300345
29.1715	0.0473375
34.1357	0.0741579
39.9446	0.0716927
46.742	0.109825
54.6961	0.113179
64.0038	0.0608647
74.8954	0.115301
87.6404	0.0624873
102.554	0.0453092
Average	
Number	10.7946
Area	44.9301
Standard Deviation	
Number	11.584
Area	27.6592

Figure 84 - Grain distribution in the extrusion direction for AA2196-T8511 as delivered from Constellium.

Chart: Grain Size (diameter)

Edge grains included in analysis

Diameter [microns]	Area Fraction
5.21293	0.0159915
6.18108	0.0104038
7.32903	0.0188826
8.69017	0.0155012
10.3041	0.0189042
12.2178	0.0234176
14.4869	0.0212042
17.1774	0.0266981
20.3675	0.0218747
24.1502	0.0309735
28.6353	0.0353283
33.9535	0.0435187
40.2593	0.0521345
47.7362	0.0838074
56.6018	0.111039
67.1139	0.124687
79.5782	0.102647
94.3575	0.0961939
111.882	0.111234
132.66	0.035559
Average	
Number	12.7847
Area	60.7266
Standard Deviation	
Number	15.4854
Area	35.0968

Figure 85 - Grain size distribution in the extrusion direction for 0%CW AA2196.

Chart: Grain Size (diameter)

Edge grains included in analysis

Diameter [microns]	Area Fraction
5.32948	0.00905889
6.60497	0.00335667
8.18573	0.00773823
10.1448	0.00800649
12.5728	0.00894196
15.5818	0.0108748
19.3109	0.0100975
23.9326	0.0126701
29.6604	0.0103383
36.7589	0.0127113
45.5564	0.022802
56.4594	0.041924
69.9717	0.0273418
86.718	0.0281809
107.472	0.0484448
133.193	0.10103
165.07	0.145761
204.576	0.13739
253.537	0.218555
314.216	0.134776
Average	
Number	15.7283
Area	180.995
Standard Deviation	
Number	30.8937
Area	96.825

Figure 86 - Grain size distribution in the pressed transverse direction for 0%CW AA2196.

Chart: Grain Size (diameter)

Edge grains included in analysis

Diameter [microns]	Area Fraction
5.20612	0.0228993
6.15686	0.0174499
7.28123	0.0293126
8.61093	0.0243223
10.1835	0.025201
12.0432	0.0223878
14.2425	0.0279027
16.8435	0.0322177
19.9194	0.0301061
23.5571	0.0447952
27.8591	0.0412016
32.9468	0.0585597
38.9635	0.0859116
46.079	0.114024
54.494	0.131946
64.4457	0.125415
76.2148	0.0837607
90.1332	0.0431099
106.593	0.0116267
126.059	0.0278503
Average	
Number	11.4279
Area	45.856
Standard Deviation	
Number	12.2844
Area	27.8988

Figure 87 - Grain size distribution in the extrusion direction for 10.1%CW AA2196.

Chart: Grain Size (diameter)

Edge grains included in analysis

Diameter [microns]	Area Fraction
5.3677	0.00537329
6.74811	0.00284961
8.48352	0.00633713
10.6652	0.0078504
13.408	0.00725906
16.8561	0.00968496
21.191	0.00927521
26.6407	0.00441876
33.4918	0.0121248
42.1049	0.00769209
52.933	0.0096384
66.5458	0.0122133
83.6593	0.0051591
105.174	0.0218331
132.221	0.0402438
166.225	0.0208599
208.973	0.0155611
262.714	0.114851
330.276	0.332832
415.213	0.353943
Average	
Number	15.4103
Area	311.925
Standard Deviation	
Number	39.4145
Area	130.763

Figure 88 - Grain size distribution in the pressed transverse direction for 7.4%CW AA2196.

Chart: Grain Size (diameter)

Edge grains included in analysis

Diameter [microns]	Area Fraction
5.27023	0.0354043
6.38713	0.0311852
7.74074	0.018543
9.3812	0.0149095
11.3693	0.0127023
13.7788	0.0141737
16.6989	0.00710189
20.2378	0.0101048
24.5268	0.0142939
29.7246	0.0105853
36.0241	0.0226269
43.6585	0.0285727
52.9109	0.0701931
64.1242	0.0665596
77.7138	0.107835
94.1834	0.092775
114.143	0.120987
138.333	0.0677908
167.65	0.0795622
203.18	0.174094
Average	
Number	9.10127
Area	102.979
Standard Deviation	
Number	15.1421
Area	67.9774

Figure 89 - Grain size distribution in the extrusion direction for 19.9%CW AA2196.

Chart: Grain Size (diameter)

Edge grains included in analysis

Diameter [microns]	Area Fraction
5.38023	0.00667979
6.79546	0.00343073
8.58296	0.00434334
10.8407	0.00350256
13.6922	0.00626996
17.2939	0.0073727
21.8429	0.00911342
27.5885	0.00845854
34.8455	0.00848811
44.0114	0.00843319
55.5884	0.0178297
70.2105	0.00757973
88.6789	0.0177748
112.005	0.0184761
141.468	0.0215266
178.68	0.0477726
225.68	0.0925665
285.044	0.0923721
360.023	0.312129
454.725	0.30588
Average	
Number	15.2703
Area	315.719
Standard Deviation	
Number	40.494
Area	139.605

Figure 90 - Grain size distribution in the pressed transverse direction for 18.7%CW AA2196.

Chart: Grain Size (diameter)

Edge grains included in analysis

Diameter [microns]	Area Fraction
5.29554	0.0332167
6.47958	0.0314905
7.92838	0.0152238
9.70111	0.0133778
11.8702	0.00802546
14.5243	0.00462708
17.7719	0.00559205
21.7456	0.00332047
26.6077	0.00584978
32.557	0.0114358
39.8366	0.012221
48.7438	0.0263719
59.6426	0.0306214
72.9783	0.0670686
89.2958	0.0690885
109.262	0.152831
133.692	0.124086
163.585	0.166047
200.161	0.0984692
244.916	0.121035
Average	
Number	8.62302
Area	125.618
Standard Deviation	
Number	16.5394
Area	70.3474

Figure 91 - Grain size distribution in the extrusion direction for 40.5%CW AA2196.

Chart: Grain Size (diameter)

Edge grains included in analysis

Diameter [microns]	Area Fraction
7.13626	0.0210692
8.91974	0.00481357
11.149	0.0109193
13.9353	0.00864076
17.418	0.0130992
21.771	0.0107812
27.212	0.0074275
34.0128	0.0155257
42.5132	0.0202012
53.138	0.0210692
66.4181	0.0156342
83.0173	0.0253798
103.765	0.0359341
129.697	0.0305583
162.111	0.0322549
202.626	0.0785954
253.266	0.100217
316.561	0.173298
395.676	0.123979
494.562	0.250602
Average	
Number	14.5955
Area	287.014
Standard Deviation	
Number	32.1912
Area	173.068

Figure 92 - Grain size distribution in the pressed transverse direction for 40.1%CW AA2196.

Chart: Grain Size (diameter)

Edge grains included in analysis

Diameter [microns]	Area Fraction
5.22359	0.0738409
6.21904	0.101551
7.40421	0.0396716
8.81522	0.085753
10.4951	0.0594045
12.4952	0.0602199
14.8764	0.0419618
17.7114	0.0394234
21.0867	0.0246822
25.1051	0.0181234
29.8894	0.0115434
35.5854	0.0195273
42.3669	0.0238171
50.4408	0.0342615
60.0533	0.0465919
71.4977	0.0738551
85.1229	0.081371
101.345	0.0722668
120.658	0.0655804
143.652	0.0265541
Average	
Number	7.77841
Area	44.0398
Standard Deviation	
Number	7.07743
Area	42.5346

Figure 93 - Grain size distribution in the extrusion direction for 55.5%CW AA2196.

Chart: Grain Size (diameter)

Edge grains included in analysis

Diameter [microns]	Area Fraction
5.31367	0.0876298
6.54636	0.0155206
8.06503	0.0180445
9.936	0.0214439
12.241	0.0180445
15.0808	0.0134947
18.5793	0.0140441
22.8894	0.0116061
28.1994	0.0154691
34.7413	0.0203451
42.8008	0.0244828
52.73	0.0401064
64.9626	0.059988
80.033	0.0471972
98.5995	0.0434715
121.473	0.0861877
149.653	0.261035
184.371	0.057344
227.142	0
279.836	0.144545
Average	
Number	7.56196
Area	123.25
Standard Deviation	
Number	12.4643
Area	97.5441

Figure 94 - Grain size distribution in the pressed transverse direction for 58.7%CW AA2196.

Appendix G. Additional Data Logging Measurements of N11/R

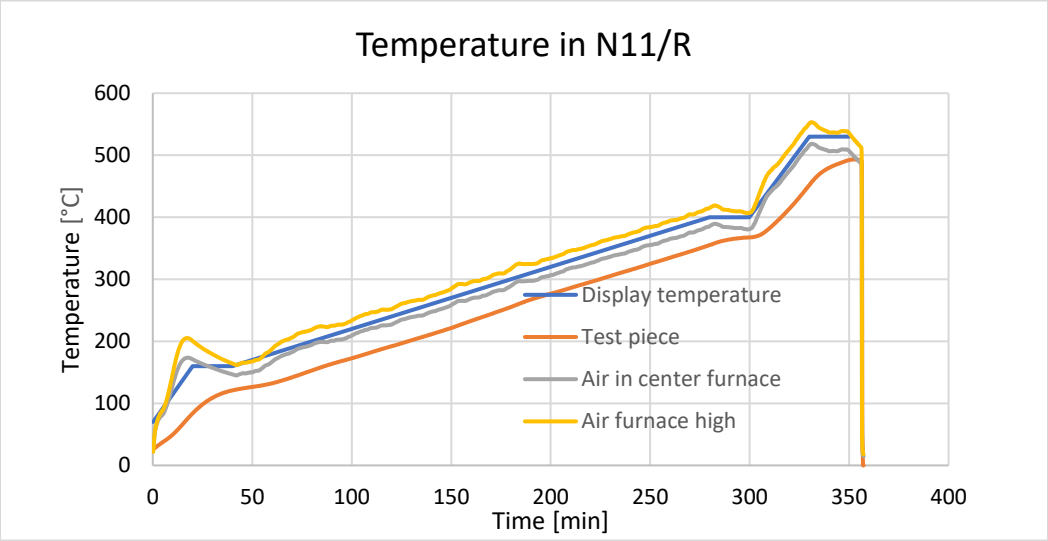

Figure 95 - The temperature measured in N11/R for three thermocouples either inside a metal test piece, in the air circa 3 cm above the sample or in the top of the furnace.

A thermocouple was placed so that it measured the temperature in the top of the furnace, while another was placed such that it measured the air 3 cm above the sample. Additionally, one was placed within a sample piece. The time-temperature measurements can be seen in Figure 95.

Appendix H. Images of the Fracture Surface of Charpy Samples

Figure 96 - Pictures showing the Charpy samples for 0-39.1%CW of AA7090. Cold work increases from left to right and from top to bottom.

Appendix I. Geometry and Dimensions of Tensile Testing Rods

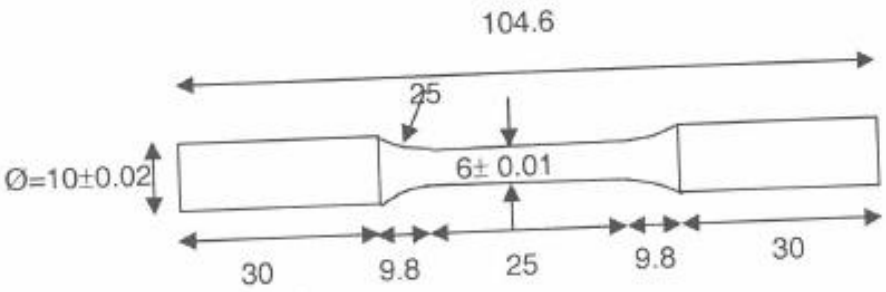

Figur 1. Geometri og dimensjon på strekkstavene. Alle mål er i mm.

Figure 97 - Dimensions of the largest tensile testing samples used. All values in mm.

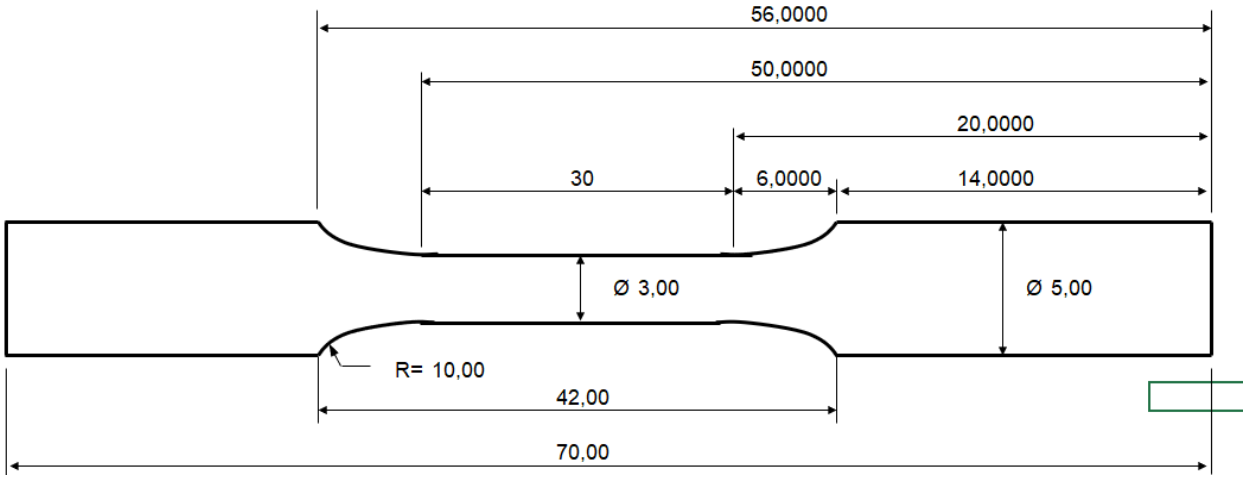

Figure 98 - Dimensions of the smallest tensile testing samples used. All values in mm.

Appendix J. NS-EN ISO 148-1:2016 Charpy Standard

Table 2 — Tolerances on specified test piece dimensions

Designation	Symbol and no.	V-notch test piece			U-notch test piece		
		Nominal dimension	Machining tolerance		Nominal dimension	Machining tolerance	
				Tolerance class[a]			Tolerance class[a]
Length	*L*	55 mm	±0,60 mm	js15	55 mm	±0,60 mm	js15
Width	*W*	10 mm	±0,075 mm	js12	10 mm	±0,11 mm	js13
Thickness[c]	*B*	10 mm	±0,11 mm	js13	10 mm	±0,11 mm	js13
— standard test piece — subsize test piece — subsize test piece — subsize test piece		10 mm 7,5 mm 5 mm 2,5 mm	±0,11 mm ±0,11 mm ±0,06 mm ±0,05 mm	js13 js13 js12 js12	10 mm 7,5 mm 5 mm —	±0,11 mm ±0,11 mm ±0,06 mm —	js13 — — —
Angle of notch	1	45°	±2°	—	—	—	—
Ligament	2	8 mm	±0,075 mm	js12	5 mm	±0,09 mm	js13
Notch radius	3	0,25 mm	±0,025 mm	—	1 mm	±0,07 mm	js12
Notch position (centering)	4	27,5 mm	±0,42 mm[d]	js15	27,5 mm	±0,42 mm[d]	js15
Angle between plane of symmetry of notch and longitudinal axis of test piece		90°	±2°	—	90°	±2°	—
Angle between adjacent longitudinal faces of test piece	5	90°	±2°	—	90°	±2°	—
Surface roughness[b]	NA	<5 µm			<5 µm		

[a] In accordance with ISO 286-1.

[b] The test pieces shall have a surface roughness better than *Ra* 5 µm except for the ends.

[c] If another thickness (2 mm or 3 mm) is specified, the corresponding tolerances shall also be specified.

[d] For machines with automatic positioning of the test piece, it is recommended that the tolerance be taken as ±0,165 mm instead of ±0,42 mm.

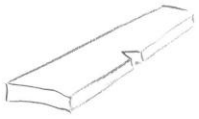

Nedskalert 5x10 x 55 mm

Figure 99 - Standard for the construction of Charpy samples.